UNIVERSITY OF CALIFORNIA,
IRVINE

Experimental Investigation of Multi-Component Suspensions Flowing and Settling in Analog Fractures

DISSERTATION

submitted in partial satisfaction of the requirements
for the degree of

DOCTOR OF PHILOSOPHY

in Civil Engineering

by

Ricardo Medina

Dissertation Committee:
Associate Professor Russell L. Detwiler, Chair
Professor Brett F. Sanders
Associate Professor Amir AghaKouchak

2018

DEDICATION

To my parents, my wife, and all my family.

TABLE OF CONTENTS

LIST OF FIGURES

LIST OF TABLES

LIST OF SYMBOLS

Symbol	
a	particle radius (L)
A_{ab}	light absorbance (-)
A_d	area occupied by dyed water, used to measure the mean fracture aperture (L^2)
b	fracture aperture (L)
C	dye concentration (M L^{-3})
d	sand particle diameter (L)
d_f	fiber particle diameter (L)
D	self-induced shear-diffusion (M L^{-2})
$d(\phi)$	particle self diffusion coefficient (-)
h	fracture height or aperture (L)
I	measured intensity (cd)
I_i	measured intensity of image (cd)
I_0	incident light intensity (cd)
I_r	measured intensity at a pixel in a reference image (cd)
I_η	viscous number (-)
i, j	coordinate positions in the x- and y-direction, respectively
L	fracture length (L)
L_{dev}	development length (L)
$\dot{m}_{in}$	mass-flow-rate in (M T^{-1})
$\dot{m}_{out}$	mass-flow-rate out (M T^{-1})
P	total pressure (M L^{-1} T^{-2})
P_s	pressure acting on a solid particle (M L^{-1} T^{-2})
P_f	pressure acting on the fluid (M L^{-1} T^{-2})
Q	volumetric flow rate (L^3 T^{-1})
Q_{in}	volumetric influent flow rate (L^3 T^{-1})
Q_{out}	volumetric effluent flow rate (L^3 T^{-1})
Re_p	particle Reynolds number (-)
t_{dev}	development time (T)
t_{flow}	time for Q_{out} to reach Q_{in} (T)
U_α	volume of parcel of fluid occupied by tracked particle α (L^3)
V_d	volume occupied by dyed water (L^3)
V_x	velocity component in flow-direction (L T^{-1})
v_{ij}^x	x-velocity component in cell i, j (L T^{-1})
v_{ij}^y	y-velocity component in cell i, j (L T^{-1})
V_s	settling velocity in Stokes regime (L T^{-1})
W	fracture width (L)

Greek Symbols

α	absorbance coefficient (L^{-1})
α	tracked particle in PIC model (-)
β	shear-thinning coefficient in Ellis fluid (-)
γ_f	specific weight of fluid (M L^{-2} T^{-2})
$\dot{\gamma}$	shear rate (T^{-1})
ΔP_f	pressure difference of fluid across fracture (M L^{-1} T^{-2})
Δt	timestep used in simulation (T)
Δx	size of cell in the x-direction (L)
Δx_α	x-displacement of tracked particle (L)
Δy	Size of cell in the y-direction (L)
Δy_α	Y-displacement of tracked particle (L)
ϵ	absorption coefficient of solute (M mol^{-1} L^{-1})
η	apparent viscosity (M L^{-1} T^{-1})
η_f	apparent fluid viscosity (M L^{-1} T^{-1})
η_r	relative viscosity (M L^{-1} T^{-1})
η_s	apparent suspension viscosity (M L^{-1} T^{-1})
ϕ	solid volume fraction or volume of solid/total volume (-)
ϕ_0	average solid volume fraction (-)
ϕ_{cr}	critical solid volume fraction (-)
ϕ_{mob}	solid volume fraction for solid mobilization (-)
ϕ_f	solid volume fraction of fibers (-)
ϕ_s	solid volume fraction of sand (-)
ρ_w	density of water (M L^{-3})
ρ_s	density of suspension (M L^{-3})
ρ_p	density of solid particles (M L^{-3})
σ_n	normal stress, applied to fracture surfaces (M L^{-1} T^{-2})
σ_{ap}	standard deviation from mean aperture (-)
τ	shear stress (M L^{-1} T^{-2})
$\tau_{1/2}$	shear stress at which $\eta = \eta_0/2$ in Ellis fluid (M L^{-1} T^{-2})
Ω_{ij}	region occupied by cell i, j in PIC model (L^2)
ξ	absorbance of solvent and glass plates (-)
$\langle \cdot \rangle$	spatially averaged quantity (-)

ACKNOWLEDGMENTS

I would like to thank my advisor, Dr. Russell L. Detwiler for his guidance, support, pep-talks, and for always motivating me to do my best.

Special thanks to the members of my committee, Dr. Brett Sanders and Dr. Amir AghaKouchak.

I would also like to thank Dr. Romain Prioul, Dr. Joseph (Joe) Morris, Dr. Wenyue Xu, and Dr. Jean E. Elkhoury for their substantive discussions and advice regarding my research.

I would also like to thank Trevor Jones for all the thoughtful discussions about our research, for showing me around the lab when I arrived at UCI, for helping me with my experiments, but most importantly for being a good friend. I also thank Pablo Torres for his unconditional friendship.

I would like to thank Schlumberger-Doll Research, the Henry Samueli School of Engineering, and the Department of Civil & Environmental Engineering for providing financial support for my Ph.D. degree.

CURRICULUM VITAE

Ricardo Medina

EDUCATION

Doctor of Philosophy in Civil Engineering **2018**
University of California-Irvine *Irvine, CA*

Masters of Science in Civil Engineering **2013**
California State University, Los Angeles *Los Angeles, CA*

Bachelor of Science in Civil Engineering **2009**
University of California Davis *Davis, CA*

RESEARCH EXPERIENCE

Graduate Research Assistant **2013–2018**
University of California, Irvine *Irvine, CA*

Graduate Research Assistant **2010–2013**
California State University Los Angeles *Los Angeles, CA*

TEACHING EXPERIENCE

Teaching Assistant **2013–2018**
University of California Irvine *Irvine, CA*

Part Time Lecturer **2015–2017**
California State University Los Angeles *Los Angeles, CA*

Teaching Assistant **2011–2013**
California State University Los Angeles *Los Angeles, CA*

Laboratory Assistant **2011**
California State University Los Angeles *Los Angeles, CA*

REFEREED JOURNAL PUBLICATIONS

Flow of dense suspensions through fractures: significant in-plane velocity variations caused by small variations in solid concentration **2015**
Geofluids

Use of Fly Ash as Soil Amendment to Offset Anion Exclusion Effect on Nitrate Transport **2015**
Vadose Zone Journal

BOOK CHAPTERS

Flow of dense suspensions through fractures: significant in-plane velocity variations caused by small variations in solid concentration **2016**
Crustal Permeability. Tom Gleeson & Steve Ingebritsen (Eds.). Wiley.

REFEREED CONFERENCE PUBLICATIONS

Fiber-Laden Proppant Placement in a Deformable Fracture: Influence of Fracture-Surface Roughness **Dec 2016**
American Geophysical Union Fall Meeting

Effect of Confining Stress on Sand-Fiber Proppant Placement in a Deformable Fracture **Jun 2016**
US Rock Mechanics/Geomechanics Symposium

Proppant distribution in a fracture subjected to normal stress **Dec 2015**
American Geophysical Union Fall Meeting

Flow of High Solid Volume Fraction Fluids through Fractures and around Obstructions **Jun 2015**
US Rock Mechanics/Geomechanics Symposium

Flow of concentrated suspensions through fractures: Significant in-plane velocity variations caused by small variations in solid concentration — **Dec 2014**
American Geophysical Union Fall Meeting

Flow of Dense Suspensions Through Fractures: Experimental And Computational Observation of Velocity-Field Heterogeneity — **Jun 2014**
US Rock Mechanics/Geomechanics Symposium

Flow and Geometry Control the Onset of Jamming in Fractures with High Solid-Fraction Fluids — **Dec 2013**
American Geophysical Union Fall Meeting

On the implementation of open source CFD system to flow visualization in fluid mechanics — **Jun 2012**
American Society for Engineering Education

Implementation of Particle Image Velocimetry in the Fluid Mechanics Laboratory — **Apr 2011**
American Society for Engineering Education

ABSTRACT OF THE DISSERTATION

Experimental Investigation of Multi-Component Suspensions Flowing and Settling in Analog Fractures

By

Ricardo Medina

Doctor of Philosophy in Civil Engineering

University of California, Irvine, 2018

Associate Professor Russell L. Detwiler, Chair

Suspensions of non-Brownian particles are ubiquitous in natural processes such as debris flows, magma flows, and sediment transport in river systems. Non-Brownian suspensions are used in engineering applications such as the injection of slurries for environmental remediation, mud injection during well drilling, cosmetics, and hydraulic fracturing. Suspensions are especially important in hydraulic fracturing, a technique developed in the 1940's by the oil industry to increase production rates from wells. The goal of hydraulic fracturing in oil and gas applications, is to enhance the permeability of subsurface rock formations by injecting a pressurized fluid to create a network of conductive pathways, i.e., fractures. The fluid used in hydraulic fracturing is composed of solids, chemical additives, and water. The solids (e.g., proppants) are used to *prop* open the fracture and allow hydrocarbons to flow through the fracture. The hydrocarbons flow through the pore spaces between proppant particles, which means the fracture conductivity is limited by the amount and distribution of proppants delivered to the fracture.

The work presented in this dissertation explores the behavior of two different proppant mixtures (suspensions). The first suspension is a conventional proppant mixture (sand only) with a high solid volume fraction, $\phi_s = 0.5$, which may increase fracture permeability by

increasing the amount of sand delivered to the fracture. The second suspension is made up of sand ($\phi_s = 0.177$) and polymeric fibers ($\phi_f = 0.0038$), which may create a proppant distribution that may enhance fracture permeability. I used transparent, laboratory-scale (15.2 cm $\times$ 15.2 cm), fractures to understand the behavior of these suspensions as they flow through and settle inside hydraulic fractures.

Concentrated suspensions flowing through idealized parallel-plate fractures exhibited complex flow behavior. Concentrated suspensions flowing through parallel fractures developed a non-uniform velocity distribution across the fracture width (in the plane of the fracture). As the concentrated suspension flowed through a confined rectangular channel (e.g., fracture) the suspension developed regions of high velocity near the no-flow boundaries where velocity was expected to be the lowest. These high-velocity regions were $\sim$2cm wide and were observed regardless of upstream boundary conditions. Furthermore, the observed non-uniform velocity distribution persisted irrespective of flow rate and fracture geometry. Through further experiments it was observed that these high-velocity regions were due to non-uniform ϕ distribution in the plane of the fracture. Additionally, the pressure gradient across the fracture, ∇P, exhibited behavior that defied simple relationships between applied pressure gradient and flow rate. It was observed that the timescale required for ∇P to reach a steady state was significantly longer than expected. The cause of the transient ∇P was explored using a two-dimensional numerical model of concentrated suspensions flowing through a fracture of the same dimension as our experiments.

I explored the flow and settling behavior of multi-component (sand-fiber) proppant mixtures inside a fracture subjected to an applied stress. The experiments presented here show that adding fibers to conventional proppants leads to heterogeneous proppant distribution inside the fracture. This heterogeneous proppant distribution led to the formation of sand-fiber *clusters* capable of supporting the applied stress and maintained the fracture open. Additionally, it was observed that injecting solids-free fluid (flowback) led to the mobilization of

some solids within the proppant pack. Solid mobilization and flowback was explored through the use of a non-Newtonian flow solver that simulates flow through a mixed fracture-porous matrix medium. The experimental and numerical results suggest that adding polymer fibers to conventional proppants leads to highly heterogeneous proppant distribution which may lead to higher fracture permeability.

Chapter 1

Introduction

1.1 Background

Suspensions of non-Brownian particles are ubiquitous in many natural processes and engineering applications. Natural suspensions are found in mud and debris flows characterized by high suspended solids concentration (Mueller et al., 2009), intrusion of magma composed of crystals suspended in silicate melts (Mader et al., 2013), mobilization of suspended sediments in the shallow crust such as sand intrusion in sedimentary basins (Huuse et al., 2010), and mud volcanoes leading to the migration of fluidized solids through preexisting or propagating fractures (Manga and Brodsky, 2006). Suspensions used in engineering applications include the injection of slurries for environmental remediation (Murdoch et al., 2006), mud injection during well drilling (Bittleston et al., 2002), injection of slurries containing high concentrations of sands in hydraulic fracturing for oil and gas production (Kern et al., 1959; Montgomery, 2013), and micro-particle suspensions in food, paint, and cosmetics industries.

Non-Brownian suspensions are especially important in hydraulic fracturing, a technique aimed at enhancing the permeability of subsurface rock formations by injecting pressur-

ized fluid to create a network of conductive pathways, i.e., fractures. Hydraulic fracturing was developed in the late 1940's by the oil and gas industry to increase production from oil wells (Kern et al., 1959). Hydraulic fracturing has been used for the disposal of radioactive waste materials (de Laguna, 1966), preconditioning rock mass to cave formation in mining operations (Katsaga et al., 2015), enhanced geothermal systems (Legarth et al., 2005), and carbon sequestration (Boschi et al., 2009). Over the last couple of decades, use of hydraulic fracturing in the oil industry proliferated in part due to the introduction of horizontal well drilling. Horizontal drilling allowed the use of multi-stage fracturing, reducing the cost and allowing the recovery of oil and gas from unconventional reservoirs, e.g., shale reservoirs (Kim and Moridis, 2015; Guo et al., 2014).

The goal of hydraulic fracturing is to enhance oil and gas production at the well by increasing the formation permeability through the creation of a network of fractures connecting the reservoir and the well. The hydraulic fracturing process starts with the installation of a well (see Figure 1.1 for a typical hydraulic fracturing process). The well is initially drilled vertically and transitions to horizontal in the targeted 'pay zone,' i.e., the hydrocarbon-rich formation (Kim and Moridis, 2015). The wellbore is protected by a steel casing typically extending to shallow depths. In addition to the steel casing some wells are protected by a concrete annulus which may may extend the entire length of the well (Economides and Nolte, 2000). Small perforations or weak points are created on the wellbore through the use of explosives or hydro-jets; the location of these perforations serves as the starting point for the fractures. Fracturing fluid is injected into a region of the wellbore that has been isolated using packers. The fluid pressure is increased until the formation rock near the well fails and the fractures are initiated (Economides and Martin, 2007). After fracture initiation, solids-free fluid is injected to propagate the fracture and increase fracture aperture, then a fluid mixed with solids (i.e., proppants) is injected to propagate the fracture further into the formation. The cycle of injecting proppant-free carrier fluid followed by proppant-laden carrier fluid is typically repeated several times until the desired fracture length is reached (Yew and

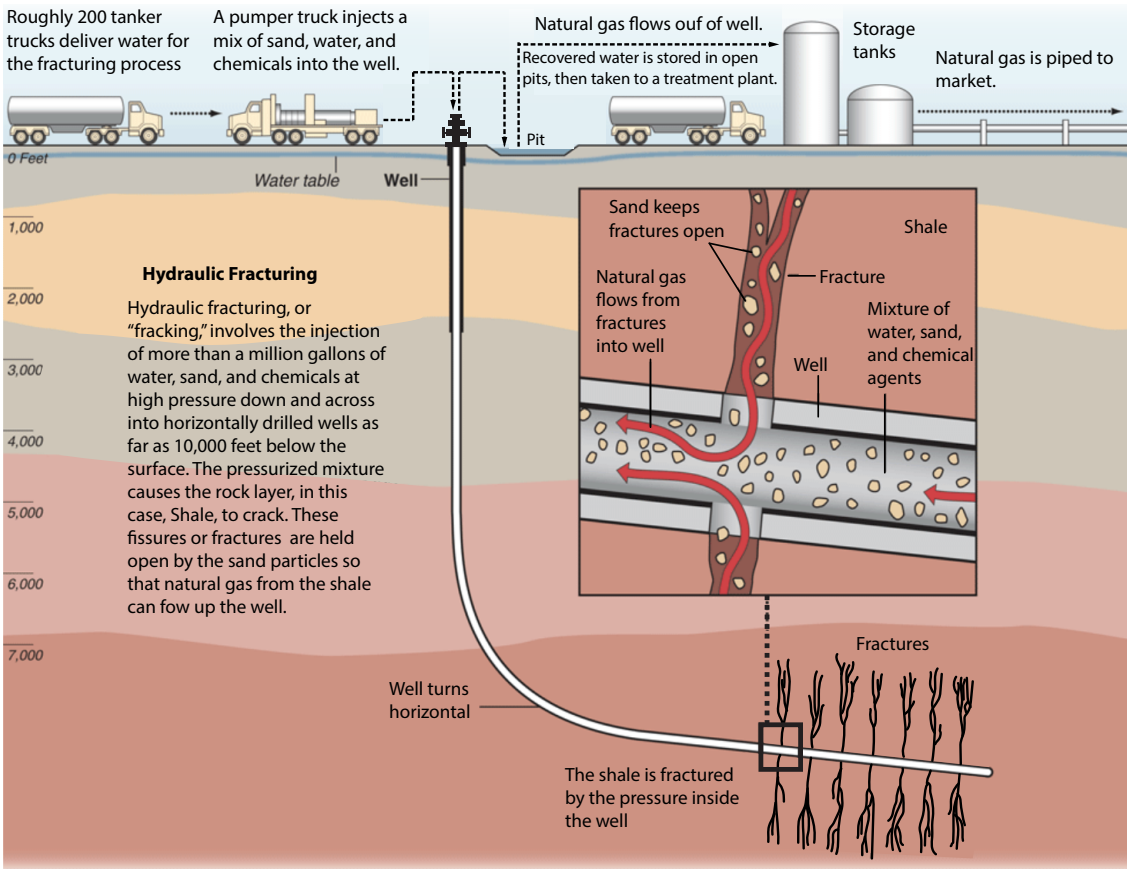

Figure 1.1: Schematic depicting the process of hydraulic fracturing. The well is initially drilled vertically and switches direction to horizontal once it reaches the hydrocarbon-rich formation, e.g., shale formation. Horizontal wells allow the creation of larger fracture networks by creating staged fractures separated. The solids, i.e., proppants, used in the hydraulic fracturing fluid help propagate the fracture and keep the fracture open after pumping ends. Image taken from (Granberg, 2008)

Weng, 2015). After the completion of the staged pumping, the well is de-pressurized, which causes some of the injected fluid to flow back to the surface (flowback). Decreasing the pressure in the well causes the fracture aperture to decrease (e.g., fracture closure) and the compressive formation stress is transferred from the fluid to the proppant. This fracture aperture reduction traps the proppants between the fracture surfaces, therefore the solids are used to 'prop' open the fracture.

The fluid used in hydraulic fracturing is typically composed of water ($\sim 87\%$), sand ($\sim 13\%$), and chemical additives ($\sim 0.05\%$) (U.S.EPA, 2016). The chemical additives and quantities

in the hydraulic fracturing fluid vary greatly among operators and may depend on the type of reservoir being stimulated. Chemical additives may include acids, pH stabilizers, friction reducers, biocide, scale and corrosion inhibitors, breakers, foamers, surfactants, cross-linkers, and polymers (e.g., guar-gum) (Economides and Nolte, 2000). Adding guar-gum gives the fracturing fluid a shear-thinning rheology, with relatively high viscosity at low shear rates and low viscosity at very high shear rates. The high viscosity at low shear rates decreases the proppant settling velocity and the lower viscosity at higher shear rates allows the transport of proppants over long distances. The amount and distribution of proppant delivered to the fracture is of extreme importance as it provides the long term conductivity of the fracture.

1.2 Motivation

Hydraulic fracturing has improved significantly since it was first introduced in the 1940's. Advances in understanding the mechanisms controlling fracture creation and orientation, and improvements to the base fluid and proppants have made the technique more efficient and cost effective. Improvements to hydraulic fracturing have led to the creation of longer fractures, stimulating larger reservoir volumes using horizontal drilling, which allows the creation of staged fractures, and increasing proppant delivered to the fracture. However, the fracture permeability and thus production rates are limited by the properties of the the proppant delivered to the fracture.

Understanding the behavior of suspended proppant as it flows through the fracture is important because the suspension behavior determines the proppant distribution within the fracture. Figure 1.2 shows a schematic of a horizontal well with three staged hydraulic fractures. The fluid and suspension are injected into the well to create the fracture which opens in the direction of the least principal stress (σ_h), creating two surfaces separated by a distance b or aperture. The fracture propagates radially out of the well in the plane of the

greatest (σ_V) and intermediate principal stresses (σ_H), e.g., the fracture plane is in the x-y plane in the schematic shown in Fig. 1.2. Due to principal-stress anisotropy the fracture will propagate further into the formation along the intermediate stress than along the highest principal stress, giving the fracture an oval-like shape. The two-dimensional fracture geometry is typically modeled as an ellipse whose minor and major axes vary over the length of the fracture, therefore the aperture varies along both x- and y-axes, $b(x, y)$ (PKN model) or modeled with uniform width and a rectangular cross section, e.g., the aperture only varies along the x-axis, $b(x)$ (KGD model) (Economides and Nolte, 2000). Considering a region in the middle of the propagating fracture, the fracture can be approximated as a parallel-plate fracture with a separation distance given by the aperture, b.

Treating the hydraulic fracture as a parallel-plate fracture has allowed for the theoretical and experimental understanding of proppant behavior as it flows through the fracture. Much of the previous suspension-flow studies through fractures have focused on quantifying the distribution of solids and velocity across the fracture aperture, e.g., in the z-direction. This work revealed that suspended solids flowing through a parallel-plate fracture tend to develop large velocity and concentration gradients with a *plug* of concentrated solids forming in the middle of the fracture. The solid distribution across the aperture is assumed to be the same across the height of the fracture, which leads to the assumption that proppants are evenly distributed within the fracture and form a single (or multiple) layer of evenly distributed particles across the entire fracture width (Fig. 1.2b). In this dissertation I explore the behavior of concentrated suspensions and the effects on solid distribution across the fracture-plane to understand the applicability of uniform solid layers across the fracture width. The assumption of uniform proppant distribution across the width of the fracture is of great importance because this assumption determines the expected fracture geometry and the formation of uniform proppant layers, both which control the fracture permeability.

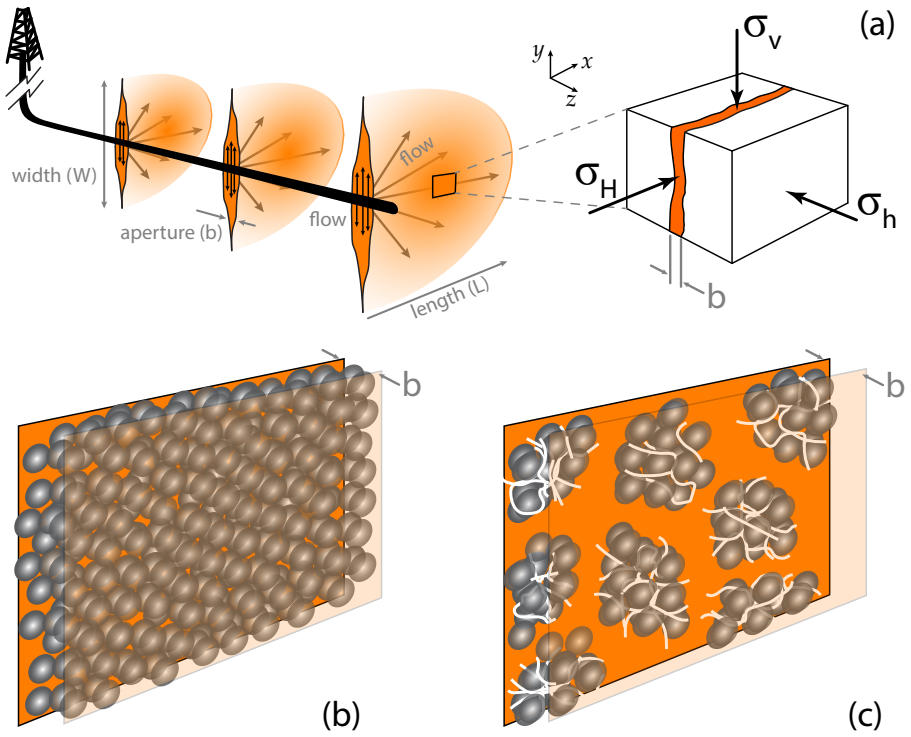

Figure 1.2: (a) Schematic showing horizontally directed well with three staged fractures. The fractures open in the direction of the least principal stress (z-direction) and propagate in the plane of the greatest and intermediate principal stresses (x-y plane). Schematic depicting (b) uniform proppant placement across the fracture plane and (c) localized-channelization induced by the addition of fibers to conventional proppants.

Recently, a new method to improve fracture permeability was introduced which aims to create a discontinuous proppant placement within the fracture. Such discontinuous proppant packs may be achieved by injecting proppant in short pulses, alternating with pulses of proppant free fluid (Gillard et al., 2010). In this *channelized fracturing* method, the proppant was amended with fibers keeping the particles together in the form of individual clusters (Fig. 1.2c). Therefore, hydrocarbons flow through the channels separating the proppant clusters rather than flowing through the proppant pack. A recent technique, *in situ channelization*, proposed that the discontinuous proppant placement may be achieved by adding fibers to the proppant (Potapenko et al., 2016). This technique does not require the alternating injection of proppant pulses, but instead relies relies on the interactions between sand proppants and fibers to form the proppant clusters leading to channelization. Studies of the interactions

between sand and fibers have largely been limited to geomechanical experiments looking at the compressive and shearing strength changes in the sand due to the addition of fibers (Diambra et al., 2010; Eldesouky et al., 2016) or rheology modifications to suspensions by adding fibers (George et al., 2011, 2012; Guo et al., 2005; Rajabian et al., 2008). In this dissertation I explore the behavior of semi-dilute suspensions of proppant and fibers as they flow and settle inside a hydraulic fracture. The experiments and numerical simulations presented here aim to quantify the fracture permeability enhancement due to the addition of fibers.

1.2.1 Goals of the present study

The focus of the work presented within this dissertation is to investigate the behavior of conventional (sand-only) concentrated suspensions and multi-component (sand-fiber) semi-dilute suspensions as they flow through and settle inside a hydraulic fracture. The objectives of the work presented in this dissertation are:

- Understand the flow behavior of concentrated suspensions as they flow through an idealized two-dimensional (e.g., rectangular slot) hydraulic fracture. It is hypothesized that the solid distribution across the fracture plane is equally important as the distribution across the aperture, in controlling fracture permeability. In addition, it was hypothesized that small variations in solid volume fraction (ϕ) in concentrated suspensions will have a significant effect on the suspension rheology and the flow behavior of the suspension.

- Investigate the behavior of concentrated suspensions in two-dimensional fractures (e.g., rectangular slot) with a complex geometry induced by obstructions that create shear stresses in multiple directions within the fracture and increasingly three-dimensional velocity field. It was hypothesized that shear-rate gradients in multiple directions

normal to the direction of flow have a significant effect on the solid volume fraction distribution across the fracture plane

- Investigate the behavior of multi-component proppants, e.g., sand and fibers, as they flow through and settle inside a hydraulic fracture and the effect of heterogeneous proppant placement on fracture permeability. It was hypothesized that the addition of fibers to conventional sand-polymer proppants may increase fracture permeability by creating heterogeneous proppant distributions within the fracture. This heterogeneous proppant distribution is the result of particle interactions between sand, fibers and polymer that lead to the formation of complex networks of interconnected sand and fiber particles. We hypothesize that these sand-fiber *networks* are stable enough to support an applied stress.

1.3 Outline of Dissertation

In Chapter 2, I review relevant literature on the behavior of suspensions as they flow through and settle in idealized confined flow geometries, e.g., tubes and rectangular channels. A review of fiber suspensions is presented. Finally a review of recent numerical simulations and experiments of sand and fiber mixtures in hydraulic fracturing applications is presented.

In Chapter 3, I explore the influence of solid volume fraction (ϕ) heterogeneity in a concentrated suspension flowing through a confined rectangular channel. It was observed that concentrated suspensions flowing through parallel fractures developed a non-uniform velocity distribution across the fracture width (in the plane of the fracture) which was significantly different than theoretically expected velocity distributions. The regions adjacent to the no-flow boundaries had the highest suspension velocity, while the free-stream velocity in the middle of the fracture was the lowest. The cause of these high-velocity regions was explored

using a depth-averaged model by simulating three possible scenarios that may lead to such velocity distributions.

In Chapter 4, the non-uniform velocity distribution across the fracture plane, observed in Chapter 3 are further explored by placing obstructions inside the fracture. Experiments presented in this chapter confirm that the mechanism responsible for these velocity variations was ϕ-gradients in the plane of the fracture. The experiments also revealed the timescale required for pressure gradient across the fracture, ∇P, to reach steady-state was much longer than expected for concentrated suspensions flowing through an idealized fracture. The cause of these ϕ-gradients and transient ∇P was explored by using 2-dimensional numerical simulations of concentrated suspensions flowing in confined geometries.

Chapter 5 explores the behavior of fiber-sand proppant mixtures inside a fracture; the response of the proppant to an applied stress is explored in this chapter. The experiments presented in this chapter investigate the behavior and distribution of solids as they flow through a parallel-plate fracture. I investigate the response of these sand-fiber proppants to an applied normal stress, σ_n. A method to estimate ϕ of sand within the fracture is proposed and used to quantify solid distribution within the fracture. This chapter also explores the response of the resulting solid distribution to fluid flowback (e.g., injection of solids-free fluid) within the fracture. Finally, Chapter 5 explores the effects of flowback and heterogeneous solid distribution on the fracture permeability.

Chapter 6 offers some concluding remarks and future research directions for the work presented in this dissertation.

Chapter 2

Literature review

2.1 Introduction

Understanding the behavior of proppants as they flow through and settle inside hydraulic fractures is critical to predict fracture permeability in hydraulic fracturing. In hydraulic fracturing, a suspension (in this work *suspension* means solid particles dispersed in a continuous liquid phase, e.g., base fluid or carrier fluid) is injected into the fracture to help propagate the fracture into the reservoir. After injection of the suspension stops, the pressure at the well is reduced and the formation stress is transferred from the fluid to the proppants, and as a result, proppants are trapped between the fracture surfaces. Therefore, the permeability of the completed hydraulic fracture depends on the proppant properties (e.g., material, stiffness, strength, mean particle size, particle size distribution, etc.), amount of proppant delivered, and the distribution of the solids, which affects the structure of the voids and thus the permeability of the porous sand pack. In this chapter I review the properties of the most common carrier fluid used in hydraulic fracturing, e.g. guar. I review and explore the flow and settling behavior of suspensions. Finally, I review the literature on experimental

and theoretical behavior of fiber suspensions and experimental behavior related to sand-fiber mixtures.

2.2 Hydraulic fracturing fluids: guar gum

When hydraulic fracturing was first introduced, gasoline-based napalm was used as the base fluid (Clark, 1949). Environmental and safety concerns associated with oil-based fracturing fluids prompted the development of water-based fracturing fluids. Using water as a base fluid required the addition of chemicals to increase the fluid's viscosity in order to increase the proppant carrying capacity of the fluid. Polymers , e.g, guar-gum or xanthan-gum, are typically added to water to increase the fluid's viscosity. The most widely used polymer in hydraulic fracturing is guar and guar-derivatives, which come from the guar plant or cluster bean (*Cyamopsis tetragonolobu* or *C. psoraloides*). Guar has a chemical structure that consists of long (1-4)β-D-mannose backbone chain with (1-6)α-D-galactose side-branches (Figure 2.1) (Chudzikowski, 1971). The ratio of mannose to galactose depends on the source of the guar bean, however, most studies report a ratio of $\sim$1:2 (Chudzikowski, 1971; Montgomery, 2013). The relatively high galactose content makes guar more soluble and a better stabilizer than most polymers (Mudgil et al., 2014). In addition, the galactose branches serve as the connection points to cross-link guar gum (Kesavan and Prud'Homme, 1992). Guar cross-linking is typically used to increase its viscosity and consistency which yields a gel-like fluid capable of carrying higher amounts of solids.

2.2.1 Carrier fluid rheology

Polymeric fluid rheology is highly dependent on the molecular composition of the polymer, the structure formed after mixing the polymer and liquid (e.g., during hydration), and the

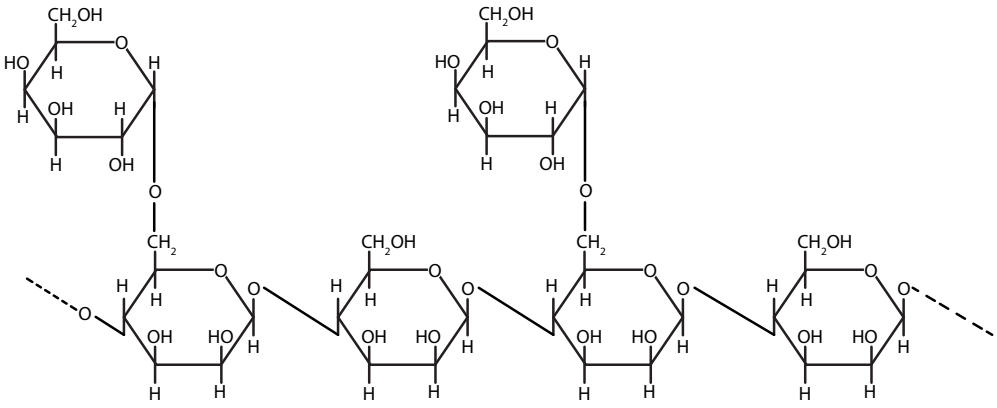

Figure 2.1: Chemical structure of guar-gum. The long chain is composed of β-D-mannose and the side-chains are α-D-galactose. (Chudzikowski, 1971).

concentration of guar used in the mixture. In general, guar-based fluids tend to exhibit a shear-thinning viscosity (decreasing apparent viscosity as the shear rate increases) with a relatively high viscosity at low shear rates. The apparent viscosity (η) of guar-based fluids approaches a constant value, referred to as the fluid's Newtonian limit (η_0), at low shear rates ($\dot{\gamma}$). Above a critical $\dot{\gamma}$, the viscosity of guar-based fluids exhibit a strong shear-thinning behavior descrived by the power-law. However, at very high shear-rates, the viscosity reaches a second plateau, η_∞. These two Newtonian plateaus (η_0 & η_∞) are controlled by the guar-links formed during the hydration process and the molecular weight of guar (Lei and Clark, 2004). Symbols in Figure 2.2 shows the represantative rheological behavior of guar-based fluids. The shear thinning behavior makes guar-gum one of the preferred carrier fluids in hydraulic fracturing because the high viscosity at low shear-rates reduces settling velocity helps transport proppants over long distances which leads to the formation of longer fracture and increased productivity.

The shear thinning behavior of guar-based fluids has been extensively studied; this behavior can be approximated by one of the established viscosity models. Here I present a short review of some relevant rheological models for shear-thinning fluids. One of the most common shear-

thinning viscosity models is the power-law or Ostwald-De Waele model given by (Chhabra, 2006):

$$\eta = m\dot{\gamma}^{n-1} \tag{2.1}$$

where η is the apparent fluid viscosity [Pa·s], $\dot{\gamma}$ is the shear rate [s^{-1}], m is the fluid consistency index [Pa· s^n], and n is the shear-thinning index [$-$]. Note for a Newtonian fluid $n = 1$ and $m = \eta$. The power-law model approximates the shear-thinning behavior of guar-based fluids, however, it does not capture the limiting viscosity at low shear rates ($\lim_{\dot{\gamma}\to 0}\eta = \eta_0$, i.e. zero shear viscosity) or high shear rates ($\lim_{\dot{\gamma}\to\infty}\eta = \eta_\infty$, infinite shear viscosity) (Figure 2.2). Additionally, the power-law model predicts the apparent viscosity of the fluid will decrease indefinitely with increasing shear-rate. Therefore, other rheological models are preferred over the power-law model.

Other models have been developed to describe the rheological behavior over a larger range of shear rates. Carreau (1972) developed a shear-thinning model based based on molecular network theory given by:

$$\eta = \eta_\infty + \frac{\eta_0 - \eta_\infty}{[1 + (\lambda\dot{\gamma})^2]^{(1-n)/2}} \tag{2.2}$$

where η_0 and η_∞ are the zero-shear and infinite-shear viscosities [$Pa \cdot s$], respectively, $n(< 1)$ is the shear-thinning behavior index [-], and λ is the relaxation time of the fluid [s]. This model captures the onset of the thinning behavior through the relaxation time, λ. For $\dot{\gamma} < {}^1/\lambda$ the viscosity approaches the zero-shear viscosity (Newtonian limit) and for $\dot{\gamma} >> {}^1/\lambda$ the viscosity approaches the infinite-shear viscosity. One possible downside of the Carreau model is the need to estimate four-parameters to describe the apparent viscosity.

The Cross model is similar to the Carreau model in that it captures the pseudo-plastic behavior of fluids. However, the Cross model was developed based on the assumption that shear-thinning behavior is a result of the formation of structural linkages or units (Chhabra, 2006):

$$\eta = \eta_\infty + \frac{\eta_0 - \eta_\infty}{1 + \lambda\left(\dot{\gamma}\right)^n} \tag{2.3}$$

where $n(< 1)$ is the shear-thinning behavior index [-], and λ is the relaxation time of the fluid $[s]$.

The Ellis model is a three-parameter model that captures the Newtonian plateau, η_0, and assumes a persistent power-law behavior through the high shear rate limit. The Ellis model defines the apparent viscosity as a function of shear stress ($\eta = f(\tau)$) instead of $\dot{\gamma}$ and is given by:

$$\eta = \frac{\eta_0}{1 + \left|\frac{\tau}{\tau_{1/2}}\right|^{1-\beta}} \tag{2.4}$$

where η_0 is the zero-shear viscosity, τ is the shear stress [Pa], $\tau_{1/2}$ is the value of the shear stress at which the apparent viscosity is half of the zero-shear viscosity ($\eta_0/2$), and $\beta(> 1)$ is the shear-thinning index [-].

2.2.2 Suspension rheology

Adding particles to the suspending fluid (carrier fluid) can have a significant effect on the rheology of the suspension. The suspension rheology depends on the physical and chemical properties of the particles and the fluid, as well as mechanical and hydrodynamic interactions

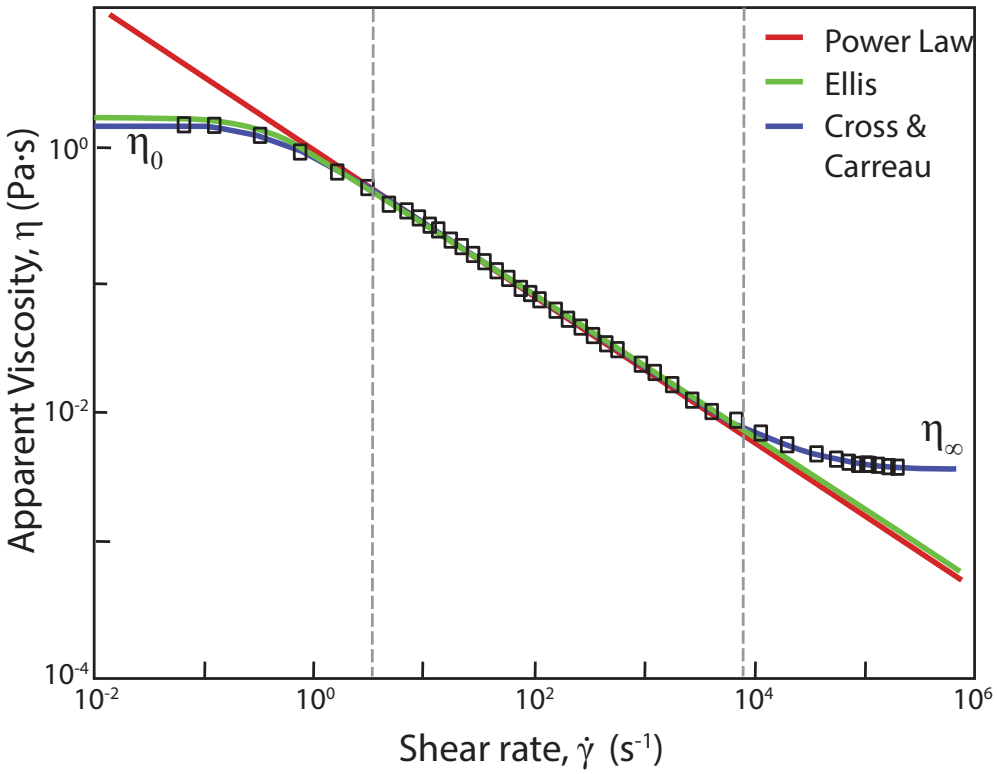

Figure 2.2: Behavior of different shear-thinning (pseudo-plastic) rheology models. The symbols show the representative behavior of polymeric fluids. The Power-Law (Ostwald-De Waele) model captures the shear-thinning behavior over a limited range of $\dot{\gamma}$ and does not capture either of the Newtonian plateaus at very low or very high shear rates, η_0 or η_∞. Both the Cross and Carreau models capture the shear-thinning behavior and the viscosity limits, however, these models have four parameter estimates. The Ellis model sets $\eta = f(\tau)$ instead of $\dot{\gamma}$. The Ellis model, captures the Newtonian limit at low $\dot{\gamma}$ and the onset of shear-thinning behavior. This model does not capture the second plateau, however, it only needs three parameters. (Chhabra, 2006).

between the fluid and particles. Understanding the rheological properties of suspensions is important to determine mechanical behavior of the suspensions such as flow rate, internal forces, particle velocity and deposition rates of particles as the suspension is transported. From an engineering perspective, knowing the rheology of the suspension is important for the design of pipelines, pumps, conveyors, and other transport mechanisms/instruments.

One of the main factors affecting the suspension rheology include particle volume fraction (ϕ defined as the ratio between the volume of the particle phase and the total volume), shape

and spatial distribution of the particles, interactions between particles, as well as the motion of the bulk flow (Mueller et al., 2009). Much of the research has focused on the effect of ϕ on the apparent viscosity of the suspension η. Suspensions are typically categorized into three distinct regimes (dilute, concentrated, and dense) based on the solid concentration. In the *dilute* regime ($\phi \lesssim 0.2$), the distance between particles is large (compared to the particle radius) and hydrodynamic interactions between suspended particles are negligible. Dilute suspensions exhibit Newtonian behavior and their viscosity increases linearly with ϕ (Deboeuf et al., 2009). Einstein (1906) proposed a first-order linear relationship for viscosity of dilute suspensions, $\eta_r = \eta_s/\eta_f = 1 + \mathrm{B}\phi + \mathcal{O}(\phi^2)$, where η_f, η_s, and η_r is the fluid, suspension, and relative viscosity, respectively, and $\mathrm{B} = 2.5$ for spherical particles. This was later extended to a second-order approximation, $\eta_r = 1 + \mathrm{B}\phi + \mathrm{B}_1\phi^2 + \mathcal{O}(\phi^3)$, with $\mathrm{B}_1 \approx 5.2 - 7.6$ and $\mathrm{B} = 2.5$ (Batchelor and Green, 1972). Both models agree with experimental observations of dilute suspension's apparent viscosity, however, the apparent viscosity given by both models deviate for suspensions with higher ϕ.

As ϕ increases, the number of particles increases and the separation distance between particles decreases, therefore, particle-particle interactions can no longer be ignored. These particle-level interactions lead to hydrodynamic interactions which give rise to the non-Newtonian behavior of the suspension (Brady, 1993). In the *concentrated* regime, ϕ between ~ 0.2 and the random lose packing limit ($0.2 \lesssim \phi \lesssim \phi_{rlp}$), the apparent viscosity of the suspension increases significantly as ϕ increases (Boyer et al., 2011a). Maron and Pierce (1956) proposed an empirical equation for the apparent viscosity of concentrated suspensions, $\eta_r = (1 - {}^{\phi}/_{\phi_m})^{-2}$, which agrees with much of the experimental data available for suspension rheology (Stickel and Powell, 2005). The maximum solid volume fraction ϕ_m represents a state in which particles have reached their optimal or 'closest' configuration, as a consequence, it is often used to represent the suspended particles' microstructure (Stickel and Powell, 2005). Other proposed models, which are in excellent agreement with empirical results, have been proposed (Chong et al., 1971; Frankel and Acrivos, 1970).

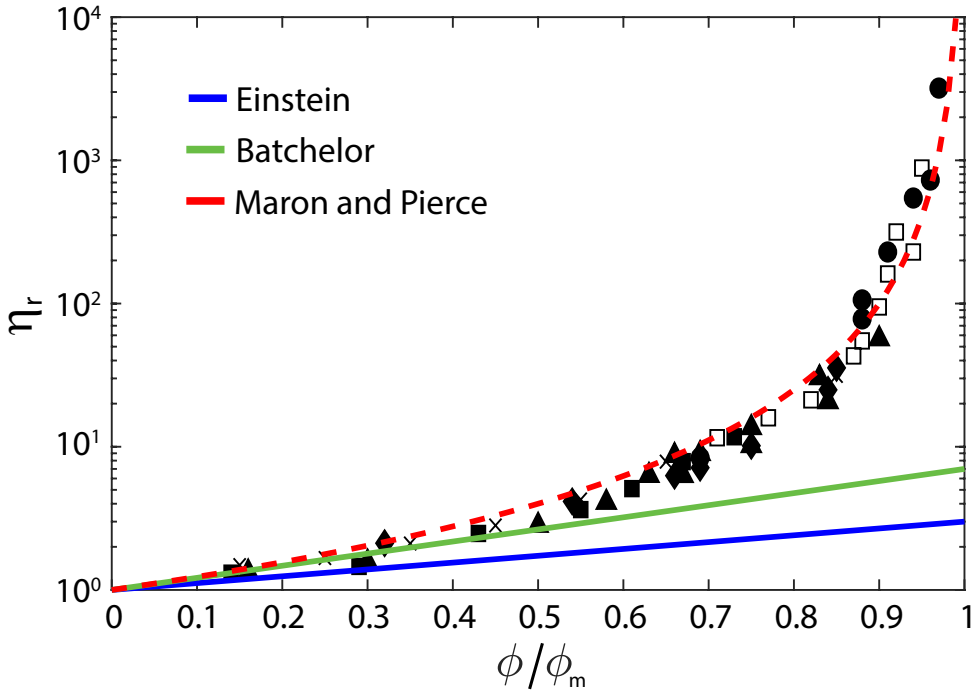

Figure 2.3: Relative viscosity (η_r) of suspensions as a function of ϕ/ϕ_m. Data is taken from Chang and Powell (1993)

In the *dense* regime ($\phi_{rlp} \lesssim \phi$) the particle microstructure or the relative arrangement of the particles may have a significant effect on the rheological and flowing behavior of the suspension. At high ϕ values the concentration may exhibit yield stress behavior (Boyer et al., 2011a). If the suspension concentration reaches a critical value ϕ_{cr}, between the random-loose packing and close-packing limit ($\phi_{rlp} \leq \phi_{cr} \leq \phi_{rcp}$) the suspended particles may jam (or clog) (Haw, 2004). For spheres, $0.55 \lesssim \phi_{cr} \lesssim 0.64$, however, ϕ_{cr} depends on the particle shape and polydispersity. When the suspension is jammed, solids are immobilized and can resist a finite shear stress (Shapiro and Probstein, 1992; Haw, 2004). Therefore, the jammed suspensions exhibit properties similar to those of a solid and effectively become a fixed porous medium with fluid moving through the pore spaces. The permeability of the suspension thus decreases to that of a porous medium composed of the jammed (immobile) solids.

In addition to ϕ, suspension viscosity depends on the particle size distribution of the particles. Shapiro and Probstein (1992) showed that fluids mixed with bi-modal and multi-modal sand distributions typically have lower apparent viscosity than the same fluid mixed with monodisperse particle size distribution at the same concentration. The lower viscosity of polydispese suspensions was attributed to the higher fluidity limit (ϕ_{cr}) of polydisperse suspensions.

2.3 Introduction to suspension flow

Suspension flow in hydraulic fracturing is typically represented as flow through tubes (Cox and Mason, 1971) or parallel-plate channels (Lyon and Leal, 1998a). Suspension flow through porous and fractured media have been observed to exhibit complex behavior and often defy simple relationships between applied pressure gradient and flow rate. At high shear rates, the presence of the solids typically causes shear-thinning behavior; at low shear rates, a yield stress is common due to possible settling of particles within the suspension (Lecampion and Garagash, 2014). This behavior is especially important in fractures, where the suspension may experience significant variation in shear stresses over a relatively short distance.

Suspensions flowing through tubes and parallel plates have been observed to experience particle migrations transverse to the flow direction, from regions of high shear to regions of low shear. These particle migrations lead velocity profiles that deviate from the parabolic profile expected for Newtonian fluids. In their rheology measurements of concentrated suspensions, Gadala-Maria and Acrivos (1980) first noticed that the viscosity of suspensions in a constant shear experiment decreased over time even though the suspending fluid was Newtonian. Leighton and Acrivos (1987b) demonstrated that such behavior was due to shear-induced stresses that caused particles to migrate from regions of high shear to regions of low shear. These particle migrations were attributed to irreversible displacements caused

by inter-particle interactions and shear-stress gradients (Leighton and Acrivos, 1987a). They concluded the particle migration could be approximated by a diffusive process that scales with $a^2\dot{\gamma}$, where a is the particle radius and $\dot{\gamma}$ is the applied shear rate. Phillips et al. (1992) proposed a constitutive 'diffusive-flux model' to account for the shear-induced migrations described by Leighton and Acrivos (1987b). They identified threee mechanisms contributing to this 'diffusive-flux' of particles: (i) particle flux due to random particle collisions caused by shear-rate gradients ($\mathbf{N}_C$), (ii) particle flux due to particle interactions caused by viscosity gradients ($\mathbf{N}_\eta$), and (iii) flux due to collision due to Brownian motion ($\mathbf{N}_b$). For most suspensions of interest Brownian effects are negligible and this term is dropped.

The model proposed by Phillips et al. (1992) was limited to rectilinear flows, with particle displacements limited to the direction normal and parallel to gradients. The diffusive flux model failed to explain similar behavior in curvilinear flows. Krishnan et al. (1996) generalized the Phillips model for both rectilinear and curvilinear flows through the addition of curvature-induced migration flux ($\mathbf{N}_r$). The total particle flux in the diffusive flux model is the sum of fluxes due to shear-rate gradients, viscosity gradients, and curvature induced migration (see Figure 2.4 for a representation of these fluxes.) By adding the curvature flux, the diffusive-flux model was able to model particle migrations in multi-dimensional flows, including cone and plate rheometers and torsional parallel plate flows. A shortcoming of the model is that the diffusive process predicts ϕ in zero-shear regions (e.g., the center of axial flow through a tube) will always reach ϕ_m regardless of bulk suspension concentration, which leads to instabilities because the viscosity approaches infinity as $\phi \to \phi_m$. In practice, this is typically overcome by adding a local $\dot{\gamma}$ in the zero-shear line of symmetry.

Nott and Brady (1994) proposed the suspension balance model (SBM), also known as the suspension temperature model, in which particle migrations result from gradients in the particle-phase stress, not diffusion. Physically, this means that an inhomogeneous stress develops due to particle concentration and shear rate gradients. Particle migration is therefore

driven by normal stress differences that arise due to the presence of the particles in the bulk fluid. The *net* particle flux is proportional to the divergence of this particle stress tensor. The proposed model by Nott and Brady (1994) only accounted for isotropic particle-phase stress tensors and was later modified to include anisotropic stresses (Morris and Boulay, 1999) and extended to general flows (Miller and Morris, 2006). The SBM leads to a first-order-continuous particle concentration where $\dot{\gamma} = 0$ (e.g., center of a tube), whereas the diffusive-flux model leads to a discontinuity in the concentration gradient, because $\phi = \phi_m$ regardless of the bulk solid content of the suspension.

These particle migrations from regions of high shear rate (e.g., walls) towards regions of lower shear rate (e.g., centerline of tube/channel) results in ϕ-variations which may create local variations in the suspension viscosity (η_s) due to the non-linear dependence on the solid volume fraction (ϕ).

2.4 Introduction to suspension settling

Sedimentation of non-Brownian particles in quiescent fluids has been a topic of interest for many decades. Analytical solutions have been developed for the settling of a single particle (i.e. sphere, cylinders, and spheroids) in an infinite unbounded fluid domain (Batchelor, 1972, 1970; Cox and Mason, 1971) and relationships have been derived which include wall effects on the settling velocity of a single particle (Staben et al., 2003; Xue et al., 1992). Much of the work on spheres (or particles) settling in a quiescent fluid have been performed in Newtonian fluids (Happel and Bart, 1974; Xue et al., 1992). Settling of non-Brownian fluids in polymeric fluids (i.e. xanthan or guar gels) is of great importance for many different industrial applications, especially industries where the aim is to prevent particles from settling or at least decrease the settling rate of the particles, i.e. oil and gas production, and well installation as the drill cuttings (typically mixed with mud) need to be retrieved to the

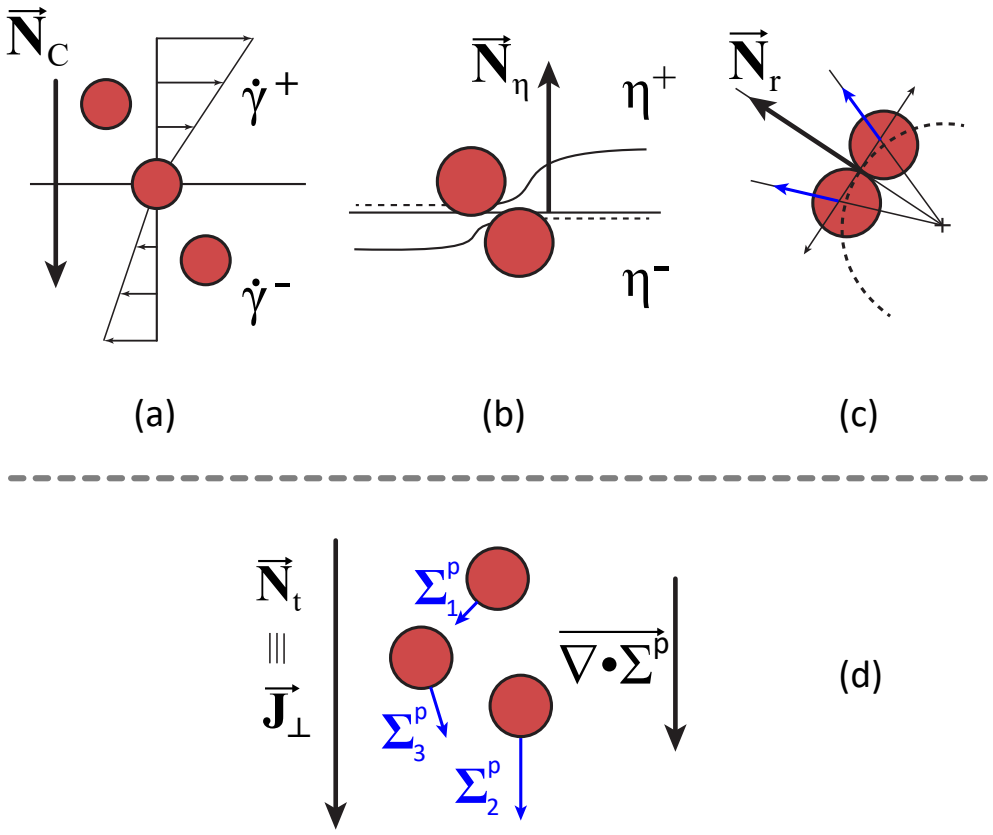

Figure 2.4: Migration mechanisms observed in flowing suspensions. Migration due to (a) shear rate gradients, (b) viscosity gradients, and (c) curvature induced migration. (d) represents the mechanism of the suspension balance model, in which the migration is due to the stresses the particles exert onto the fluid. Figure adapted from Dbouk (2013)

surface. The rheological properties of polymeric fluids make them ideal for the transport of suspended solids due to their high apparent viscosities. Over the past three-decades efforts have been made to improve the rheological properties and behavior of fluids used when injecting solids into a hydraulic fracture or transporting drill cuttings during well installation. One such advance has been the cross-linking of guar which increases the thickness of the fluid, creating the consistency and properties of a gel. Cross-linking of guar and guar derivatives has been shown to reduce costs by reducing the amount of polymer used, while keeping the same fluid properties, and are also believed to minimize formation damage (Lei and Clark, 2004).

Suspension settling exhibits complex behavior due to hydrodynamic interactions between all particles. As the particles settle, diffusion causes the suspension to form a concentration front that spreads across the width of the container in which the suspension is settling. In dilute suspension this spreading creates horizontal regions of constant and uniform ϕ which settle as a 'front'. Thus, ϕ will remain constant throughout the suspended layer and will only vary sharply at the suspension-clarified layer fluid interface and the sediment layer. In polydisperse suspensions, ϕ of the settling layer does not remain uniform. As particles settle, the larger particles (higher settling velocity) move away from smaller particles. These migrations leads to the creation of different layers in the settling container, separated by particle size.

The region just above the sediment layer (region 1), contains all the different particle species at their initial concentrations, while the region immediately above it does not contain the largest particles. Successive regions contain one less particle species than the region below, with the uppermost region containing only the slowest-settling (smallest) particles, followed by a clarified layer which is practically particle-free (Fig. 2.5). These regions are usually separated by a discontinuity in particle concentration distribution, i.e. shock. Though there are instances when the shock is a steep concentration gradient, particle diffusion will tend to smooth the concentration gradient, such that there is a sharp but continuous transition across each shock separating two regions of uniform concentration (Davis and Acrivos, 1985).

Suspensions settling within a container will have a slower settling velocity (hindered settling) than that predicted by Stokes due to interactions with the walls and inter-particle forces. Richardson and Zaki (Richardson and Zaki, 1954) proposed a semi-empirical formulation for the hindered settling velocity: $V = V_s(1-\phi)^n$, where V_s is the Stokes settling velocity of a single particle, ϕ is the solid volume fraction of the suspension, and the empirical exponent n depends on the particle Reynolds number $Re_p = \frac{\Delta\rho V_s a}{\eta_f}$; typical values of n fall in the range of 4.65-2.4 (Baldock et al., 2004).

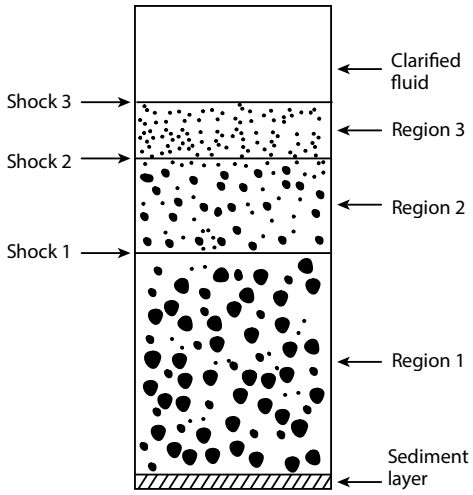

Figure 2.5: Development of three distinct sedimenting regions for a suspension composed of multi-modal particle size distributions in a Newtonian carrier fluid. Figure adapted from (Davis and Acrivos, 1985)

The settling velocity of suspensions can be reduced by increasing the solid concentration, ϕ, increasing the fluid viscosity η_f or decreasing the density difference, Δrho, between the fluid and the particles. The settling and flow behavior of suspensions described above, lead to the formation of a largely uniform proppant distribution in the fracture plane within the fracture surfaces. As a result, proppant inside hydraulic fractures are typically assumed to be uniformly distributed as a single or multi-layer of proppant within the fracture and little attention is given to the solid distribution across the fracture width.

2.5 Introduction to fibers as proppant additives

A new method to improve fracture permeability was proposed by Gillard et al. (2010), which aims to create a discontinuous proppant placement within the fracture. It was proposed that such discontinuous proppant packs may be achieved by injecting proppant in short pulses, alternating with pulses of proppant free fluid. In this *channelized fracturing* method, the proppant was amended with fibers that bind the particles together in the form of individual

clusters (see Fig. 1.2c). In *channelized fracturing* oil and gas flows through the channels separating the proppant clusters rather than flowing through the proppant pack. A recent technique, *in situ channelization*, proposed that the discontinuous proppant placement may be achieved by adding fibers to the proppant (Potapenko et al., 2016). *In situ channelization* does not require the alternating injection of proppant pulses, instead, this method proposed that fiber-fiber and fiber-proppant interactions lead to the formation of proppant clusters and ultimately channelization.

Fiber suspensions have been shown to exhibit complex settling behavior which is affected by the properties of the individual fibers, such as length, diameter, helicity, stiffness, fiber material, and fiber concentration (Herzhaft et al., 1996; Herzhaft and Guazzelli, 1999; Guazzelli and Hinch, 2011). The characteristic length scales for fibers, are given by the fiber shape, usually represented by cylinders having a length l and diameter d. Concentration of fibers in suspensions is related to the particle density of fibers, n, by $\phi_f = \frac{\pi}{4} n l^2 d$ (note that for spheres $\phi_s = \frac{4\pi}{3} n a^3$). Using the particle density and the dimensions of fibers, four non-dimensional parameters were derived: nl^3, nl^2d, nld^2, and nd^3 (Nicolai et al., 1995). Using these non-dimensional values and the dependence of ϕ on n three concentration regimes for fiber suspensions were defined (e.g., dilute, semi-dilute, and concentrated), similar to those regimes defined for spherical suspensions. A characteristic of the *dilute* regime, $1 \gg nl^3$, is that each fiber occupies a large volume ($\mathcal{O}(l^3)$), creating a large separation distance between fibers. Due to this large separation distance the fibers can rotate freely, therefore, interactions between individual fibers are negligible. As the fiber particle density increases, the probability of encountering more than one fiber within a volume of $\mathcal{O}(l^3)$ increases, therefore, the *semi-dilute* regime is defined as $nl^3 \gg 1 \gg nl^2d$ (Herzhaft and Guazzelli, 1999). In the *concentrated* regime, $nl^2d \approx 1$, the distance between fibers is small, as a consequence there is significant hydrodynamic interactions between fibers. In the concentrated regime, the suspension may experience a nematic phase transition in which fibers form approximately parallel formations (Guazzelli and Hinch, 2011). These definitions of the suspension regimes

suggest that the aspect ratio and concentration (or number density) have a significant effect on settling and flow behavior of fibers, especially confined geometries where the walls may exert forces on the fibers.

A fundamental difference between settling fibers and settling spherical particles is the orientability of fibers. A fiber with its long-axis oriented parallel to the direction of settling will have a higher settling velocity; while a fiber oriented perpendicular to the settling direction might experience higher drag and may drift in the direction perpendicular to the settling direction (Herzhaft et al., 1996). Settling fiber suspensions have been observed to form 'streamers' (e.g. vertical fiber structures) whose width may be in the order of a few fiber lengths; the height of these clusters is of the same order of magnitude as the height of the container (Herzhaft and Guazzelli, 1999; Metzger et al., 2007). As they settle, the fiber streamers may 'dissolve' or lose fibers from the main stream into the fluid space and 'grow', e.g., capture loose fibers (Metzger et al., 2005; Guazzelli and Hinch, 2011). Fiber-level simulations have observed that flexible and semi-flexible fibers tend to form 'clusters' or 'agglomerates' of interlocked fibers (Schmid and Klingenberg, 2000a,b; Saintillan et al., 2005; Switzer III and Klingenberg, 2003; Switzer and Klingenberg, 2004).

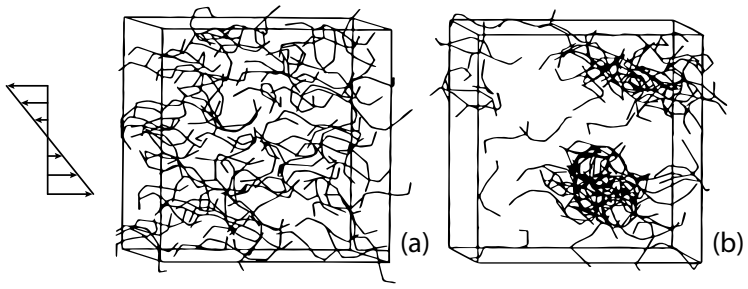

Figure 2.6: Fiber flocs or agglomerates formed due to frictional and interlocking effects in sheared suspensions (Schmid and Klingenberg, 2000a).

2.6 Interaction between solid particles and fibers in suspensions

Suspensions with high particle densities have been observed to have a complex flow and settling behavior. The complexity of suspensions is a result of long-range hydrodynamic interactions between suspended particles. In suspensions of spherical particles, hydrodynamic interactions have been accounted for by defining a normalized probability distance function to a *test* particle and calculating the hydrodynamic force exerted on the *test* particle by any particle in the suspension (Batchelor, 1972; Herczynski and Pienkowska, 1980). The probability distance function is a direct function of the ϕ or particle density of the suspension. This normalization is significantly more complex for a fiber suspension due to the fiber's orientability and complicated agglomerating behavior. Similarly, solutions of hydrodynamic interactions in suspensions of solid spherical particles and fibers have not been developed. Much of the experimental and theoretical work has focused on the interaction of a single spherical particle in a suspension of fibers.

The settling velocity of a single particle in a suspension of uniformly dispersed fibers was reduced (compared to settling velocity in fiber-free fluid) and was observed to decrease as fiber concentration increased; these effects were the similar in both fiber suspensions in a Newtonian (Milliken et al., 1989; Harlen et al., 1999) and non-Newtonian base fluid (Elgaddafi et al., 2012, 2016). The observed decrease in settling velocity was attributed to the increased viscosity of the fluid due to the fiber addition (George et al., 2011; Guo et al., 2012, 2015). The decreased settling velocity of the spherical particle can be approximated by introducing a drag coefficient which is a function of fiber content of the suspension (Milliken et al., 1989; Elgaddafi et al., 2012). Pradhan et al. (2013) simulated fiber suspension with different levels of anisotropy, which describes the overall fiber orientation, e.g., from high (parallel fibers) to low (intertwined fibers) fiber orientation. They simulated flow of particles

through the suspension and found the the permeability of the suspension was inversely proportional to the suspension anisotropy, e.g. low anisotropy suspensions (highly oriented fibers) had the highest permeability, suggesting that anisotropy could lead to interlocking of sand and fiber particles.

The clumping behavior of fibers described above and the viscosity modifications to the carrier fluid as a result of adding fibers has the potential to increase fracture permeability by creating a heterogeneous solid distribution capable of supporting closure stresses. Previous experiments have demonstrated that adding fibers to sand significantly improved the mechanical response of the fiber-reinforced soils under different stress conditions. Isotropic compression and shearing experiments have demonstrated that fiber-reinforced sand specimens have a higher compressive strength (Diambra et al., 2010, 2013; Diambra and Ibraim, 2015; Consoli et al., 2005) and shearing strength (Eldesouky et al., 2016; Tang et al., 2007), than those sand specimens without fibers. It has also been observed that fibers may reduce particle crushing in well graded sands subjected to uni-axial compression(Pino and Baudet, 2015).

The increased strength of fiber-reinforced sands suggests that adding fiber to sand proppants may help the proppant support the compressive stress from the formation. Sand-fiber proppant experiments in hydraulic fracturing have demonstrated that adding fibers to conventional sand proppants reduced proppant back-production (Card et al., 1995). Recent experiments have demonstrated that adding fibers to sand proppants led to the formation of a heterogeneous proppant distribution inside the fracture (Yang and Wen, 2017; Liang et al., 2018). These solid distributions showed that fiber-sand clumps had a highly irregular shape. Numerical simulations of flow through heterogeneous proppant placements increase fracture conductivity at low closure stress (Ejofodomi et al., 2014; Hou et al., 2016; Zheng et al., 2017), however, at very high closure stresses the sand-fiber proppants may actually reduce permeability (Hou et al., 2017).

Chapter 3

Flow of concentrated suspensions through fractures: Small variations in solid concentration cause significant in-plane velocity variations

3.1 Abstract

Flow of high-concentration suspensions through fractures is important to a range of natural and induced subsurface processes where fractures provide the primary permeability (e.g., mud volcanoes, sand intrusion, and hydraulic fracturing). For these flows, the simple linear relationship between pressure gradient and flow rate, which applies for viscous-dominated flows of Newtonian fluids, breaks down. We present results from experiments in which a high concentration (50% by volume) of granular solids suspended in a non-Newtonian carrier fluid (0.75% guar gum in water) flowed through a parallel-plate fracture. Digital imaging

and particle-image-velocimetry analysis provided detailed two-dimensional maps of velocities within the fracture. Results demonstrate development of a strongly heterogeneous velocity field within the fracture. Surprisingly, we observed the highest velocities along the no-flow boundaries of the fracture and the lowest velocities along the centerline of the fracture. Depth-averaged simulations using a recently developed model of the rheology of concentrated suspensions of mono-disperse solids in Newtonian carrier fluids reproduced experimental observations of pressure gradient versus flow rate. Results from additional simulations suggest that small (3%) variations in solid concentration within the fracture can lead to significant (factor of two) velocity variations within the fracture yet negligible changes in observed pressure gradients. Furthermore, the variations in solid concentration persist over the length of the fracture, suggesting that such heterogeneities may play a significant role in the transport of concentrated suspensions. Our results suggest that a simple fracture-averaged conductivity does not adequately represent the transport of suspended solids through fractures, which has direct implications for subsurface suspension flows where small concentration variations are likely.

3.2 Introduction

Subsurface flows of fluids with high concentrations of suspended solids are important to a range of naturally occurring and applied problems. Naturally occurring phenomena such as intrusion of magmas composed of crystals suspended in silicate melts (Mader et al., 2013) and mobilization of suspended sediments in the shallow crust such as sand intrusion in sedimentary basins (Huuse et al., 2010) and mud volcanoes (Manga and Brodsky, 2006) involve migration of fluidized solids through preexisting or propagating fractures. Engineering applications include environmental remediation (Murdoch et al., 2006), mud injection during drilling (Bittleston et al., 2002), and injection of slurries containing high concen-

trations of sands during hydraulic fracturing for both oil and gas production (Kern et al., 1959; Montgomery, 2013). Suspended solids can alter fracture transmissivity if they become immobilized within the fracture or if their concentration is sufficiently large to change the suspension rheology.

The volumetric concentration of solids in a suspension, ϕ, strongly influences its rheology. In dilute suspensions ($\phi \lesssim 0.2$), interactions between particles are negligible and the rheology of the suspension is similar to that of the suspending fluid, with the effective viscosity, η, increasing with ϕ (Krieger and Dougherty, 1959). Even at very low ϕ, particles may bridge or clog at pore throats leading to reduced permeability (Khilar and Fogler, 1998). These permeability reductions may be reversed when the clogged particles are remobilized due to earthquake-induced shaking or pressure oscillations (Elkhoury et al., 2006, 2011). When ϕ approaches a critical limit, ϕ_{cr}, between the random loose- and dense-packing limits for the solids ($0.55 \lesssim \phi_{cr} \lesssim 0.64$), the particles become completely jammed and abruptly change to a rigid porous medium (Haw, 2004). The permeability then decreases to that of a porous medium composed of the jammed solids. Subsequent large pressure perturbations can lead to fluidization of the jammed solids and remobilization (e.g., mud volcanoes). Here we are interested in intermediate concentrations ($0.2 \lesssim \phi \lesssim 0.55$) where fluid and solid flow together but particle-particle interactions are non-negligible leading to frictional losses that significantly alter the rheology of the suspension from that of the suspending fluid.

Over the past decade, frictional models for the behavior of dry granular solids have been extended to represent the behavior of solids suspended in viscous fluids. Early efforts focused on flows of granular solids down inclined planes (Cassar et al., 2005; du Pont et al., 2003), and established the importance of the dimensionless 'viscous number', $I_v = (\eta_f \dot{\gamma}/P_s)$, which relates the timescale of the movement of a single particle subjected to a force $P_s d^2$ (where P_s is the pressure acting on a solid particle of diameter, d) in a fluid with viscosity, η_f, to the timescale of the displacement of a particle caused by the imposed shear rate, $\dot{\gamma}$. Boyer et al.

(2011a) demonstrated that relationships of the form $\tau = \eta(I_v)P_s$ can adequately quantify the shear stress and proposed corresponding constitutive relationships for the effective friction coefficient, $\eta(I_v)$, and volume fraction, $\phi(I_v)$. As shear rate (or I_v) increases, $\phi(I_v)$ decreases from a maximum of ϕ_{cr} when $I_v \to 0$ and $\eta(I_v)$ increases from a minimum when $I_v \to 0$. In pressure-driven, internal flows (e.g., tubes and fractures), where the shear rate is maximum at the walls and vanishes along the centerline, the dependence of η and ϕ on I_v gives rise to plug-flow behavior for larger values of ϕ_o (the average solid concentration of the well-mixed suspension and the uniform concentration at the inlet). The result is a localized region of high shear rate near the walls where $\phi < \phi_o$ and a region in the center of the flow where $\phi \to \phi_{cr}$ and the fluid and solid move at the same velocity. Lecampion and Garagash (2014) extended the constitutive relationships for $\phi(I_v)$ and $\eta(I_v)$ proposed by Boyer et al. (2011b) to develop a model for pressure driven flows through tubes and channels.

Parallel-sided channels provide an idealized analog to fractures in geologic systems where fractures typically have rough walls that may also be permeable. However, as with early studies of Newtonian (Witherspoon et al., 1980) and non-Newtonian (Di Federico, 1997) fluid flow in fractures, beginning with this idealized geometry provides a well-controlled step towards understanding more complicated geometries. The emphasis of previous suspension-flow studies in channels was to quantify the distribution of solids and velocity across the gap between the surfaces (or aperture). Here, we consider larger three-dimensional flow fields, where the velocity may also vary in the plane of the fracture. We are particularly interested in the influence of boundary conditions on suspension flows. In experimental and computational studies of fluid flow through fractures, uniform pressure is typically applied along two boundaries to create the pressure gradient that drives flow. When studying suspension flows, it is also necessary to prescribe ϕ_o at the inlet boundary. The obvious choice is to also assume uniform ϕ_o, but due to the strong dependence of η on ϕ, small variations of ϕ within the flow field can cause variations and instabilities in the velocity field. In addition, many previous studies of the rheology of concentrated suspensions focused on idealized mono-disperse

(Karnis et al., 1966; Lyon and Leal, 1998a,b) or bimodal (Lyon and Leal, 1998b) spherical solids. Here we explore the implications of the complex rheology of a mixture of guar and silica sand representative of suspended solids encountered in the subsurface. In particular, we focus on conditions where suspended solids flow with the fluid and we do not consider conditions under which the settling of solids within the fracture is important.

We present results from a pair of experiments in which we flowed high-solid-concentration fluid through a parallel-sided fracture with two different boundary-condition configurations. To aid in interpreting the results of the experiments, we simulated flow through the experimental system using the rheological model of Lecampion and Garagash (2014).

3.3 Overview of Experiments

We designed an experimental apparatus to explore the role of suspension rheology and flow geometry on fracture flow. Transparent parallel-sided fractures provide the ability to both directly measure the flow geometry under experimental conditions and visualize and quantify the velocity field within the fracture. Here we describe the experimental apparatus, the details of the fluid-solid mixture used for the experiments, the configuration of the experimental system, and the procedure used to carry out the experiments.

3.3.1 Experimental apparatus

A rotating stand rigidly fixed a high-sensitivity 12-bit charge-coupled device camera (Photometrics Quantix KAF-6303e) above a monochromatic (red) light-emitting-diode panel. Clamps held the fracture cell to the stand between the light source and the camera. Two $\sim$0.3-cm-thick aluminum shims separated the two fracture surfaces (15cm $\times$ 15cm $\times$ 1.2cm smooth glass plates) and served as no-flow boundaries along the fracture edges. The frac-

ture cell secured the fracture surfaces while allowing visualization of the entire flow field. An electronic controller synchronized 65-ms pulses of the light source with the camera exposure to provide reproducible high-resolution (76 $\times$ 76 μm pixels) measurements of transmitted light intensity (Figure 3.1). Section 3.4 describes how we processed measured intensities to yield velocity fields.

We carried out two experiments in the same fracture with different inlet/outlet boundary conditions. Experiment A, used linear inlet and outlet manifolds (Figure 3.2) that included large rectangular channels that spanned both ends of the fracture. Initially, a high-capacity syringe pump pushed slurry into one end of the inlet manifold (blue arrow) and out a waste line at the other end of the inlet manifold (green arrow) filling the manifold with slurry. We then closed the waste line and opened the two outlets on either side of the outlet manifold (red arrows) to initiate flow through the fracture. Experiment B, used a wedge-shaped manifold (Figure 3.2) that allowed us to flow directly into the fracture without pre-filling the manifold. This configuration included only a single inlet and a single outlet tube. Furthermore, the wedge-shaped manifold tapers gradually from the inlet port (blue arrow) to a rectangle with the same width (W) and aperture (h) as the fracture. A differential pressure transducer connected to the ports located at the center of the inlet and outlet manifolds (marked by $\times$'s in both configurations in Figure 3.2) measured the differential fluid pressure (ΔP_f) across the fracture at high temporal resolution (0.3 Hz) during each experiment.

3.3.2 Fluid description and experimental configuration

For both experiments, we used a carrier fluid consisting of 0.75% by volume mixture of guar gum and water. This guar/water mixture is a shear thinning fluid that behaves as a Newtonian fluid under low shear rates and exhibits non-Newtonian behavior at higher shear rates (Figure 3.3). We selected guar because it is a well-characterized high-viscosity fluid

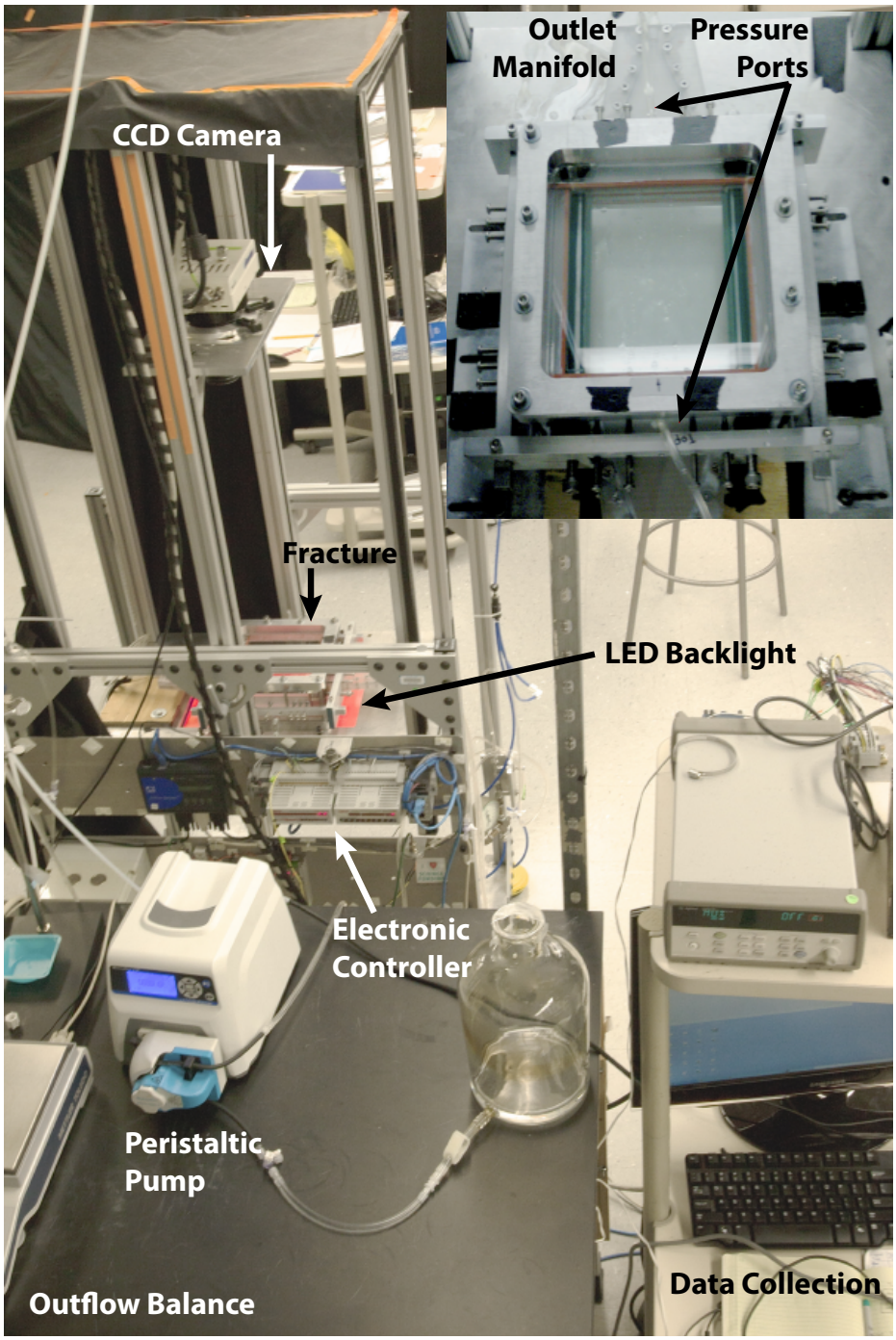

Figure 3.1: Photograph of experimental setup and fracture cell (inset).

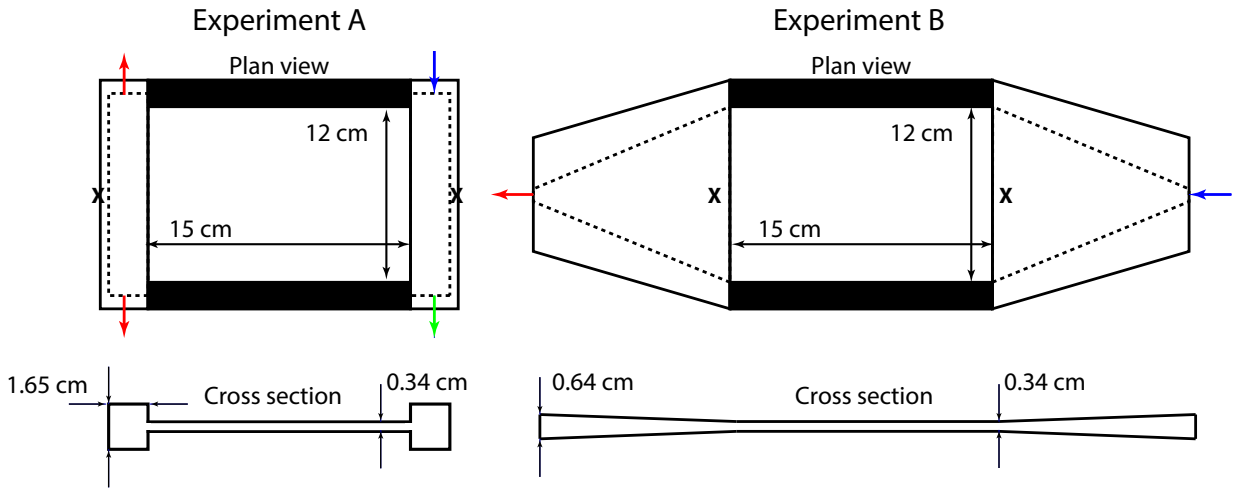

Figure 3.2: Schematic of inlet and outlet manifold configuration for Experiments A (left) and B (right). The separate schematics shown for Experiment A and B highlight the difference between the manifold geometries for the two experiments. For Experiment A, a large rectangular channel (much more conductive than the fracture) bounded each end of the fracture. For Experiment B, the manifold gradually tapered from the inlet/outlet tubing to the fracture geometry. The schematic shows the location of the inlet (blue arrows), outlet (red arrows), and waste (green arrow; experiment A only). The black crosses mark the locations of the pressure ports, which were connected to the differential pressure transducer.

that can be prepared reliably and consistently as a base fluid for high-solid concentration slurries. A laboratory-grade blender (Waring 7012g) mixed the guar/water solution. We slowly added guar with the blender operating at 6,800 rpm. After adding all of the guar we added biocide (Glutaraldehyde, 0.005% by volume) and increased the blender speed to 16,900 rpm and mixed for at least 10 minutes to ensure complete hydration of the guar. Applying a vacuum for at least 12 hours removed most of the trapped air bubbles from the carrier fluid.

We prepared the high-solid-concentration fluid by adding 50% by volume of silica sand to the de-aired carrier fluid. The sand had a multimodal particle-size distribution ranging from submicron to about 600 μm (Figure 3.4). Note, the fines served to reduce the permeability of the solids, which reduced their settling rate such that negligible settling occurred within the fracture. A rotary paddle mixed the slurry as we slowly added sand. After adding all of the sand to the guar solution, we stirred the slurry under vacuum for approximately 15

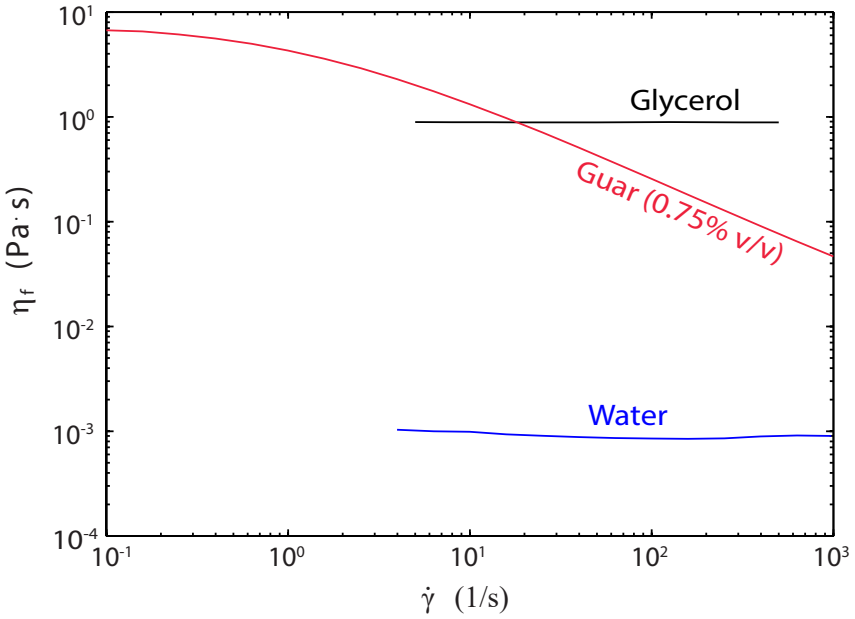

Figure 3.3: Measured viscosities (η_f) plotted against shear rate($\dot{\gamma}$) for water, 100% glycerol, and the 0.75% guar-water mixture used as the carrying fluid for the experiments.

minutes to ensure a well-mixed and bubble-free slurry. Removing bubbles was important both for the flow characteristics (entrained gas increases compressibility of the fluid) and optical quantification of the flow field (Section 3.4).

After mixing, we immediately transferred the slurry to a high-capacity (2.5 L) syringe pump to minimize solid particle settling prior to initiating slurry flow. The syringe pump consisted of a clear polycarbonate pipe (1.7-m long, 2.5-cm inner diameter) fitted with a plunger from a 60-ml syringe. A plastic funnel capped the bottom of the tube and provided a smooth transition from the pipe to the 3-mm-inner-diameter tubing. Water pumped through a tube using a peristaltic pump (Masterflex LS) displaced the plunger and pushed slurry through the funnel at specified flow rates. Balances recorded the mass-flow-rate of water into the syringe ($Q_{in}\rho_w$) and the mass-flow-rate of slurry from the fracture ($Q_{out}\rho_s$).

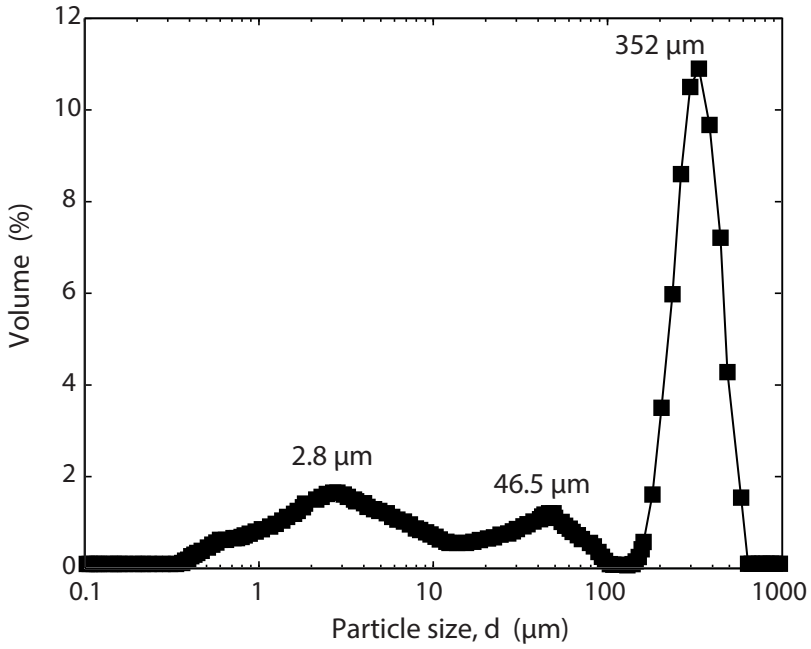

Figure 3.4: Particle-size distribution for the solids used in the flow experiments. The solids consisted of angular silica sand grains.

3.3.3 Experimental procedure

Prior to initiating flow experiments, we used light transmission techniques to measure the fracture aperture field. This involved two steps: (*i*) measuring the mean fracture aperture and (*ii*) measuring the spatial distribution of aperture within the fracture (see Detwiler et al. (1999) for details). To measure the mean aperture, we oriented the fracture vertically with the inlet at the bottom and filled the inlet tubing, manifold, and about 10% of the fracture with dyed water (FD&C Blue No. 1 at 32 mg/L, Warner Jenkins) and acquired a set of images. We then measured the volume of fluid (V_d) required to nearly fill the fracture ($\sim$ 90%) and acquired another set of images. This provided an accurate measure of the mean fracture aperture, $\langle h \rangle = {}^{V_d}/_{A_d}$, where A_d is the area occupied by the injected fluid. We then acquired a set of images with the fracture completely filled with dyed water, flushed the fracture with $\sim$10 pore volumes of deionized water and acquired a set of reference images with the fracture filled with deionized water. We used these images to calculate the spatial distribution of the fracture aperture (described in Section 3.4.1). After measuring

the aperture field, we drained and dried the fracture and associated tubing to prepare for the flow experiment.

After drying the fracture, we filled the inlet tubing with solids-free carrier fluid while carefully preventing entrainment of air bubbles. After filling all of the inlet tubing, we slowly filled the fracture with carrier fluid and acquired a set of reference images. We then rotated the fracture to horizontal and initiated slurry injection at 6.0 ml/min. When the fracture was completely filled with slurry and the effluent mass flow rate reached steady state, we began a stepped flow experiment with image acquisition at regular intervals.

3.4 Image analysis

Raw images consist of measured light intensity values which we transformed to light absorbance, $A = \ln(I_r/I_i)$, where I_r is the measured intensity at a pixel in a reference image and I_i is the measured intensity at the same pixel in the measured image. Converting measured intensities to absorbance allows quantitative comparison of images between experiments by eliminating the influence of variations in camera or light-source settings. Additionally, absorbance fields provide greater contrast between flowing particles and the carrier fluid.

3.4.1 Aperture measurement

Light absorbance can also be directly related to fracture aperture by applying the Beer-Lambert law (e.g., Christian et al. (2014)) to measurements of the fracture filled with clear and dyed water:

$$I = I_o e^{-\epsilon C h + \xi} \tag{3.1}$$

Table 3.1: Experimental parameters and geometry for both experiments

Experiment	A	B
Manifold configuration	Square	Wedge
Fracture Size $L \times W$ (cm)	15.2×11.4	15.2×11.4
Flow rate range (ml min^{-1})	0.2-6.0	0.2-6.0
Mean Aperture (cm)	0.34	0.34
Aperture Standard Deviation	< 0.01	< 0.01

where I is the measured intensity at a location, I_o is the incident light intensity, ϵ is the absorption coefficient of the solute, C is the dye concentration, h is the solute-filled gap, and ξ is a constant that accounts for absorbance by the solvent and the glass plates (Detwiler et al., 1999). Though the fracture consists of two pieces of flat glass, small long-wavelength aperture variations are common. These variations can be quantified using light-transmission techniques to measure the fracture aperture e.g., Detwiler et al. (1999). The aperture at any location is then calculated as:

$$h_{i,j} = \frac{A_{i,j}}{\langle A \rangle} \langle h \rangle \tag{3.2}$$

where $\langle A \rangle$ is the absorbance averaged over the entire field. This method of measuring fracture aperture yields measurements of $h_{i,j}$ that are accurate to within approximately $\pm 1\%$ of $\langle h \rangle$, or about 30 μm for the fracture used in these experiments. Table 3.1 summarizes the details of the fracture aperture measurements for Experiments A and B.

3.4.2 Particle Image Velocimetry

We used particle image velocimetry (PIV) analysis to calculate velocity fields from the measured absorbance fields using a modified version of the Matlab-based software, PIVlab (Thielicke and Stamhuis, 2012). A high-pass filter applied to the absorbance fields removed long-wavelength features and increased contrast between individual sand grains and the

surrounding carrier fluid. We divided the fracture image into 40×40-pixel subregions and calculated the cross-correlation between corresponding subregions in pairs of sequential images. The PIV algorithm provided a local measure of the average distance sand grains moved from one frame to the next. We note that absorbance fields provide a high-resolution measure of the depth-integrated absorbance of the slurry-filled fracture. Thus, the resulting velocity fields indicate an average measure of the velocity of the solids at each location in the fracture. For ϕ_o=0.5 (our experiments) we expected formation of a high-concentration plug in the center of the fracture. Therefore, the measured velocity fields are probably more heavily weighted by particles traveling at the peak velocity and, thus, represent an overestimate of the average slurry velocity. We performed PIV analysis on the entire dataset (1000s of images) and constructed the time-series of the evolving velocity field within the cell.

3.5 Experimental results

After initializing slurry flow through the fracture, we carried out the two flow experiments by sequentially decreasing the flow rate through a sequence of steps and then increasing it through a subset of the same flow rates. At each flow rate, we attempted to allow the pressure differential (ΔP_f) and effluent mass-flow-rate ($Q_{out}\rho_s$) to reach steady state. Figure 3.5 shows the time series of mass flow rate of water pumped into the large injection syringe, $Q_{in}\rho_w$ (red), the differential pressure measured across the fracture, ΔP_f (blue), and the normalized effluent mass flow rate, ${}^{Q_{out}\rho_s}/_{Q_{in}\rho_w}$ (gray). Because the density of the slurry (ρ_s) was ∼1.8 kg/L, we expected the gray line in Figure 3.5 to be relatively constant at a value of 1.8. This was the case for Experiment A, but for Experiment B, each change in flow rate resulted in an immediate increase in ${}^{Q_{out}\rho_s}/_{Q_{in}\rho_w}$ during decreasing flow-rate steps (or, vice versa, decrease in ${}^{Q_{out}\rho_s}/_{Q_{in}\rho_w}$ during increasing flow-rate steps) followed by a gradual decrease in ${}^{Q_{out}\rho_s}/_{Q_{in}\rho_w}$ (or, respectively, an increase in ${}^{Q_{out}\rho_s}/_{Q_{in}\rho_w}$) during the following period of constant flow

rate. This anomalous behavior during Experiment B resulted from expansion/compression of a volume of about 75±5 mL of air that entered the injection syringe during filling. At each flow rate, as the trapped air equilibrated with the new pressure, $^{Q_{out}\rho_s}/_{Q_{in}\rho_w}$ gradually approached the expected steady-state value of 1.8.

Despite the transient flow rates observed during Experiment B, the transients observed in ΔP_f are consistent with the changing flow rate. That is, as the flow rate gradually approached steady state after each change in flow rate, ΔP_f approached steady state at a similar rate. An exception occurred at the lowest flow rates ($t \sim 100 - 150$ min), where ΔP_f became relatively constant even when flow rate changed. For Experiment A, the correlation between Q_{out} and ΔP_f was not as clear, particularly for the increasing flow steps. This was likely due changes in the distribution of solids and fluid within the inlet and outlet manifolds.

To interpret the transient behavior observed during the experiments, it is useful to plot steady-state flow rate (Q_{out}) versus the corresponding ΔP_f at each of the measured flow rates for each experiment to clarify how the slurry rheology affected the transmissivity of the constant-permeability fracture (Figure 3.6). Despite significant differences in the behavior of the time series of the two experiments, plots of Q_{out} versus ΔP_f are surprisingly similar for both experiments. Most notably, results from both experiments suggest a yield stress (or a positive ΔP_f that must be exceeded to initiate flow) as $Q_{out} \to 0$. Also, after flow rate had been reduced to near zero and then increased, the two experiments exhibited significantly different behavior. This observation emphasizes the potential for hysteretic behavior in flows of high-concentration slurries.

In addition to the fracture-scale observations of Q_{out} and ΔP_f, PIV analysis of sequential pairs of images provided discrete measurements of the velocity field within the fracture. Averaging sequential velocity fields, measured during a period when the observed flow rate was approximately constant, provided a relatively noise-free measure of velocity throughout the fracture at each flow rate. Figure 3.7 shows a representative subset of these solid velocity

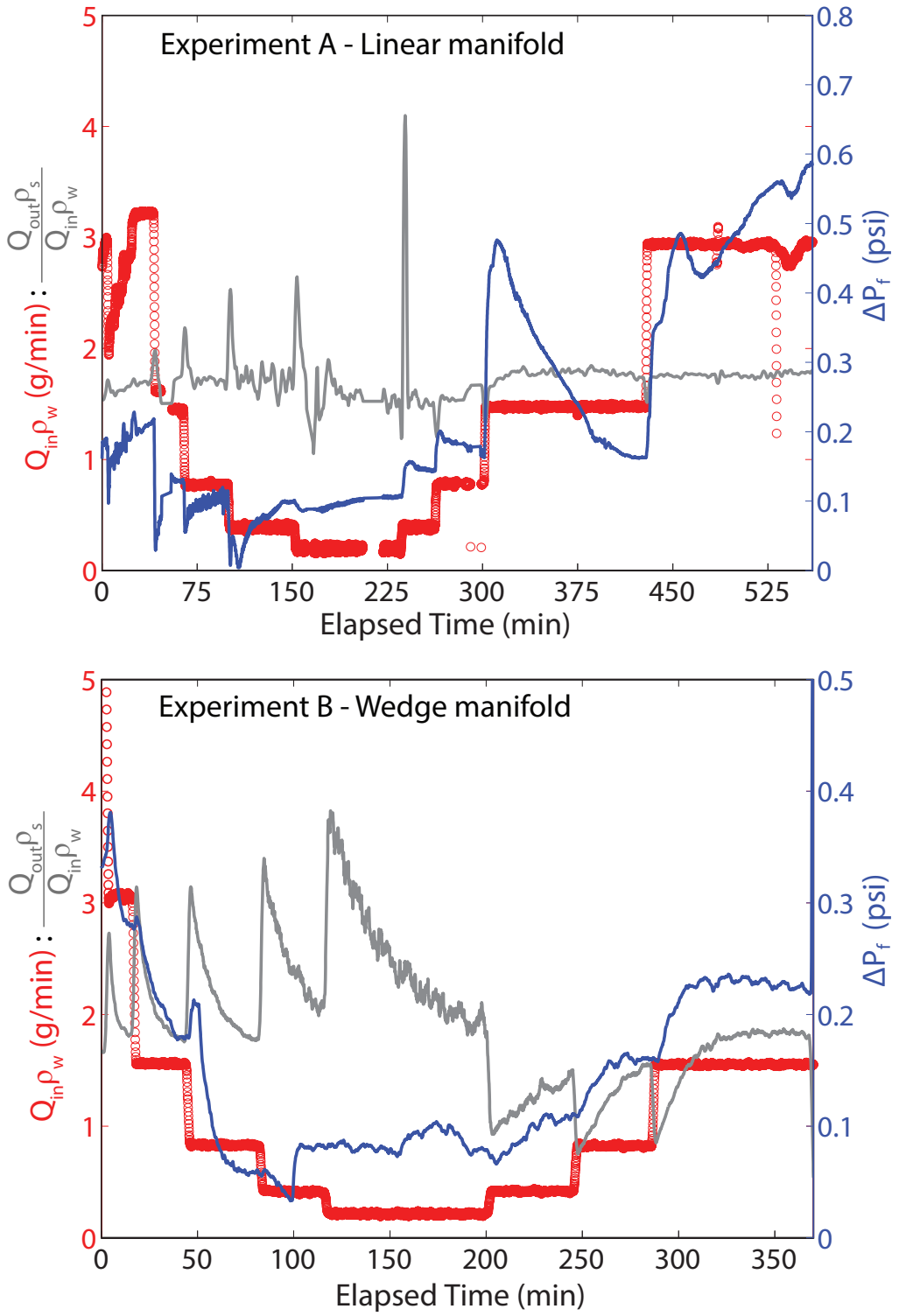

Figure 3.5: Mass flow rate of water into the syringe pump (red) and differential pressure across the fracture (blue) plotted against time for experiments A and B. The gray line is the ratio of the mass flow rate of high-ϕ effluent from the fracture over the mass flow rate of water into the syringe. At steady state, the gray line will be equal to the density of the high-solid-concentration fluid ($\sim$ 1.8 kg/L).

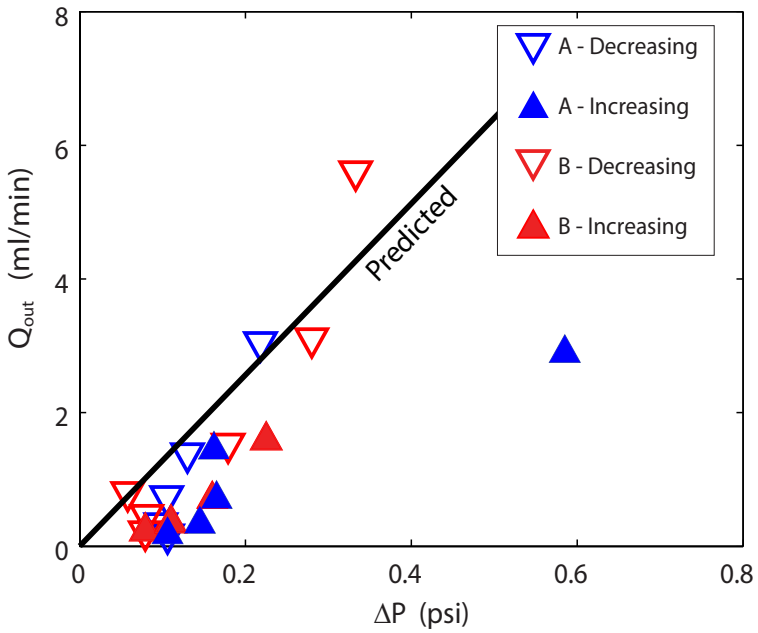

Figure 3.6: Volumetric flow rate through the fracture (Q_{out}) plotted against differential pressure (ΔP_f) for the full range of measured flow rates for both experiments.

fields for both experiments. During Experiment A at early time, the flow field was nearly one-dimensional, with the somewhat surprising result that the highest velocities occurred along the no flow boundaries (top and bottom of each frame in Figure 3.7), where one typically expects fluid velocity to be the lowest due to no-slip conditions on the boundaries. However, at later time, the flow field became more complex with a large region near the outflow boundary with zero velocity and a smaller region near the inlet boundary with near-zero velocity. When the flow rate returned to 1.5 ml/min (last frame at bottom), the inlet region returned to a similar configuration to the earlier measurement at the same flow rate (second frame from top) but the outlet region remained jammed. This hysteretic response was a direct manifestation of the geometry of the boundaries and helps explain the difference in pressure response to decreasing (down triangles) and increasing (upright triangles) flow rates observed in Figure 3.6. The outlet manifold was much larger than the fracture aperture, such that pressure losses within the manifold were relatively small compared to those in the fracture. However, the flow geometry caused a stagnation point at the middle of the manifold, which led to the development of the zero velocity region when

shear rate decreased. The resulting jamming of the solids was not immediately reversible when flow rate was subsequently increased.

By contrast, the inlet and outlet boundaries for Experiment B precluded a stagnation point within the flow system. The resulting flow field remained nearly one dimensional throughout the duration of the experiment. Furthermore, because no jamming occurred, there was no evidence of hysteresis in the relationship between flow rate and differential pressure. However, as with Experiment A, the highest velocities occurred along the no-flow boundaries, which was, again, not expected.

Figure 3.8 shows a representative subset of average velocity profiles ($\overline{V}_x = \frac{1}{L}\int_0^L V_x dx$, where V_x is the component of the velocity in the x- or flow-direction) normalized by the mean velocity ($\langle V \rangle = {}^{Q_{out}}/_{W\langle h \rangle}$). These normalized velocity profiles provide a more quantitative measure of the velocity distributions observed during Experiment B. The magnitude of the high-velocity channels along the edges of the fracture increases relative to $\langle V \rangle$ as the flow rate decreases. In addition, at the lowest flow rate, the velocity in the center region of the fracture also increases relative to $\langle V \rangle$. This behavior likely reflects a change in the distribution of solids across the aperture at the lowest flow rate. Because our experimental system does not measure velocity distributions across the fracture aperture, the source of this shift in measured velocities from the expected mean velocity is unclear. However, the process is readily reversible when the flow rate increases and the velocity profile at 1.5 ml/min is almost identical to that measured during the decreasing steps.

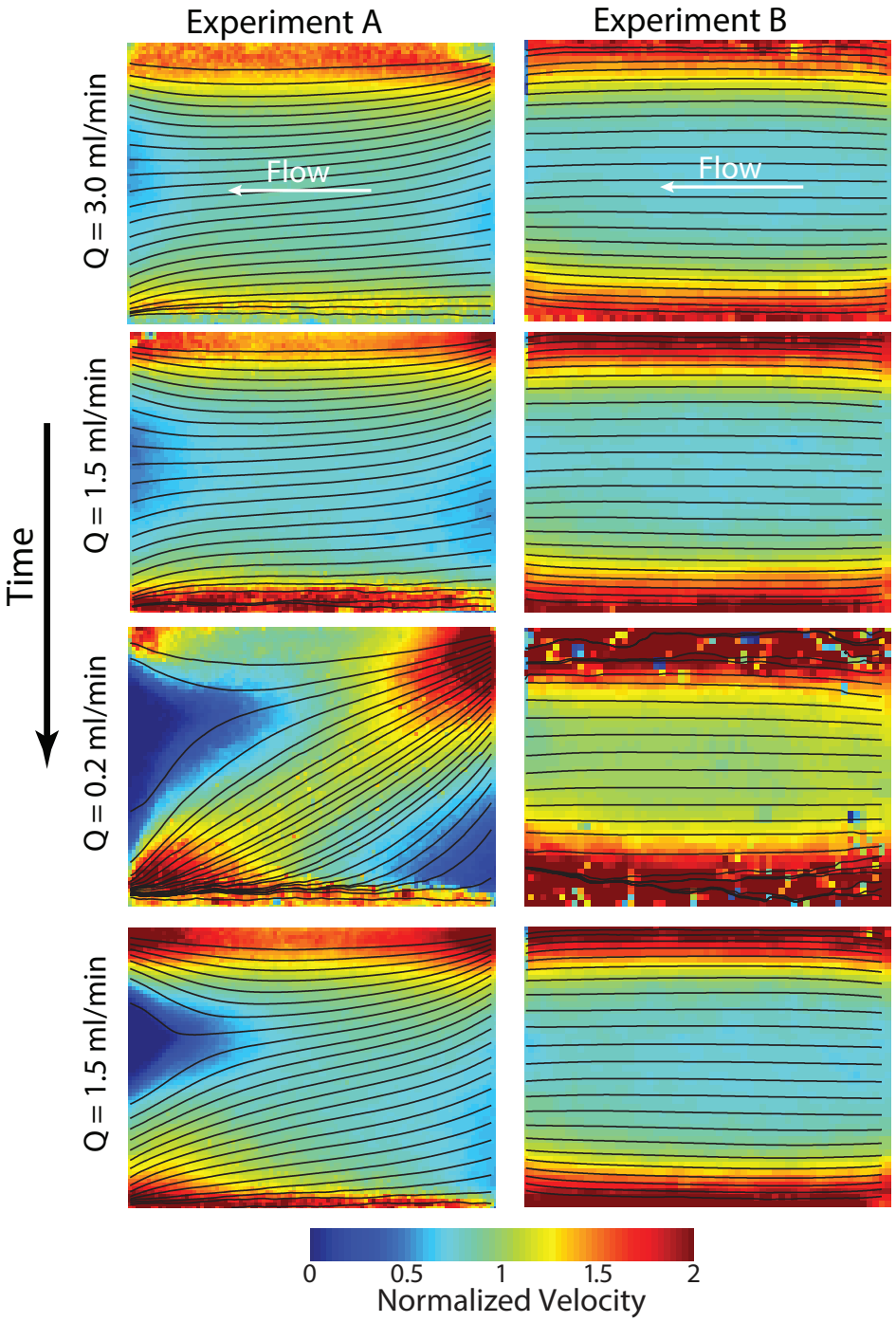

Figure 3.7: Normalized velocity fields measured over the entire fracture for a subset of the flow rates for Experiments A and B superimposed with the corresponding streamlines. The velocity fields are normalized by the depth-averaged velocity ($V = {}^{Q_{out}}/_{W\langle h \rangle}$), during each step to facilitate comparison of velocity fields and profiles at different flow rates. A jammed ($\sim$zero velocity) region developed in Experiment A. High-velocity regions/bands are observed in both experiments near the no-flow (top and bottom) boundaries.

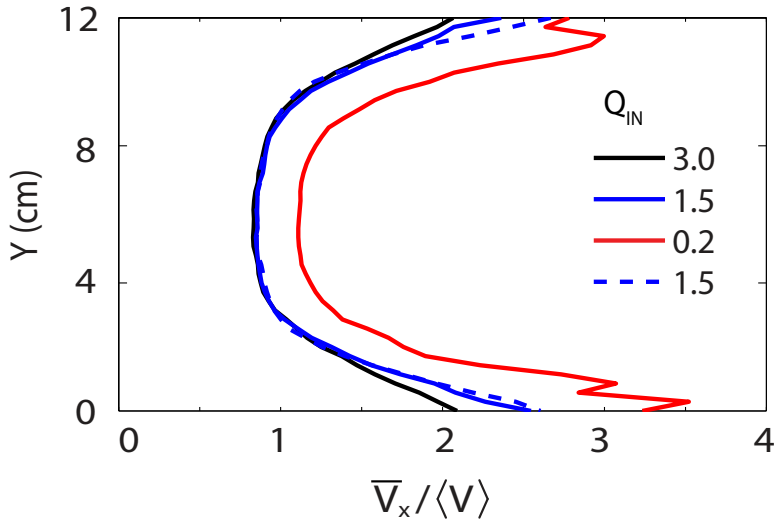

Figure 3.8: Normalized velocity profiles corresponding to the velocity fields shown in Figure 3.7b. These are average profiles (over the fracture length) measured perpendicular to the flow direction. The velocity near the no-flow boundaries is approximately twice the velocity in the middle of the fracture.

3.6 Computational simulations

In this section, we present results from simulations of flow through the fracture to test possible explanations for the strong velocity heterogeneities observed within the uniform-aperture fracture.

3.6.1 Flow of a homogeneous suspension in a Newtonian fluid

We used the rheological model developed by Lecampion and Garagash (2014) to predict the flow of concentrated suspensions. They considered the rheology of mono-disperse solids suspended in a Newtonian carrier fluid. Their model reproduces experimentally observed rheologies over the entire range $0 < \phi < \phi_{cr}$ by combining an effective pressure-dependent yield stress (typical of granular media) with hydrodynamic stresses. Although they present a general model for developing pressure-driven flow, we use their simpler result for fully

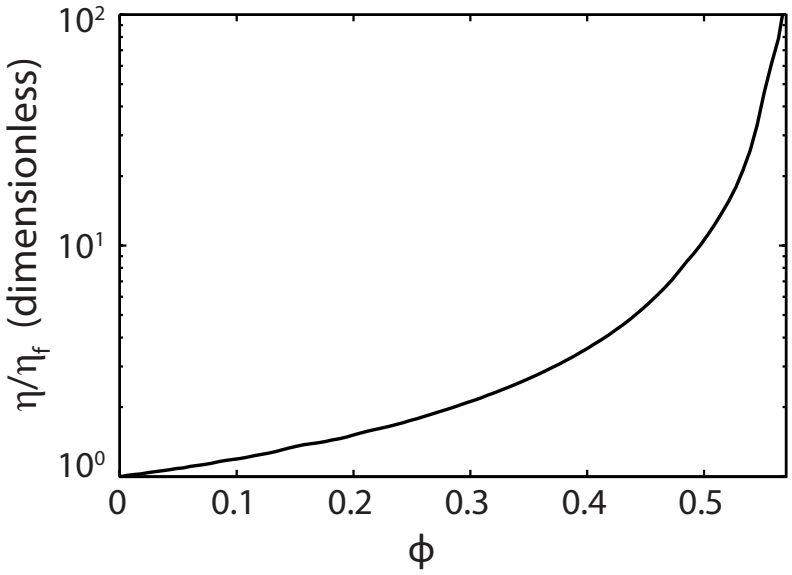

Figure 3.9: The apparent Newtonian viscosity, η, of fully-developed slurry-flow between two plates can be predicted given the Newtonian viscosity, η_f, of the carrier fluid and the solid concentration (ϕ) of the slurry (Lecampion and Garagash, 2014).

developed flow between parallel plates, which allows depth-integration (across the fracture aperture) of the momentum equation. In this limit, they demonstrated that the cubic law (e.g., Witherspoon et al. (1980)):

$$Q = W\frac{h^3}{12\eta}\frac{\Delta P}{L} \tag{3.3}$$

predicts the total flow rate, Q, between horizontal parallel plates, where η is the apparent viscosity of the slurry, h is the aperture, W is the width, L is the length of the fracture and ΔP is the total pressure differential measured across the length of the fracture. The total pressure, $P = P_f + P_s$, includes contributions from the pressure acting on the fluid and solid, respectively, but for the relatively free-flowing conditions considered in our experiments, we expect P_s to be small such that $P \approx P_f$. Figure 3.9 plots the unique relationship between η/η_f and ϕ developed by Lecampion and Garagash (2014) and used in our simulations. Note this relationship assumes a Newtonian carrier fluid.

The measurements of carrier-fluid rheology in Figure 3.3 demonstrate that our carrier fluid was non-Newtonian, except at the lowest shear rates. In order to determine the appropriate effective viscosity to use in our model, we must determine a shear rate that is representative of the experimental conditions. The characteristic shear rate, $\langle\dot{\gamma}\rangle$, of the fluid between the plates will scale with:

$$\langle\dot{\gamma}\rangle \simeq \frac{\langle V\rangle}{h} \simeq \frac{Q}{Wh^2} \tag{3.4}$$

For our experiments, W $\simeq$10 cm, $h \simeq 0.3$ cm, and the flow rate varied from 0.2 to 3.0 ml/min. The highest of these flow rates corresponds to $\langle\dot{\gamma}\rangle \simeq 0.05\ s^{-1}$. Consequently, for our experiments, at all flow rates, $\langle\dot{\gamma}\rangle$ was below the lowest measured shear rate in Figure 3.3 and we can assume the guar-based carrier fluid was within its Newtonian regime with $\eta_f \simeq 8$ Pa·s.

A homogenous slurry, with $\phi = 0.5$, flowing between two plates with Newtonian carrier-fluid $\eta_f \simeq 8$ Pa·s results in a slurry with $\eta_f \simeq 84.3$ Pa·s (Figure 3.9). Figure 3.6 compares experimental observations with the model predictions of ΔP_f for the measured range of Q_{out}. The predictions are in excellent agreement with the experimental results for decreasing flow rate (down triangles) for both experiments A and B. However, the experimental results show evidence of a yield stress (i.e., a non-zero pressure differential when the flow rate approaches zero), which is not predicted by the model.

While we are able to obtain good agreement for the relationship between Q_{out} and ΔP_f, the experimental results indicate significant variations in the velocity field within the fracture. In the following sections, we present an approach for capturing the details of a heterogeneous flow field that explains the experimentally observed flow structure.

3.6.2 Flow of a heterogeneous suspension

In this section, we describe our approach for simulating the flow of variable solid concentration fluid within a fracture, which uses a Lagrangian particle-based approach for tracking the solid concentration within the fracture. We approximate the potentially three-dimensional geometry of the fracture with a two-dimensional array of locations where the local fracture aperture, $h(x, y)$ is known:

$$h_{ij} = h[x = (i + \frac{1}{2})\Delta x, y = (j + \frac{1}{2})\Delta y] \tag{3.5}$$

where $Deltax$ is the size of the Cartesian cells and x and y are coordinates lying in the mid-plane of the fracture (Figure 3.10). Within each cell, we relate pressure gradient and slurry flow rate by assuming locally fully developed flow between the plates, which avoids the need to discretize between the fracture surfaces. This reduction from three-dimensional aperture space to a two-dimensional approximation significantly simplifies solution of the resulting system of equations.

There are many options for tracking the interface between multiple phases (see Kothe and Rider (1995) for a review) including high order advection (Alves et al., 2003), interface reconstruction (Youngs, 1984), level sets (Sussman et al., 1994), and particle-based methods (Monaghan, 2012; Morris and Monaghan, 1997). We use Lagrangian particles that naturally track fluid-history-dependent variables (ϕ, time since injection, etc.) in a frame of reference tied to the fluid itself, which minimizes advection errors (Monaghan, 2012). This method also makes it possible to track the evolution of variations in ϕ due to carrier fluid loss into the matrix. Our approach resembles Particle-In-Cell (PIC) methods used for fluid dynamics simulations (Harlow, 1964) where Lagrangian marker particles representing parcels of fluid are placed throughout the computational domain. The particles carry information such as

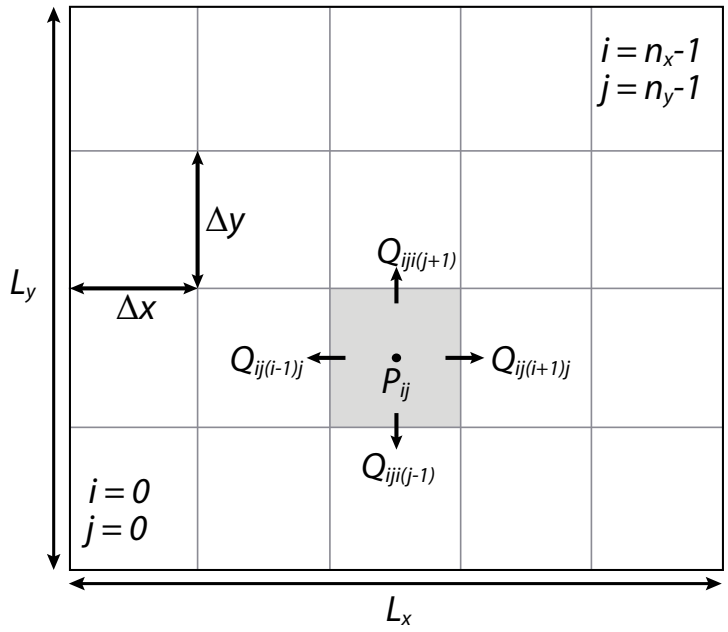

Figure 3.10: The regular cell structure employed by the width-averaged flow solver. The domain Ω_{ij} of cell i, j is highlighted in gray. The pressure, P_{ij} is cell-centered, while fluxes into neighboring elements are face-centered.

η_f and ϕ for a given fluid parcel. At injector locations, source terms are introduced into the flow equations and Lagrangian marker particles are injected with the appropriate volume fractions of the components being injected at that time. Within each timestep of length Δt, the Lagrangian particles contribute to the volume fractions of the various components within the Cartesian cell in which they are located. For example, ϕ_{ij}, the solid concentration in cell i, j can be estimated using a volume-weighted average across the particles present within the cell:

$$\phi_{ij} = \frac{\sum_{\alpha \in \Omega_{ij}} U_\alpha \phi_\alpha}{\sum_{\alpha \in \Omega_{ij}} U_\alpha} \tag{3.6}$$

where Ω_{ij} is the region occupied by cell i, j (highlighted in gray in Figure 3.10):

$$i\Delta x < x < (i+1)\Delta x$$
$$j\Delta y < y < (j+1)\Delta y, \tag{3.7}$$

and U_α is the volume of the parcel of fluid tracked by particle α and ϕ_α is the solid concentration of the parcel of fluid tracked by particle α. Equation 3.6 provides solid concentrations, ϕ_{ij}, at all points on the grid for each time step. Combining these values of ϕ_{ij} with the relationship plotted in Figure 3.9 provides calculations of the effective slurry viscosity, η_{ij} within each cell.

Using Eq. 3.3, we relate the flow rate Q_{ijkl} from cell i, j into cell k, l to the geometry and differential pressure between the two cells:

$$Q_{ijkl} = \Delta x \frac{h_{ijkl}^3}{12\eta_{ijkl}} \frac{P_{ij} - P_{kl}}{\Delta x} = -\frac{h_{ijkl}^3}{12\eta_{ijkl}}(P_{ij} - P_{kl}) \tag{3.8}$$

where h_{ijkl} and η_{ijkl} are the aperture and effective slurry viscosity averaged between cell i, j and cell k, l. We can now assemble a set of linear equations to be solved for the unknown pressures, P_{ij}, by considering the total flux into each cell from its neighbors (see Figure 3.10):

$$q_{i,j} = \sum_{(k,l)\in \substack{[(i-1,j),(i+1,j),\\(i,j-1),(i,j+1)]}} Q_{ijkl} \qquad \forall\ i, j \tag{3.9}$$

where q_{ij} is the local injection (positive) or withdrawal rate (negative) of fluid from cell i, j. In addition, depending upon the flow geometry considered, there will be a number of cells with prescribed pressure according to applied pressure boundary conditions.

The new flow field can then be used to update the location of all Lagrangian particles within the fracture. For example, if particle α occupies cell i, j its change in position, Δx_α, Δy_α is given by:

$$\Delta x_\alpha = v_{ij}^x \Delta t$$
$$\Delta y_\alpha = v_{ij}^y \Delta t \tag{3.10}$$

where v_{ij}^x, v_{ij}^y are the current velocity components in cell i, j and Δt is the discrete timestep used for integration. At this point, the model updates other history dependent variables such as the solid concentration at each particle due to the rate of local carrier fluid loss to the matrix. Although in our experiments there was no loss of carrier fluid into the matrix, this is not necessarily the case for natural systems, either because the fracture walls are not impermeable or because small fissures may take some fluid.

For simplicity, we have presented the equations for the case where buoyancy effects are neglected (horizontal fracture). This is sufficient for the current study where gravity is acting perpendicular to the plane of the fracture and the timescale for settling of solids is considerably longer than the residence time of the slurry in the fracture. We have also implemented the more general case that accounts for potential slumping of denser fluids. Simulations of heterogeneous flow in a fracture

Both experiments developed non-uniform flow fields, despite the homogenous composition of the injected fluid (Figure 3.7). In the case of Experiment A, clear stagnant zones developed at the lowest flow rates. However, both experiments clearly exhibited high-velocity zones along the edges of the fracture. In the case of Experiment B, these features were present and stable at all injection rates. In this section we investigate what mechanisms might explain

the development and stability of such high-velocity channels within the fracture. Using the numerical model described in the previous section, we consider the following possible sources of velocity-field heterogeneity within the fracture: (1) aperture variability; (2) blockages in the manifold at the inlet and outlet; or (3) heterogeneity of ϕ within the inlet manifold.

Our aperture-field measurements indicate variations within a few percent of the average at most and generally much less. Such small variations in aperture cannot explain doubling of the fluid velocity. Furthermore, the measured variations in aperture do not correlate with the high velocity flow channels, thus ruling out the first hypothesis.

Figure 3.11 shows results from simulations in which we introduced blockages within the upstream and downstream manifolds and assumed a constant-ϕ slurry throughout the fracture. This simulation captures the details of the velocity field resembling the experiment near the inlet and the outlet. However, the dissipative nature of flow between two plates results in the flow becoming essentially uniform (across the fracture width, W) in the middle of the fracture (Figure 3.11c).

Finally, we considered the possibility that variations in upstream solid concentration can lead to stable heterogeneity in the flow field. This hypothesis assumes that changes induced either within the upstream tubing or within the upstream manifold induce systematic changes in the upstream solid concentration pumped into the fracture. While the precise mechanism controlling this segregation has not been identified, we can investigate the implications for flow within the observed portion of the fracture. For this hypothesis to be plausible, the induced changes should be relatively small. Furthermore, because the velocity distribution for Experiment B was independent of distance from the upstream inlet, the imposed changes in upstream solid concentration must propagate downstream through the fracture without undergoing significant change.

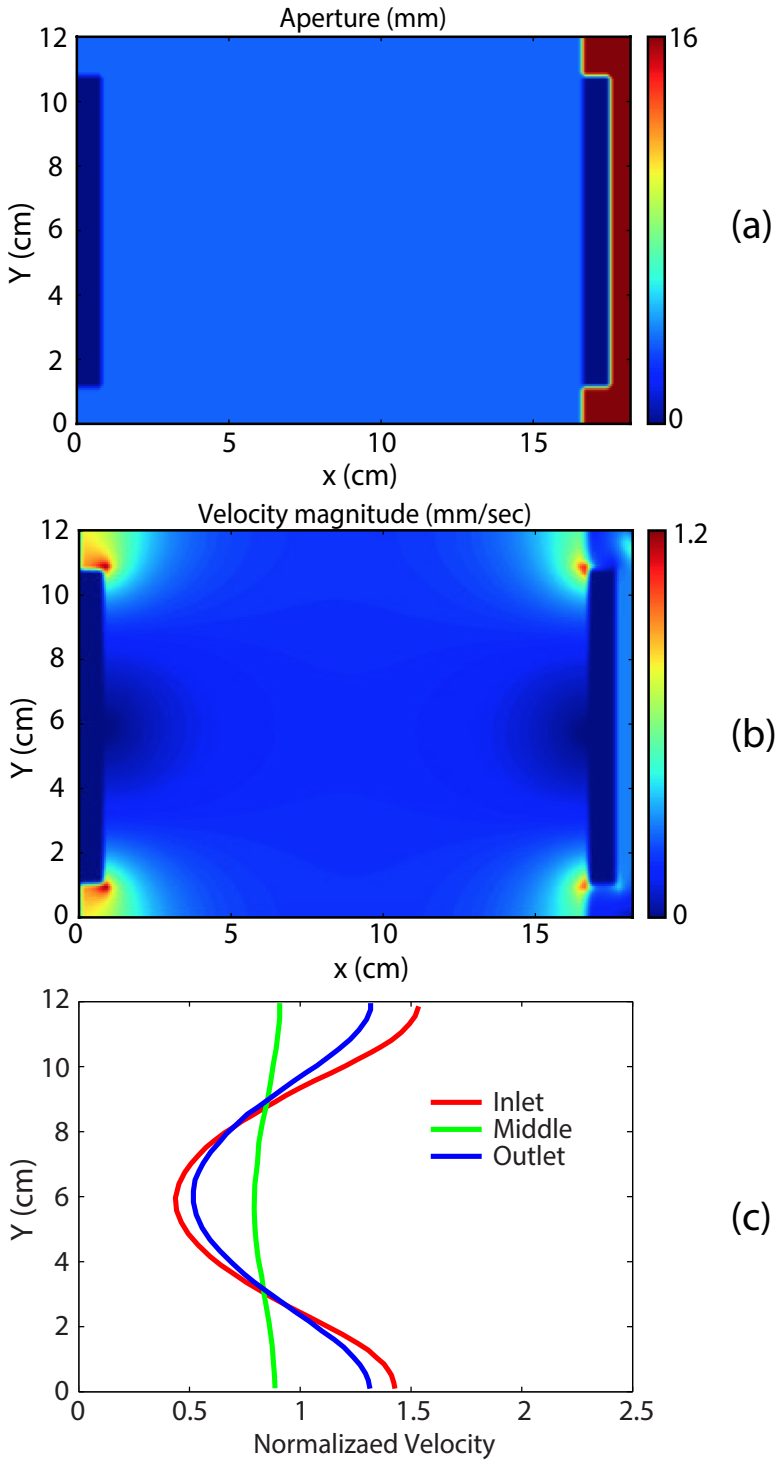

Figure 3.11: Numerical simulation of fully-developed flow of high-solid-volume slurry with an attempt to match the experimentally-observed heterogeneities by introducing blockages within the upstream and downstream manifolds through changes to the aperture field (a) while assuming the fluid remains homogeneous. The velocity field (b) and profiles (c) indicate that the flow midway along the fracture is essentially homogenous due to the dissipative nature of flow within the fracture.

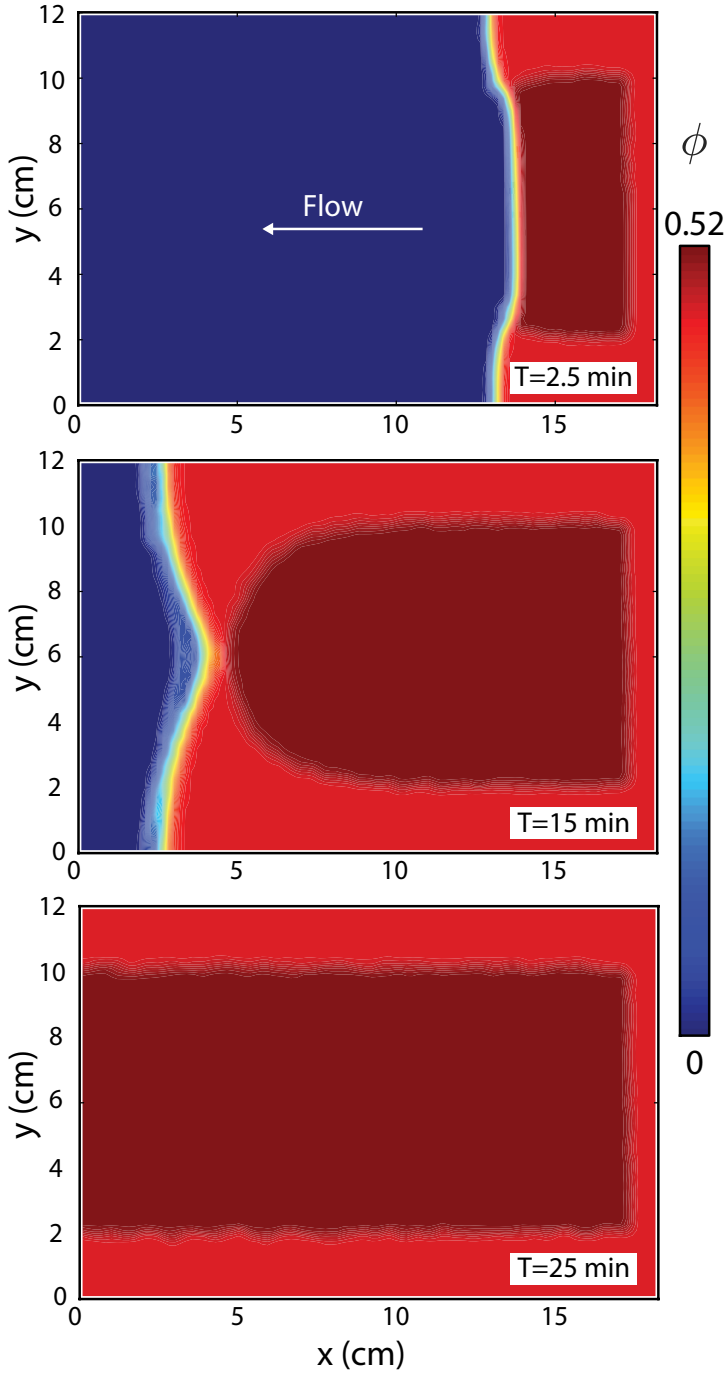

Figure 3.12: Numerical simulation of fully developed flow of high-solid-volume slurry in the fracture with imposed heterogeneity in ϕ at the upstream boundary. The color scale represents the evolving values of ϕ within the fracture . In this example, we impose ϕ=0.47 at the upstream boundary (at right) within high speed channels of approximately 2 cm width. The central region has ϕ=0.515, resulting in $\phi \cong 0.5$ overall. Our numerical model indicates that prescribed upstream variations in ϕ will propagate from inlet to outlet in a stable manner.

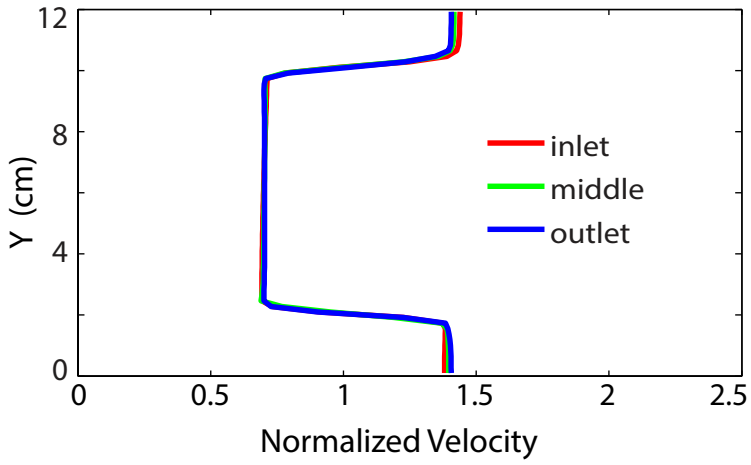

Figure 3.13: Steady-state velocity profiles corresponding to the heterogeneous-solid-concentration model shown in Figure 3.12. For low solid concentration channels having ϕ=0.47 the model predicts slurry velocities are approximately doubled in regions of approximately 2-cm width, in good agreement with experiment (Figure 3.8).

We performed simulations assuming a prescribed distribution of ϕ at the upstream end of the fracture corresponding to approximately 2 cm width channels on either side (Figure 3.12). Our simulations indicate that the imposed changes in the upstream ϕ values are indeed preserved during flow, leading to sustained variations along the entire length of the fracture, including the outlet manifold (see Figure 3.12). In addition, our analysis indicates that a reduction of as little as 3% in ϕ can lead to a factor of two increase in velocity within the low-ϕ channels over that in the higher ϕ central flow region (see Figure 3.13 and Figure 3.14).

Our simulations show that only the third hypothesis is consistent with the experimental observations. In our experiments, heterogeneity in the solid concentration field induced within the upstream tubing and/or inlet manifold likely resulted in variations in ϕ within the fracture. However, in natural and engineered systems, particularly at larger scales, heterogeneities in ϕ are likely to be prevalent. Our results suggest that even small variations in ϕ are both stable and sufficient to induce large (factor of 2) velocity variations in flow channels within the fracture. Figure 3.14 explores the relationship between the velocity of the central region and the fast channels as we introduce progressively greater differences between the values of ϕ in the two regions, while maintaining the same ϕ_o. For the same pressure

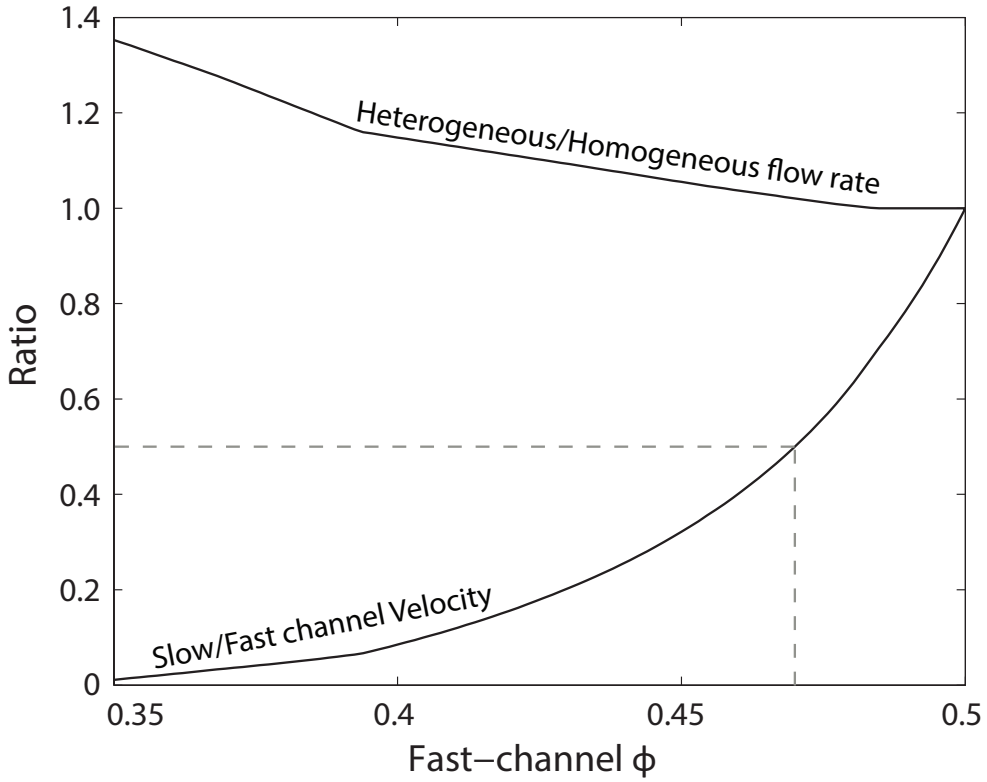

Figure 3.14: This plot explores the influence of increasing solid-concentration contrast in the fracture upon the heterogeneity in the flow field using the same geometry as shown in Figure 3.12. The lower curve shows the predicted ratio of the velocity in the central portion of the fracture to the velocity in the two, 2-cm wide low-ϕ channels. As ϕ approaches 0.34 in the fast channel, the flow in the central region stagnates. A value of ϕ=0.47 approximates the experimental observation of velocity doubling in the fast channel zones (a ratio of 0.5 on this plot). The upper curve shows the ratio of total flow rate in the heterogeneous scenario compared with the flow of a homogeneous solid concentration of 0.5 for the same pressure drop across the fracture. We see that even as the central region stagnates, the total flow rate differs from the homogeneous solution by only tens of percent.

drop across the fracture we also calculated the corresponding total flow rate obtained for these heterogeneous scenarios compared with the total flow rate for a homogeneous slurry with ϕ=0.5 (upper curve in Figure 3.14). Even as the velocity ratio between the slow and fast channels approaches zero, the difference from the total flow rate predicted by the homogeneous theory is only tens of percent. We also investigated the effect of varying the width of fast channels assumed to have a solid concentration of 0.47 (Figure 3.15) upon the flow and confirm that the homogenous theory predicts a total flow rate in close agreement with the heterogeneous flow field. Even when the fast channels are enlarged to 4 cm and $\phi \rightarrow \phi_{cr}$ in the central channel (corresponding to 2/3 of the total area of the fracture) the total flow rate predicted for the homogenous assumption is within ten percent of the heterogeneous result. These two sets of simulations indicate that the reduction in flow within the slower central channel has offset the impact of the fast channels upon the average flow field. As the central region stagnates, nonlinear effects become stronger and the homogeneous solution becomes less accurate. These results suggest that bulk measurements, such as ΔP_f and Q_{out}, provide only weak constraints upon the nature of the flow within the fracture. Specifically, very high velocity channels may develop within the fracture while the total flow rate changes only slightly. However, other transport properties of the heterogeneous system, such as initial breakthrough of slurry and dispersion, will differ greatly from the homogeneous scenario.

3.7 Concluding remarks

We have demonstrated that the experimentally observed relationship between pressure drop and total flow rate through an idealized smooth-walled fracture is predicted well by the cubic law by using a recently-developed rheological model to represent the effective viscosity of the concentrated slurry. However, our experimental results revealed significant variations in the velocity field within the fracture though the cubic law assumes uniform velocity

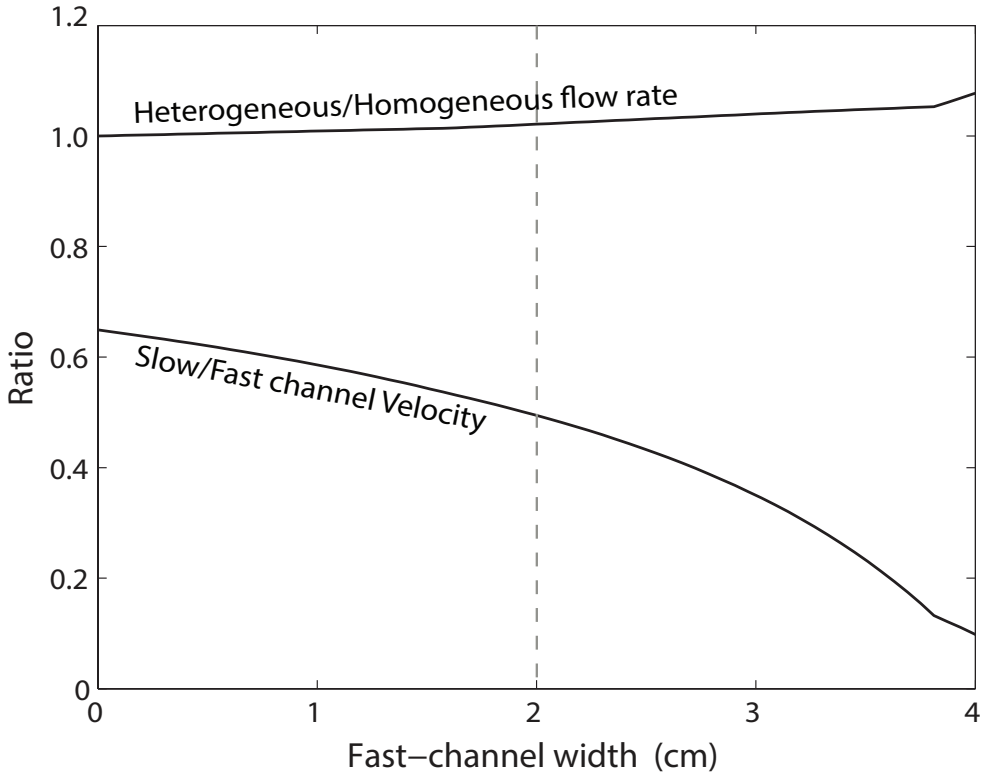

Figure 3.15: We explore the influence of varying the width of fast channels with ϕ=0.47, while maintaining the same average value of ϕ across the entire fracture using the same geometry as shown in Figure 3.12. The upper curve shows the predicted ratio of the flow rate in the slower central portion of the fracture to two channels with ϕ=0.47. As the width of the fast-channels increase, the flow in the central region progressively slows due to increased solid concentration. Also, two channels of width 2 cm approximate the experimental observation of velocity doubling in the fast channel zones (a ratio of 0.5 on this plot). The upper curve shows the ratio of total flow rate in the heterogeneous scenario compared with the flow of a homogeneous solid concentration of 0.5 for the same pressure drop across the fracture. Even as the central region stagnates, the total flow rate is well approximated by the homogeneous solution

in the fracture plane. Further analyses demonstrated that small variations ($\sim$3%) in the spatial distribution of ϕ was sufficient to induce large (factor of 2) velocity variations in channels within the fracture. As $\phi \rightarrow \phi_{cr}$, very small changes in ϕ can result in large differences in the effective viscosity of the slurry and induce both high-velocity channels and immobile or jammed regions. Furthermore, once established, ϕ heterogeneity and the resulting velocity variations, persisted through the length of the fracture; and, once formed, jammed regions persist, even after increasing the shear rate. Finally, while the actual flow within the fracture/fault may be highly heterogeneous, the average pressure drop and total flow rate through the system will remain close to that predicted for homogeneous flow. Consequently, while the assumption of uniform flow may match observations of pressure drop and total flow rates, it may greatly underestimate both the time of breakthrough and degree of dispersion of the slurry transported within the fracture.

In our experiments, the variations in ϕ that caused velocity-field heterogeneity were induced by upstream boundary conditions, despite efforts to maintain a uniform boundary condition of $\phi = \phi_o$. In the subsurface, heterogeneity is ubiquitous and the potential for uniform-ϕ flows to persist in natural or engineered systems seems unlikely. For example, in real fractures, the rock matrix bounding the fracture may have a non-negligible permeability and the resulting loss of fluid to the matrix can cause non-uniform changes in ϕ. Additionally, aperture variability caused by fracture-surface roughness leads to velocity-field variability, even in the absence of solids. In the presence of high concentrations of suspended solids, we expect plug-flow behavior similar to that observed in our experiments when the amplitude of the surface roughness is significantly smaller than the fracture aperture. In fractures with regions with apertures that are on the order of the largest particle diameters, the likelihood of jamming will increase, resulting in relationships between flow and pressure gradient that are more difficult to predict than in our experiments.

Chapter 4

Effect of flow geometry on the evolution of concentrated suspensions flowing through a fracture

4.1 Abstract

Flow of rigid-particle suspensions is prevalent in nature and is important for a range of engineering applications across many disciplines. However, understanding of the three-dimensional flow behavior of suspensions remains limited and studies primarily focus on suspensions consisting of idealized fluids (Newtonian) and particles (neutrally buoyant spheres). Here, we explore the effects of flow geometry on the behavior of a concentrated suspension ($\phi = 0.5$) composed of dense, polydisperse particles suspended in a shear-thinning fluid. Fully developed flow in a tube transitioned through a tapered manifold to a high-aspect-ratio rectangular duct (fracture), which allowed direct visualization of the flow and quantification of the velocity and solid concentration fields. Obstructions added to the fracture

led to increasingly three-dimensional flow fields and allowed direct observation of the role of in-plane shear and extension and contraction of the suspension. We observed centimeter-scale reduced-ϕ regions adjacent to the lateral no-flow boundaries and only millimeter-scale reduced-ϕ regions along no-flow boundaries caused by the obstructions placed in the middle of the flow field. This resulted in regions of increased velocity near the lateral no-flow boundaries, but negligible perturbations to the velocity away from the millimeter-scale shear zone along the internal no-flow boundaries. Additionally, recorded ∇P within the fracture exhibited a transient response that persisted throughout the experiment and was independent of the flow rate or obstruction configuration. Simulations using a suspension balance model provided additional insights into the source of the low-ϕ regions and the mechanisms controlling the transient ∇P. The simulation results support the hypothesis that the non-uniform ϕ-distribution developed in the inlet tubing expanded laterally as the suspension flowed through the manifold, creating the low-ϕ (high velocity) regions next to the no-flow boundaries. Additional simulations showed that particle rearrangement across the fracture aperture was directly related to the transient ∇P observed in our experiments.

4.2 Introduction

Suspensions of non-colloidal, rigid or semi-rigid particles are ubiquitous in a wide range of natural and engineered processes. Examples in natural systems range from the flow of red blood cells suspended in plasma (Bayliss, 1965) to rock crystals suspended in molten lava (Mader et al., 2013). Engineered applications include hydraulic fracturing for oil and gas recovery (Pearson, 1994), soil remediation (Wong and Alfaro, 2001; Murdoch, 1995), removal of drill cuttings (Graham and Jones, 1994; Perez et al., 2004), and the transport of commercial slurries in mining operations (Kaushal et al., 2005). Many of these suspensions

involve fluids and particles with non-ideal properties such as non-Newtonian base fluids and particles that may be angular, denser than the fluid, and polydisperse.

Despite the complexities of many suspensions of interest, studies of idealized suspensions (neutrally buoyant, monodisperse spheres suspended in Newtonian fluids) have led to significant insights about suspension rheology. For dilute suspensions (solid volume fraction, $\phi \lesssim 0.2$), hydrodynamic effects induced by the suspended particles cause the viscosity of the suspension, η, to increase relative to the viscosity of the suspending fluid, η_f. This ϕ-dependence is well represented by a first-order linear approximation for suspension viscosity, $\eta = \eta_f \left(1 + \frac{5}{2}\phi\right)$ (Einstein, 1906). As ϕ increases, the distance between particles decreases and particle-particle interactions influence η. Different models include the ϕ-dependence of η as ϕ increases beyond the dilute range (Krieger and Dougherty, 1959; Frankel and Acrivos, 1970; Chong et al., 1971). One commonly used model is the Quemada model, $\eta = \eta_f \left(1 - \frac{\phi}{\phi_m}\right)^{-2}$, which accurately predicts observations of $\eta(\phi)$ for suspensions with particle concentration in the range $0.15 \lesssim \phi < \phi_m$, where ϕ_m is the maximum solid volume fraction, e.g., the concentration at which the suspended solids jam, or cease to flow with the suspending fluid. As the suspension concentration approaches the jamming limit, $\phi \to \phi_m$, viscosity increases sharply.

In addition to exhibiting strong ϕ dependence, the viscosity of suspensions often exhibits dependence on shear rate, $\dot{\gamma}$. Rheology measurements of neutrally buoyant spheres suspended in Newtonian fluids have demonstrated shear-thinning behavior that is most evident in suspensions with $\phi \gtrsim 0.4$ (Leighton and Acrivos, 1987a; Zarraga et al., 2000). Gadala-Maria and Acrivos (1980) observed a transient response of an ideal suspension subjected to a simple shear in the gap between two concentric cylinders and hypothesized that shear gradients caused particles to migrate out of the gap, reducing both ϕ and η. Those results suggested that the $\dot{\gamma}$-dependence of η for suspensions in Newtonian fluids is due to rearrangements in the microstructure of the particles (or local concentration).

These previous studies in ideal suspensions also inform our understanding of non-ideal suspensions. When particles are suspended in a non-Newtonian fluid with $\dot{\gamma}$-dependent viscosity, the suspension viscosity generally exhibits similar $\dot{\gamma}$ dependence, but the magnitude of the viscosity for a given shear rate increases with ϕ (Metzner, 1985; Dagois-Bohy et al., 2015; Pal, 2015). Experimental measurements suggest the viscosity increase with ϕ at zero shear rate ($\dot{\gamma} \to 0$) follows the Quemada model, such that $\eta(\phi, \dot{\gamma})\big|_{\dot{\gamma}\to 0} = \eta_f(1 - \frac{\phi}{\phi_m})^{-2}$. Polydisperse suspensions exhibit similar flow characteristics to those of monodisperse suspensions. However, smaller particles may fill the voids between larger particles, and thus increase ϕ_m. Experimental observations suggest the viscosity of bi-disperse suspensions of spherical particles only depends on the relative solid volume fraction (ϕ/ϕ_m) and not the particle size distribution (Chong et al., 1971). Stokesian-dynamics simulations verified these results and extended them to multi-modal distributions (Chang and Powell, 1993).

More detailed measurements of suspension rheology in ideal suspensions under simple shear have revealed shear-induced differences in normal stresses, Σ_{ii} (where $i = 1, 2, 3$ are defined for a simple shear as 1-velocity, 2-velocity gradient, and 3-vorticity directions), which result from hydrodynamic interactions or direct contact between particles (Morris and Boulay, 1999; Siginer, 2015). Of particular interest are the first and second normal stress differences, defined as $N_1 = \Sigma_{11} - \Sigma_{22}$ and $N_2 = \Sigma_{22} - \Sigma_{33}$, respectively. These normal stress differences are typically negative, with $\left|N_2\right| > \left|N_1\right|$ for monodisperse suspensions and both scale with shear stress and ϕ (Morris and Boulay, 1999; Zarraga et al., 2000; Boyer et al., 2011a; Garland et al., 2013). However, recent experiments have measured positive values of N_1, which suggests that further experiments are needed to gain a full understanding of shear-induced normal stress differences in suspensions (Dbouk, 2013; Gamonpilas et al., 2016). These shear-induced normal stress differences also cause particles to migrate relative to the bulk motion of the suspension. Such particle migration has been observed in two-dimensional simple shear flows, such as Couette rheometers (Gadala-Maria and Acrivos, 1980; Leighton

and Acrivos, 1987a) and wide-gap Couette flows (Phillips et al., 1992; Abbott et al., 1991), where the particles migrate from regions of high shear rate to regions of low shear rate.

Modeling suspension flow requires effectively incorporating the dependence of η on both ϕ and $\dot{\gamma}$, and their dependence on shear-induced normal stress differences, resulting in migration of particles within the suspension. Leighton and Acrivos (1987a) proposed that shear-induced particle migrations were akin to a diffusive process controlled by an imbalance of particle interactions, which are affected by shear-rate, viscosity, and concentration gradients. This concept was formalized by Phillips et al. (1992) into what is known as the 'diffusive flux model'. Nott and Brady (1994) proposed an alternative 'suspension balance model' (SBM), which couples mass, momentum, and energy conservation of both the solid and suspension phases to explain these shear-induced particle migrations. In this model, the shear-induced particle migrations arise from the requirement of momentum balance in the presence of shear-induced normal stress differences (Nott and Brady, 1994; Brady and Morris, 1997). The original SBM model only accounted for isotropic normal stresses; Morris and Boulay (1999) proposed the introduction of a 'normal viscosity', modifying the SBM to include anisotropic normal stresses. With these modifications, the SBM accurately predicts shear-induced particle migrations in any two-dimensional flow, including truncated cone-and-plate torsional flow (Chow et al., 1995) and parallel-plate torsional flow (Chapman and Leighton, 1991). Experiments involving pressure-driven suspension flow in two-dimensional geometries (tubes and parallel plates) also demonstrate shear-induced migration of particles from regions of high shear rate to regions of low shear rate (Abbott et al., 1991; Koh et al., 1994; Hampton et al., 1997; Lyon and Leal, 1998b; Lecampion and Garagash, 2014; Oh et al., 2015). The result is particle migration away from the walls towards the center line and a corresponding flattening of the velocity profile in the center of the flow. Such observations have been accurately predicted by SBM simulations in simple two dimensional flows where there is only one shear component (Miller and Morris, 2006; Dbouk, 2013).

Efforts to quantify behavior of concentrated suspensions in three-dimensional flow fields have largely relied upon computational simulations. Reddy and Singh (2014) and Yadav et al. (2015) studied concentrated suspension flows in a bifurcating square channel, by applying the diffusive flux model to this three-dimensional flow problem. Though this model does not correctly account for curvilinear flows, they argued that the extensional region of the flow occurring at the bifurcation of the channel is short relative to the length of the flow domain and thus insignificant. Their results predict that the concentration distribution in the branched channels is flattened as the bifurcation angle increased, which significantly changed the shear stress distribution at the walls. Medina et al. (2015) conducted flow-through experiments of a concentrated suspension through a high-aspect-ratio (width to height, $W/h \approx 34$) rectangular duct to study proppant transport in fractures. Note, these experiments differed significantly from previous studies involving Poiseuille suspension flow, such as Lyon and Leal (1998b), where the aspect ratio was $\mathcal{O}(1)$. They observed the development of high-velocity ($\sim 2\times$ the mean velocity) regions near the fracture edges where one would expect velocity to be the lowest. They hypothesized that these high velocity regions were caused by a reduction in solid volume fraction in these regions, which was caused by the tapered inlet manifold that created a region of extensional flow between the inlet tubing and fracture, however, their experiments were unable to directly measure this region of extensional flow.

Here, we present results from a set of experiments in which we systematically increase the degree of three dimensionality of flow through a high-aspect-ratio fracture. It is reasonable to expect that, locally, the ϕ and velocity distributions will be similar to those observed in tubes and parallel-plate systems where $W/h \approx 1$, but our previous results (Medina et al., 2015) suggest that variations across the fracture width may significantly influence suspension flow. We explore the potential effects of three-dimensional flow geometries on the behavior of concentrated ($\phi = 0.5$), polydisperse, dense particles suspended in a shear-thinning base fluid, similar to suspensions of proppants used during hydraulic fracturing. We added simple obstructions to the flow field to systematically study three-dimensional flows that induce ex-

tensional and compressional flow components and shear-rate gradients in multiple directions. The base case is an obstruction-free parallel-plate fracture with inlet and outlet manifolds that induce extension and compression of the flow, respectively. The second experiment includes a thin-plate obstruction, oriented parallel to the flow direction and placed in the center of the fracture, which adds shear-rate gradients in the fracture plane but only causes minor deviation of the largely two-dimensional velocity field. The third experiment includes two symmetric thin-plate obstructions oriented at an angle to the mean direction of the flow, which create significant velocity gradients in the plane of the fracture. In all cases the four walls (e.g., top/bottom fracture surfaces and no-flow boundaries) create shear-rate gradients in both directions normal to the mean flow direction. We use transmitted light techniques to estimate ϕ within the fracture and particle image velocimetry to measure velocity fields during each experiment. To extend our analysis of the experimental results, we also present suspension-balance-model simulations in two different idealized channel geometries.

4.3 Methods

We explored the flow behavior of concentrated suspensions of dense particles flowing through an analog fracture using an experimental apparatus that allowed quantitative visualization of the entire flow field (Medina et al., 2015). Here, we briefly describe the experimental apparatus, the details of the suspension, the experimental procedure, and image processing techniques.

4.3.1 Experimental apparatus

We used a rotating stand with a high-resolution charged-coupled-device (CCD) camera (Photometrics Quantix KAF-6303e) mounted directly above a monochromatic red (wavelength,

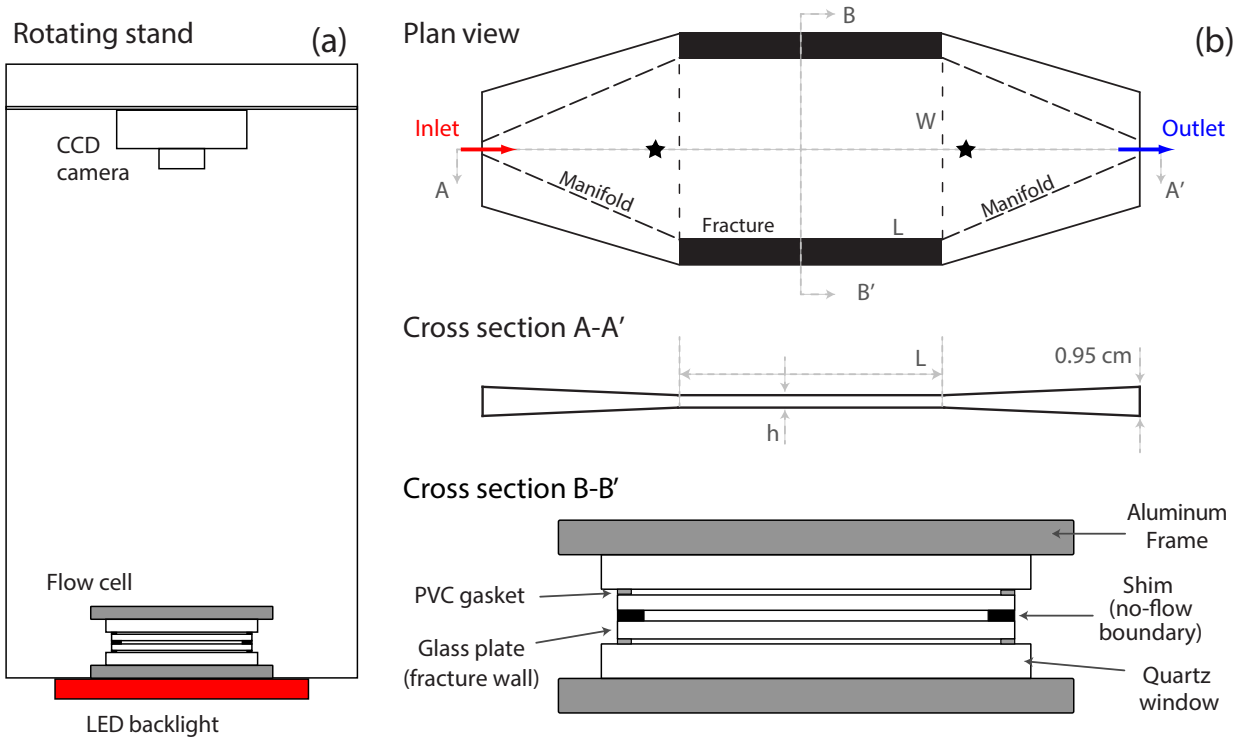

Figure 4.1: (a) Schematic of the rotating stand housing the flow cell, LED panel, CCD camera, and controllers (not shown). (b) Schematic of the flow cell showing the transparent parallel-plate fracture and manifold configuration. The manifold gradually tapers from the inlet/outlet tubing to the fracture geometry. The inlet (red arrow) and outlet (blue arrow) are connected to a 0.95 cm i.d. flexible tube. The pressure ports (black ★'s) were connected to a differential pressure transducer.

$\lambda = 625$ nm) LED panel (Fig. 4.1a). Two fracture surfaces (15.24 cm $\times$ 15.24 cm $\times$ 1.2 cm smooth glass plates) were separated by two aluminum shims (1.91 cm $\times$ 15.24 cm) which acted as no-flow boundaries along the fracture edges and provided a uniform fracture aperture of $\sim$0.3 cm. Two 2.5-cm-thick fused-quartz windows supported by 2.5 cm-thick aluminum frames clamped the fracture surfaces together (Fig. 4.1b). Steel clamps secured the fracture assembly (flow cell) to the stand between the light source and the camera. An electronic controller synchronized 65-ms pulses of the LED panel with exposure of the CCD camera to provide reproducible images of the fracture. The CCD camera used 12-bit digitization of the measured intensities. Linear pixel size of the recorded images was 76 μm.

We carried out a set of three experiments in the same parallel-plate fracture under the same experimental conditions, the only difference was the obstruction configurations (Fig. 4.2). The inlet manifold was connected to a 0.95-cm i.d. flexible tube, and tapered gradually from the inlet port (red arrow) to a slot of the same width (W) and aperture (h) as the fracture; a similar manifold was placed on the outlet side of the fracture (Fig. 4.1b). A differential pressure transducer connected to the ports located at the center of the inlet and outlet manifolds (marked by a ★ in Fig. 4.1b) measured the differential fluid pressure (ΔP) between the inlet and outlet side of the fracture at a sampling interval of 3 seconds. The distance between the pressure ports was 20 cm. The base case was Experiment A, in which the suspensions flowed through a parallel plate fracture without obstructions inside the fracture (Fig. 4.2a). Results from Experiment A were previously reported by Medina et al. (2015). Experiment B, included a 10-cm long aluminum obstruction placed in the middle of the fracture, parallel to the mean direction of flow (Fig. 4.2b). Experiment C included two obstructions in the center of the fracture oriented at an angle of $\pm 27°$, the leading edges of the obstructions were 1.0 cm apart while the trailing edge of the obstruction was 2.0 cm away from the no-flow boundary (Fig. 4.2c). The leading edges of all obstructions were sharp to reduce the potential for developing a stagnation or jamming zone (Fig. 4.2d).

4.3.2 Concentrated suspension details and preparation

The carrier fluid for the suspension was a guar-gum and water mixture, with a 0.75% (w/w) guar-to-water ratio and a density of $\rho_f = 1190$ kg/m^3. We prepared the base fluid by mixing guar and water in a laboratory-grade blender (Waring 7012g). The solution was mixed for at least 10 minutes to ensure complete hydration of the guar. The carrier fluid was then placed under vacuum for approximately 12 hours to remove air bubbles entrapped during mixing. We measured the viscosity of the guar solution at 23°C using a parallel plate rheometer at shear rates in the range $\dot{\gamma} = 0.01 - 1000$ s^{-1}. To assess the stability of the fluid rheology, we

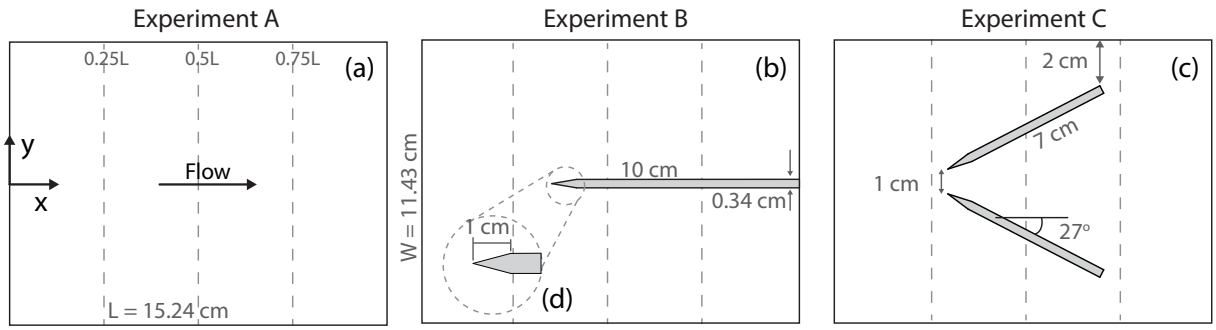

Figure 4.2: Plan view schematic showing the location and orientation of obstructions within the fracture for the three different experiments: (a) Experiment A, with no obstructions, (b) Experiment B, single obstruction aligned parallel to the flow direction, and (c) Experiment C, two obstructions at an angle of 27 degrees from the centerline of the fracture. The insert (d) shows the details of the leading edge of the obstructions. In all experiments flow was from left to right. Vertical dashed lines represent the sampling locations used in Fig. 4.7.

repeated this process 7 times with sample ages ranging from 5 to 269 hours from completion of the initial mixing process. The measurements are represented well by the Cross-power law model, $\eta_f = \frac{\eta_{fo}-\eta_{f\infty}}{1+(m\dot{\gamma})^n} + \eta_{f\infty}$, where m is the fluid relaxation time, n is the power-law index, η_{f_o} and η_{f_∞} are the viscosity at zero and infinite shear rate, respectively (Chhabra, 2006). Least-squares fitting for the 5-hour measurements yielded parameter values of $m = 0.534$ s, $n = 0.833$, $\eta_{f_o} = 6.844$ Pa.s, and $\eta_{f_\infty} = 0.01$ Pa.s (Fig. 4.3). Fitted values of η_{f_o} exhibit an exponential decay with a time constant of ∼200 hours indicating an approximately 5% decrease in the fluid viscosity over the duration of each fracture flow-through experiment.

We prepared the concentrated suspension by adding 50% (v/v) silica sand ($\rho_p = 2600$ kg/m^3) to the de-aired carrier fluid. The sand had a multimodal size distribution with three distinct nominal particle radii of 176 μm, 23 μm, and 1.5 μm (Fig. 4.4). Such multimodal PSD is representative of the solids used in hydraulic fracturing fluids. A rotary mixing paddle mixed the suspension as we slowly added sand to the carrier fluid. A lid with a vacuum-tight pass-through for the mixing paddle sealed the container, and the paddle mixed the concentrated suspension under vacuum for approximately 15 minutes to ensure a well-mixed and de-aired suspension. We minimized solids settling by transferring the suspension into

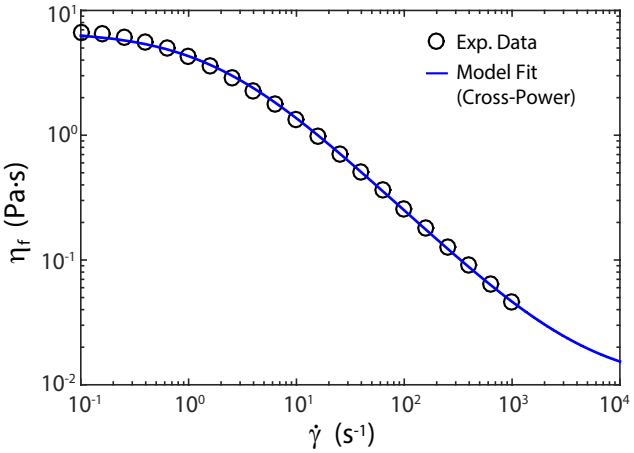

Figure 4.3: Experimental and modeled viscosity of the 0.75% guar-water carrier fluid. The experimental viscosity is approximated by the Cross-power law model: $m = 0.534$ s, $n = 0.833$, $\eta_{f_0} = 6.844$ Pa.s, and $\eta_{f_\infty} = 0.01$ Pa.s

a syringe pump and beginning the flow-through experiment immediately after mixing. The syringe pump consisted of a clear polycarbonate pipe (2.5 m long, 2.5 cm inner diameter) fitted with a plunger. A plastic funnel secured to the bottom of the pipe provided a smooth transition from the 2.5-cm inner-diameter pipe to a 0.95-cm inner-diameter tubing. Water pumped into the opposite end of the polycarbonate pipe displaced the plunger and pushed suspension through the funnel and into the fracture at specified volumetric flow rates.

4.3.3 Procedure for flow through experiments

For each of the flow experiments, we completed the following steps: (1) with the fracture oriented vertically, filled the inlet tubing and fracture with carrier fluid while taking care to avoid introducing air bubbles that could affect flow and induce optical artifacts; (2) acquired reference images of the fracture filled with carrier fluid; (3) connected the tube from the syringe/funnel to the inlet port on the manifold and rotated the stand 90 degrees to orient the fracture horizontally; (4) initiated image and data acquisition and started flow of the concentrated suspension at a flow rate of 6.0 ml min^{-1}; and (5) increased light intensity after the fracture was uniformly filled with the concentrated suspension to enhance contrast

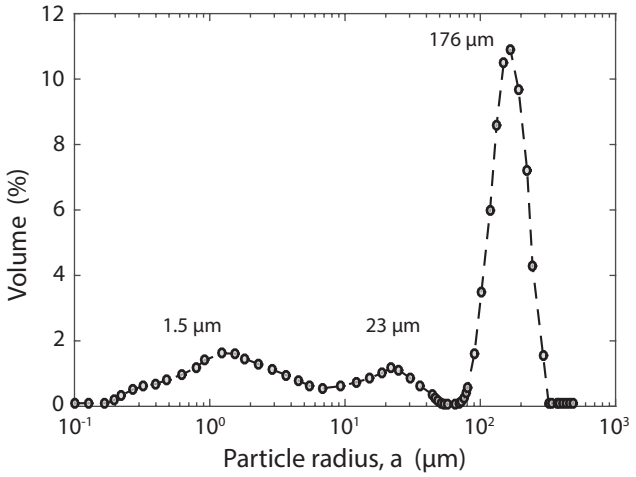

Figure 4.4: Multimodal particle size distribution (PSD) used in concentrated suspension experiments. The particle size distribution has three main modes at $a = 1.5$ µm, $a = 23$ µm, and $a = 176$ µm, respectively.

between solids and surrounding carrier fluid. The flow experiment was then conducted by stepping the flow rate through a sequence of decreasing and increasing target flow rates (Fig. 4.5). Recorded flow rates fall within 3% of the target flow rates. At each step, we changed the flow rate after the flow had reached a quasi-steady state based on the measured ∇P and flow rate, which occurred approximately 50-60 minutes after the initial flow rate change. While carrying out Experiment A, we experienced a data-acquisition malfunction, which resulted in some erroneous pressure readings. The issue was resolved before carrying out any further experiments. The recorded pressure data in Experiment B had small-amplitude periodic oscillations. Filtering these oscillations in post-processing showed qualitatively similar results to those in Experiment C, which involved only a brief data acquisition lapse. During these data-acquisition lapses, only ∇P measurements were affected; the pump, in-flow/out-flow balances, and image systems continued to function properly.

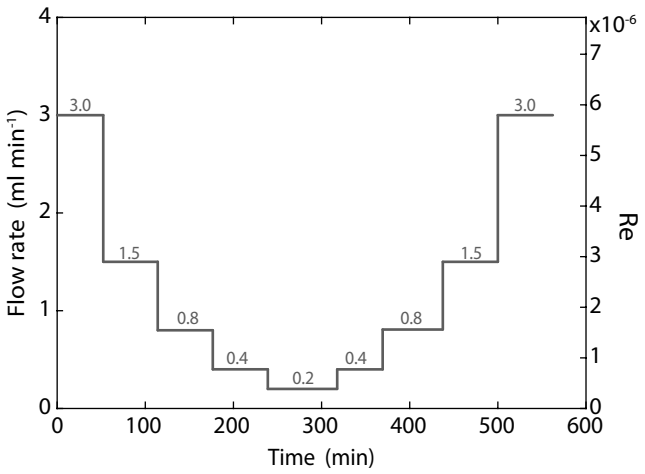

Figure 4.5: Schematic showing the sequence and approximate duration of each flow rate step.

4.3.4 Image analysis

Images captured with the CCD camera measured light-intensity values, which we later converted to light absorbance. Using absorbance allows quantitative comparison of images between experiments by eliminating any spatial variations in light-source intensity. Additionally, absorbance can be used to quantify the aperture and ϕ within the flow field. Post-processing of images corrected small registration errors and temporal variations in emitted light intensity (Detwiler et al., 1999).

4.3.4.1 Aperture measurement

We used light transmission techniques to measure the fracture aperture field. Though the fracture consisted of two smooth glass plates, small long-wavelength variations in the glass are common; using high-resolution images and light transmission techniques allowed us to measure these fracture aperture variations. Light absorbance is related to light intensity by applying the Beer-Lambert law to measurements of the fracture filled with clear and dyed water:

$$A_{i,j} = \ln\left(\frac{I_{c_{i,j}}}{I_{d_{i,j}}}\right) \tag{4.1}$$

where $A_{i,j}$ is the absorbance in pixel (i, j), I_c and I_d are measured light intensity of the fracture filled with clear and dyed water, respectively. We measured the mean fracture aperture by injecting a known volume of fluid, V_f, into a vertically oriented fracture and measured the total area covered by the injected volume, A_f (for a detailed description see Medina et al. (2015, 2016)). We then calculated the mean fracture aperture, $\langle h \rangle = V_f/A_f$, and the spatial distribution of aperture within the fracture (Detwiler et al., 1999):

$$h_{i,j} = \frac{A_{i,j}}{\langle A \rangle}\langle h \rangle \tag{4.2}$$

where h is the fracture aperture, A is the absorbance, and $\langle \cdot \rangle$ represents spatial averaging. The measured average aperture, $\langle h \rangle$, for all the experiments was $\sim$3450 μm. Measurements also revealed a small (long-wavelength) spatial variation of approximately 50 μm, with smallest apertures near the no-flow boundaries.

4.3.4.2 Solid volume fraction measurement

We can derive a relationship to quantify ϕ, based on the measured light absorbance using light absorption and scattering theory (Bohren and Huffman, 2008). Treating the flowing suspension inside the fracture as a 'slab' of particles, we can relate the absorbance to the solid concentration by:

$$A = n_s C_{\text{ext}} h \tag{4.3}$$

where h is the fracture aperture and the absorbance is now defined as $A = \ln\left(\frac{I_{cf}}{I_s}\right)$, where I_{cf} and I_s are the light intensity through the carrier fluid and suspension, respectively.

The particle number density of sand or number of particles per unit volume, n_s, can be approximated by assuming spherical grains, which leads to $n_s = \phi \frac{3}{4\pi a^3}$. C_{ext} is the extinction cross section of the sand particles, which is a measure of total light attenuated by the particles, including attenuation due to scattering and absorption. Using this definition of n_s and rearranging terms, Eq. 4.3 reduces to:

$$A = \phi \frac{3C_{\text{ext}}}{4\pi a^3} h = \phi \alpha_s h \tag{4.4}$$

where α_s is defined as the absorbance coefficient, or the absorbance attenuation per unit length of suspension-filled fracture. If we assume the suspension is well mixed, such that the particle size distribution is well represented across the depth of the flowing suspension, then it is reasonable to expect a single value of α_s for any given ϕ and, thus, absorbance provides a direct measure of ϕ. However, if the suspended particles become segregated by size, this relationship will break down due to the inverse dependence on particle size of α_s.

4.3.4.3 Particle image velocimetry

Particle image velocimetry (PIV) analysis was performed using a modified version of the Matlab-based software, PIVlab (Thielicke and Stamhuis, 2012). A high-pass filter applied to the absorbance fields removed long-wavelength features and increased contrast between sand grains and the surrounding carrier fluid. The fracture image was divided into 32×32 pixel sub-regions. Taking the cross-correlation of each sub-region between two consecutive images yields the average displacement over the time interval between the two images. We performed PIV on the entire dataset (thousands of images) to construct a time-series of the velocity field within the fracture. We note that the PIV analysis provides a depth-averaged measure of the velocity that emphasizes the velocity along the upper fracture surface and does not reveal the velocity profile across the aperture.

4.4 Results

In the following sections, we summarize the results from the three experiments. We first present observations obtained from image processing, including measurements of the evolution of both the velocity fields and particle distribution throughout the duration of each experiment. We conclude with measurements of average pressure gradient over the length of the fracture for the duration of each experiment.

4.4.1 Velocity distribution inside the fracture

PIV analysis provided discrete measurements of the evolving velocity field within the fracture during each experiment. Averaging 30 sequential velocity fields measured at the end of each flow-rate step, provided a relatively noise-free measure of the velocity field. Figure 4.6 shows normalized velocity fields, $V^* = u/\bar{u}$, where $\bar{u} = Q/(W\langle h \rangle)$, for a subset of flow rates of all three experiments. For each experiment, the time evolution of the velocity fields advances from left to right in the figure. A prominent feature in all velocity fields is the red band adjacent to the no-flow boundaries on either edge of the fracture, which indicates measured velocities greater than twice the mean velocity. These high-velocity regions occurred regardless of obstruction geometry and increased in width at lower flow rates. Despite the nonuniform velocities observed near the no-flow boundaries, the velocities measured near the fracture inlet (left-hand edge of each frame) across the middle two thirds of the fracture were relatively uniform.

For the case of the uniform, parallel-plate fracture (Exp. A), the velocity field in the middle region of the fracture (blue region) remained uniform along the entire length of the fracture, but for Exps. B and C, the velocity was affected as the suspension interacted with the obstructions. The no-slip boundaries associated with the obstructions led to narrow regions

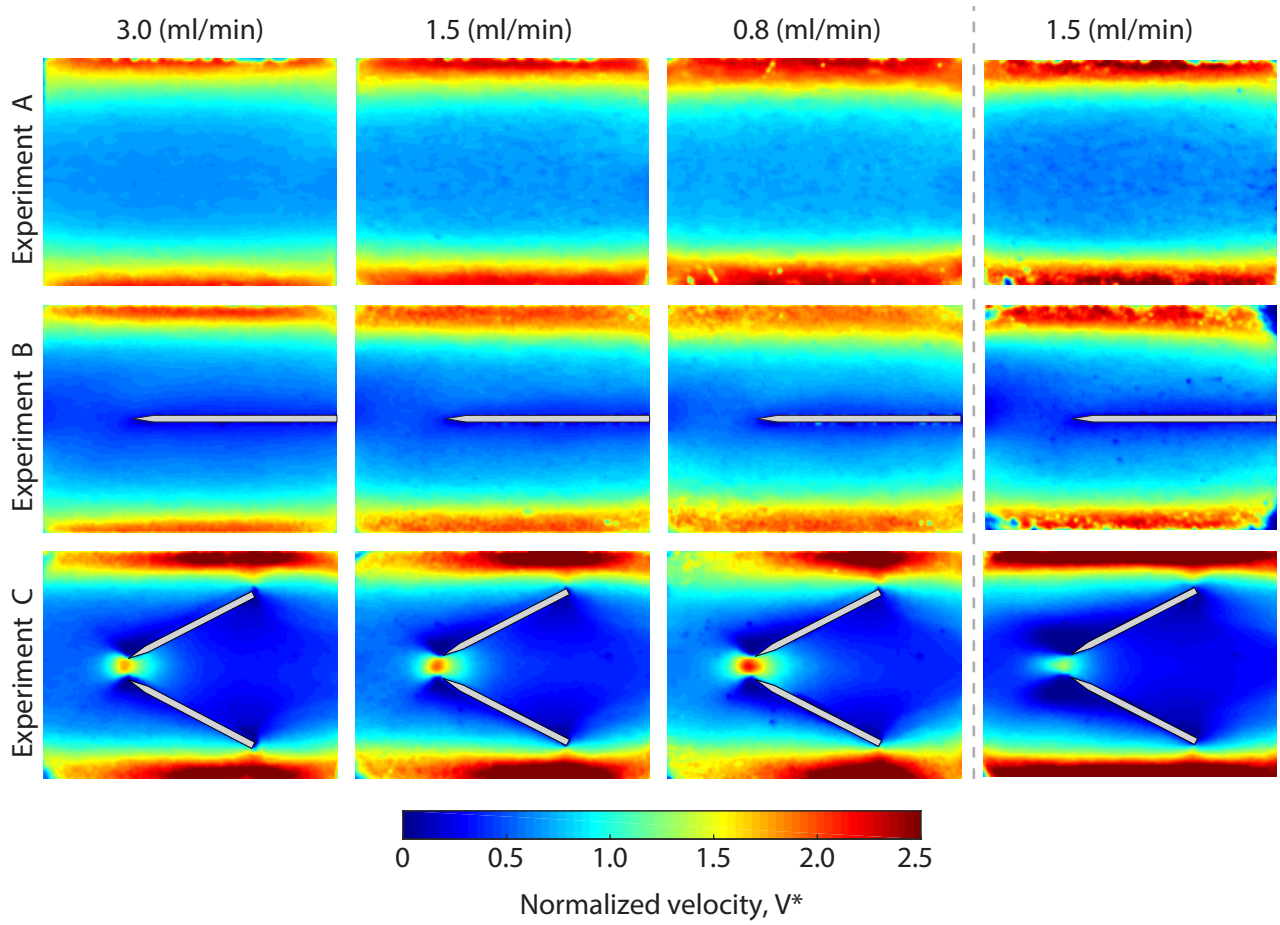

Figure 4.6: Normalized velocity field for a subset of flow rates taken during the step-down and after the flow rate was increased to 1.5 ml min^{-1}, for all experiments. The velocity is normalized by the average velocity, $V^* = u/\bar{u}$, where $\bar{u} = Q/(W\langle h \rangle)$ at each flow rate. A high velocity region near the no-flow boundaries (top and bottom of each frame) is persistent at all flow rates, irrespective of obstruction placement within the fracture.

of low velocity (dark blue) surrounding each obstruction. When the obstruction was aligned parallel to the flow direction (Exp. B), this low-velocity region extended only a few millimeters from the obstruction and the remainder of the velocity field was unaffected by the presence of the obstruction resulting in a velocity field that was similar to that observed in Exp. A. For the experiment with two obstructions oriented at an angle to the flow direction (Exp. C), the obstructions caused a significant alteration of flow paths through the fracture. From the inlet, where the velocity was relatively uniform, the flow converged and accelerated through the gaps between the two obstructions and between the obstructions and the no-flow

boundaries. After exiting the contraction between the two obstructions, the flow diverged to follow the expanding gap between the obstructions and gradually decelerated. The flow around the obstruction led to the formation of stagnation zones (dark blue regions) on the upstream and downstream edges of each obstruction; the stagnation zones on the upstream edges of the obstructions were significantly larger than those on the downstream edges.

As the flow rate decreased, the stagnation zones on the upstream edges of the obstructions increased in size and the localized high-velocity region between the two obstructions increased in magnitude (relative to the mean velocity). However, when the flow rate was sequentially increased after reaching a minimum flow rate of 0.2 ml min^{-1}, the velocity field exhibited hysteresis, which is evident in the difference between the two velocity fields measured at Q=1.5 ml min^{-1}. During the increasing sequence of flow rates, the magnitude of the high-velocity region between the obstructions was significantly lower and the stagnation zones at the upstream edges of the obstructions were significantly larger. Furthermore, we note that though the two obstructions have the same angle as the inlet manifold, high-velocity regions did not form between the obstructions as observed along the boundaries at the entrance to the fracture.

To better quantify the extent of the narrow low-velocity regions surrounding the obstructions, it is useful to plot velocity profiles across the width of the fracture midway ($0.5L$) along the length of the fracture (Fig. 4.7). Note, because the velocity profiles are symmetric about the midline of the fracture ($y = 0$), we plot the profiles from $y = 0$ to $0.5W$. The high-velocity region along the no-flow boundary extends from $\sim 0.35W$ to $0.5W$ for each profile. The magnitude of the normalized velocity exceeds 2 for all cases and is slightly larger for Exp. C due to the acceleration of the flow through the gap between the obstruction and no-flow boundary. For Exps. B and C, the low-velocity boundary layers surrounding the obstructions are evident as the sudden drop in normalized velocity at $0W$ and $0.2W$, respectively. Because the PIV analysis calculated velocity vectors in 32×32-pixel (2.4×2.4-mm) regions, we are

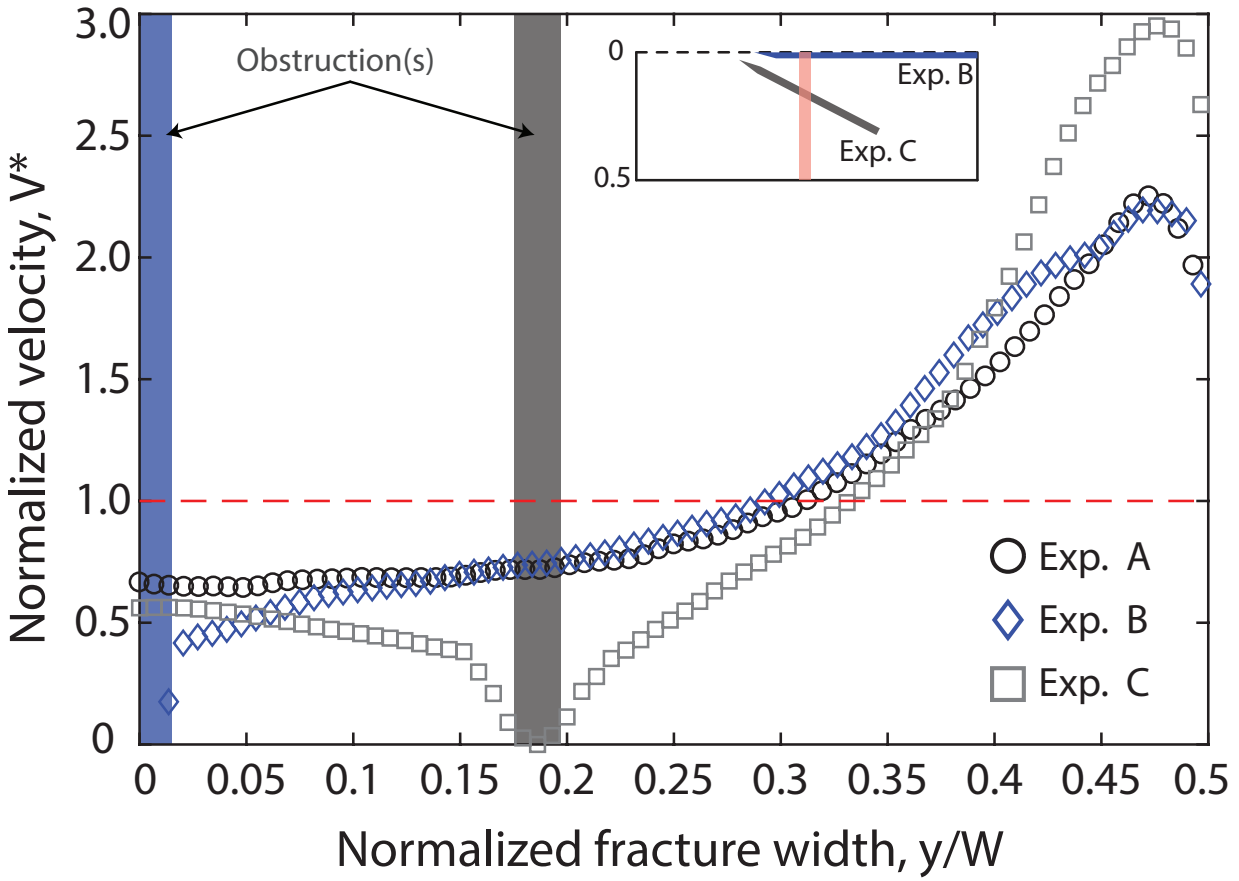

Figure 4.7: Normalized velocity, V^*, profiles taken across the fracture width, sampled at $0.5L$. The sampling location is shown in Fig. 4.2. The different symbols show the profiles for Experiment A (black circles), Experiment B (blue diamonds), and Experiment C (gray squares). The profiles show the velocity increases symmetrically near the no-flow boundaries and span $\sim 0.15 - 0.2$ the fracture width on either side. Vertical blue and gray bands correspond to the locations of the obstructions for Exp. B and C, respectively, as shown in the inset.

unable to precisely resolve the extent of these boundary layers. However, Fig. 4.7 suggests these regions do not extend more than 4.8 mm from the obstruction. These observations are consistent with expectations for Newtonian flow within a high-aspect-ratio rectangular duct, where deviations from simple two-dimensional flow between parallel plates is limited to a region of the order of the gap width. These differences in suspension velocity in the regions adjacent to zero-slip boundaries, e.g., high velocity near the no-flow boundaries and low velocity near the obstructions, cannot explain the source source of the high-velocity region near the no-flow boundaries.

4.4.2 Solid volume fraction (ϕ) distribution

The amount of light absorbed by the suspension is proportional to the solid volume fraction of the flowing suspension. Analyzing the absorbance across the fracture width provides a better understanding on the relationship between the ϕ-distribution and the observed velocity field. Figure 4.8 shows normalized absorbance, A^*, profiles for all experiments, sampled across the fracture half-width. We normalized the absorbance by the mean absorbance of each experiment averaged over the entire fracture area, $A^* = \frac{A}{\langle A \rangle}$.

Figure 4.8 revealed absorbance increased in the regions immediately next to the no-flow boundaries and obstruction walls, i.e., in the shear-zone. For a well-mixed suspension, an increase in absorbance suggests increased ϕ. However, the suspension may not be well-mixed in the regions adjacent to the boundary because shear-induced particle migration in the cross-stream direction (i.e., away from the boundary) is a function of the particle size. This size dependence leads to greater cross flow migration of large particles, similar to that observed in bi-disperse emulsions (Mohammadigoushki and Feng, 2013) and suspensions (Abbott et al., 1991; Krishnan et al., 1996). We hypothesized that preferential migration of large particles away from the high-shear region led to a retrograde migration of fine particles towards the boundary. Because absorbance is inversely proportional to the radius of the particles, $A \propto \frac{1}{a^3}$ (Eq. 5.3), a small increase in the amount of fines can lead to a large increase in absorbance. To test this hypothesis, we carried out another flow through experiment (Experiment B-2) under the same experimental conditions as Experiment B but with the fines removed. Thus, the suspension had the particle size distribution shown in Fig. 4.4 with the fine particles ($a \lesssim 10$ μm) removed and correspondingly a lower bulk concentration of $\phi_b = 0.44$. Figure 4.9 shows a region of the same absorbance profile shown in Fig. 4.8 for Experiment B (blue diamonds) from $y = 0$ to $0.1W$ and the corresponding absorbance profile for Experiment B-2 (red squares). The profiles show that absorbance increased $\sim 12\%$ when the fines were

present and decreased $\sim 10\%$ in the absence of fine particles in a narrow region, $\mathcal{O}(h)$, next to the boundaries.

We investigated the observed deviations of the absorbance near the boundaries by measuring the absorbance of a suspension composed of fine particles *only* and a suspension with a mutlimodal PSD. We found that the absorbance for the suspension of only fine particles was approximately three times higher than the absorbance for the suspension with multimodal PSD. These measurements and the absorbance profiles in Fig. 4.9, support the idea that as larger particles migrate away from the boundary (towards the 'bulk' flow), fine particles migrate in the opposite direction, towards the boundary. A mass balance calculation on a small control volume next to the obstruction, suggests that the concentration of coarse and fine particles must change by $\Delta\phi \approx 0.12$, for the absorbance to increase 12% (Fig. 4.8 and 4.9). The additional influx of large particles into the 'bulk' flow increases the concentration of coarse particles from $\phi_c = 0.440 \rightarrow 0.448$, while the concentration of fine particles decreases from $\phi_f = 0.060 \rightarrow 0.052$.

The normalized absorbance profiles across the fracture width are representative of the the bulk flow, except for the light gray regions discussed above (Fig. 4.8). The profile for Experiment A (black circles) shows that the absorbance was uniform in the middle of the fracture ($y = 0$ to $\sim 0.32W$) and decreased by $\sim 3\%$ near the no-flow boundary. The region of uniform absorbance is consistent with the uniform velocity in the middle of the fracture and the region of decreased absorbance is consistent with the high velocity regions (Fig. 4.7). The normalized absorbance in Experiment B (blue diamonds) was also uniform in the middle of the fracture, it gradually increased and then decreased from A^* =1.015 at $0.35W$ to A^* =0.975 at $0.45W$. Experiment C (gray squares) had a uniform absorbance in the middle of the fracture, between the obstructions from $0W$ to $0.15W$. The absorbance increased on the outside of the obstructions and decreased by $\sim 1\%$ around $0.46W$, near the no-flow boundary. The observed ϕ-distribution across the fracture width is consistent with the velocity profiles

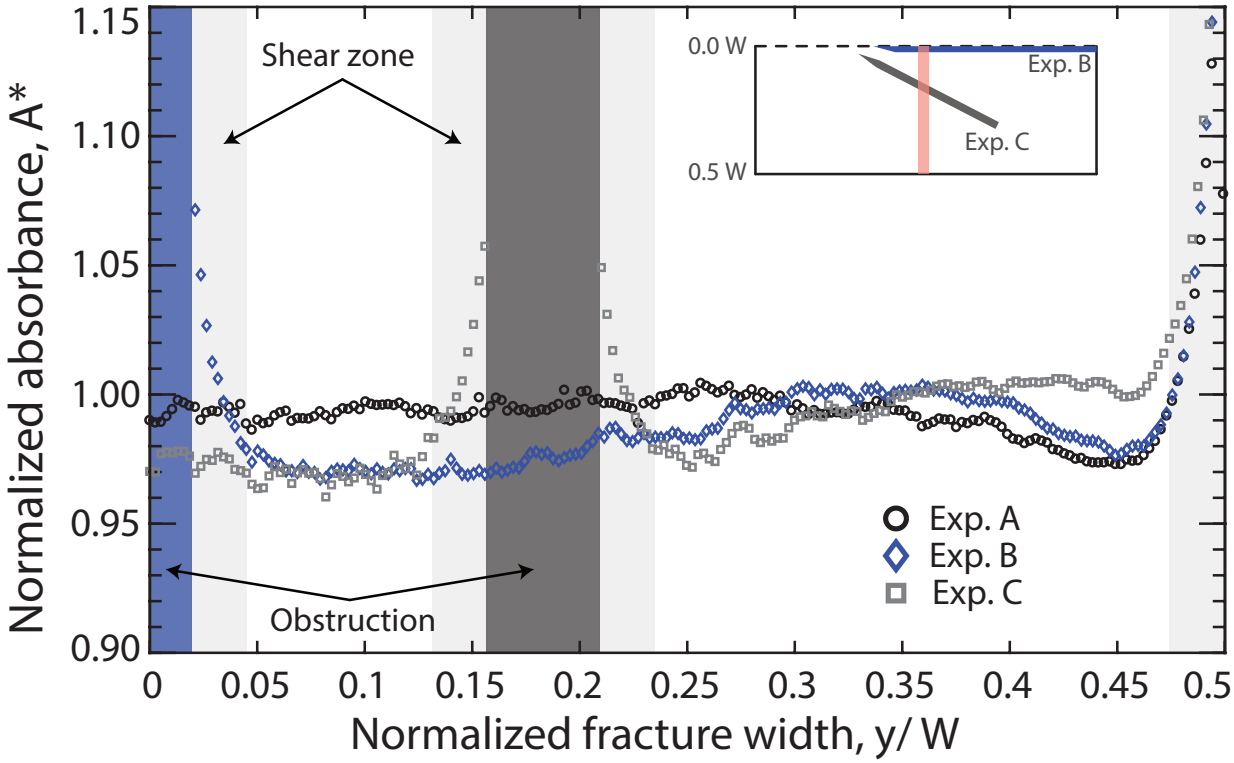

Figure 4.8: Normalized absorbance, A^*, profiles sampled at $0.5L$, averaged over 1.0 cm (along the direction of flow). The absorbance was normalized by the average absorbance of each experiment. Dark blue/gray shaded areas indicate the location of the obstructions. Absorbance for Experiment A (black circles) was uniform in the middle of the fracture and decreased $\sim 3\%$ near the no-flow boundaries at $\sim 0.32W$. Absorbance for Experiment B (blue diamonds) was uniform in the middle, slowly increased and then decreased near the no-flow boundaries at $\sim 0.35W$. Absorbance in Experiment C (gray squares) was also uniform in the middle of the fracture between the obstructions; it increased slowly towards the no-flow boundaries and then decreased slightly at $0.46W$. The absorbance for all experiments in the regions immediately next to boundaries increased sharply; see text for explanation. The measurement uncertainty was $\pm 0.2\%$.

for all experiments and suggests that the regions of high velocity near the no-flow boundaries are correlated with regions of decreased ϕ. Note that the diverging obstructions in Exp. C do not induce regions of low-ϕ and high-velocity near the obstructions. This suggests that the low-ϕ, high-velocity regions at the beginning of the fracture must result from a non-uniform ϕ-distribution at the inlet to the manifold.

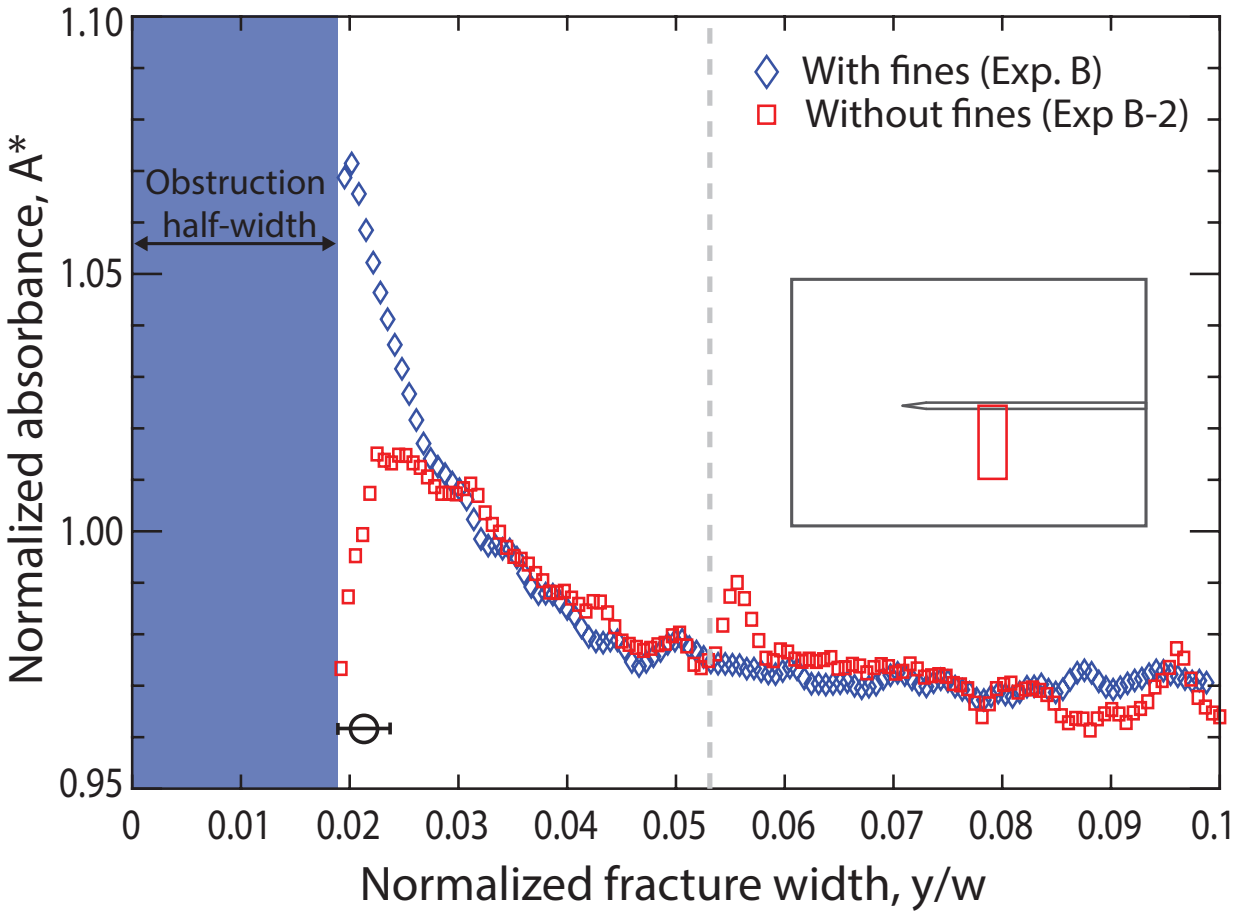

Figure 4.9: Comparison of normalized absorbance profiles for two experiments with different particle size distribution. The suspension in Experiment B (same as previously presented) was composed of multimodal PSD (blue diamonds). The suspension in Experiment B-2 had a bimodal PSD (red squares). Absorbance profiles sampled immediately next to the obstruction show the absorbance of the multimodal suspension increased approximately 12%, while the absorbance of the bimodal suspension decreased approximately 10% in the region immediately next to the obstruction. The black symbol shows the size of the largest particles. The measurement uncertainty was $\pm 0.2\%$.

4.4.3 Pressure gradient across fracture

In addition to the velocity measurements, our system allows the measurement of pressure difference between the inlet and outlet of the fracture, which yields a direct measure of the fracture-scale pressure gradient, ∇P. Figure 4.10 shows the measured in-flow rate, Q_{in} (black line), out-flow rate, Q_{out} (gray line), and ∇P (blue line) over the duration of the experiment. Data for Exps. A and B showed qualitatively similar behavior, however, we present Exp. C, which had the most complete dataset (see Sec. 4.3.3 for more details).

Figure 4.10 shows that after each step-change in Q_{in}, the out-flow rate (Q_{out}) reached the value of Q_{in} after a short delay ($\lesssim 5$ minutes). There was also a large change in ∇P over a short time, consistent with the time it took the out-flow rate to equilibrate with the in-flow rate. After the large change, ∇P slowly rebounded and approached a steady-state over a much longer timescale ($\sim$ 60+ minutes). Figure 4.11a highlights these two timescales in more detail by plotting ∇P (blue triangles) and the root mean squared deviation (RMSD) of the velocity (black circles) after decreasing the flow rate to $Q = 1.5$ ml min^{-1}. The RMSD calculates the deviation of the velocity at any given time from the velocity at the end of the flow step (e.g., steady-state). The velocity reached steady-state within minutes (≤ 5 mins.) after the step change in flow rate, while ∇P changed over the duration of the flow step. Figure 4.11b shows the pressure gradient normalized by the gradient at the end of the flow rate step, ∇P_{ss}, for the decreasing flow rates. The figure shows a similar transient ∇P response for all flow rate steps: initially ∇P drops to about $0.85\nabla P_{ss}$ and then slowly rebounds to reach steady state about 60 minutes after changing the flow rate. The measured pressure gradients suggest that the timescale to reach steady-state is insensitive to the flow rate of the suspension. Furthermore, the results also suggest that the magnitude of the early-time ∇P drop is only slightly sensitive to the flow rate.

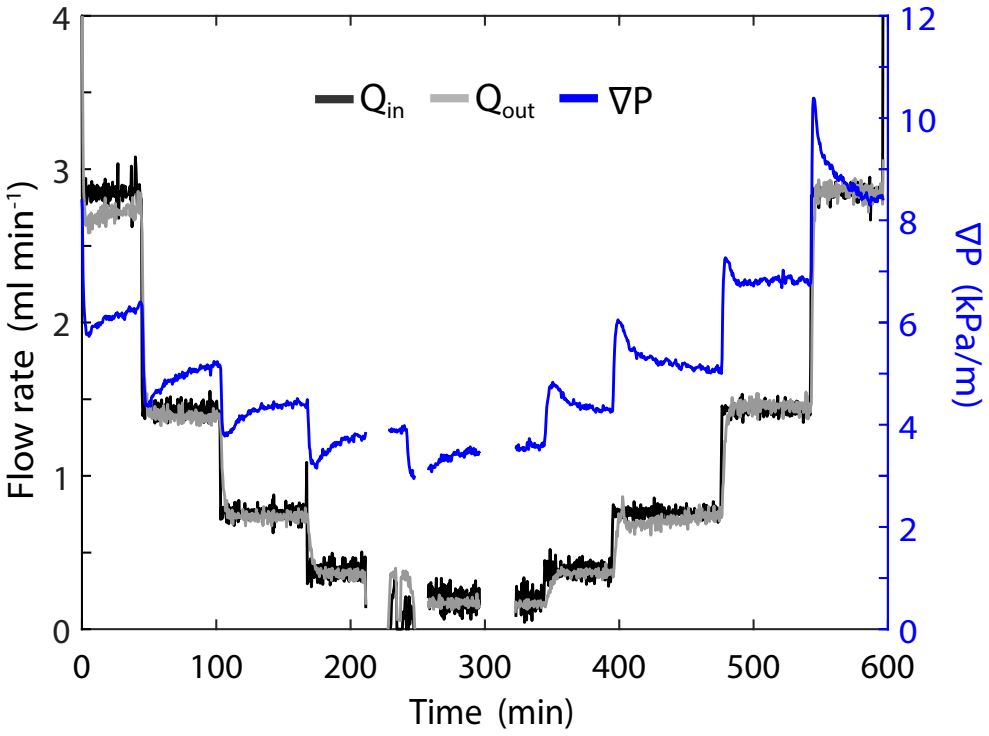

Figure 4.10: Time series showing pressure gradient, ∇P (blue line), in-flow rate, Q_{in} (black line), and out-flow rate, Q_{out} (gray line), for Experiment C. Time zero is the time at which the flow rate decreased from 6.0 ml min^{-1} to 3.0 ml min^{-1}. The pressure response shows a transient behavior after every step change in flow rate which lasts up to several dozen minutes. Gaps in data were due to instrument data acquisition malfunction, however, the flow was unaffected.

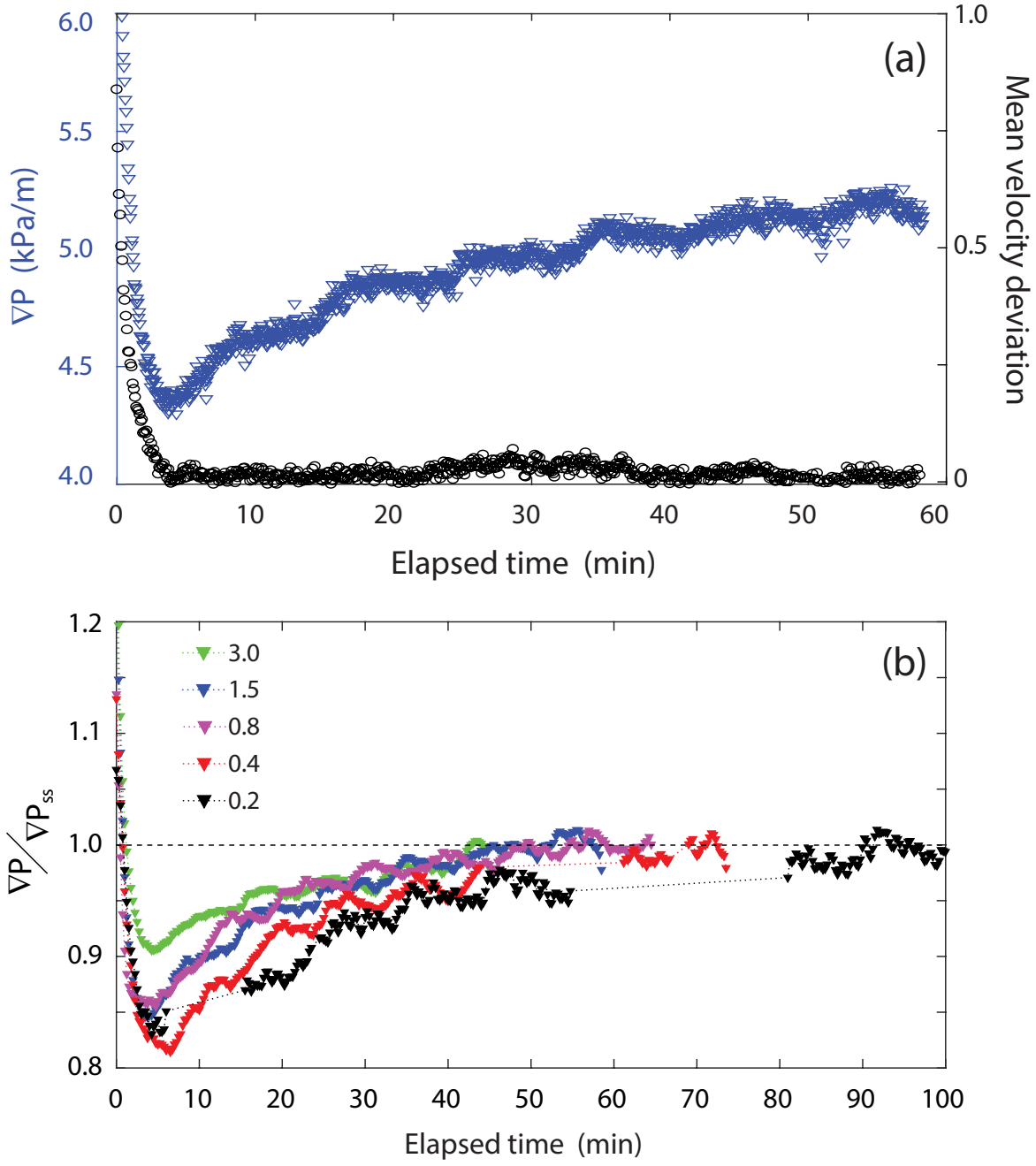

Figure 4.11: (a) Pressure gradient ∇P (Blue triangles) and mean velocity deviation (root mean squared deviation) from the velocity at steady state (Black circles) after the flow rate was decreased to $Q = 1.5$ ml min^{-1}. The velocity deviation shows the velocity field reached a steady state a short time ($\leq$ 5 mins.) after the flow rate was decreased. On the other hand, ∇P exhibits a short-time transient (which coincides with the velocity change) and a long-time pressure transient, which persisted over the duration of the flow rate step. (b) ∇P normalized by the steady state ∇P_{ss} (end of flow rate step) for the decreasing flow rates. The plot shows a similar trend for all flow rates.

Plotting the steady-state ∇P at the end of the flow rate reveals the pressure gradient response to the flow rate. Figure 4.12 shows ∇P normalized by the specific weight of the fluid, $\rho_f g$, plotted against Reynolds number, averaged over the last four minutes at the end of each flow rate step, for Experiment B (blue triangles) and Experiment C (gray triangles). Due to data acquisition issues discussed above, Experiment A was excluded in Fig. 4.12, but it is reasonable to expect the relationship would be similar to that of Experiment B. The arrows indicate the sequence of the experiment. Both experiments had a higher pressure gradient during the increasing portion of the stepped flow test. This hysteretic behavior was most pronounced for Experiment C, and can be explained by comparing the velocity fields for two flow rates during the decreasing and increasing stages, respectively. Column 2 in Fig. 4.6 shows the velocity field for $Q = 1.5$ ml min^{-1} for decreasing flow rate steps, and column 4 shows the velocity for the same flow rate during the increasing flow rate steps. As discussed in Sec. 4.4.1, these two velocity fields show clear differences. The larger jammed region in the vicinity of the stagnation zone leads to an increased pressure gradient during the increasing set of flow rates. Figure 4.12 also suggests that both experiments exhibit a yield stress, i.e., non-zero ∇P as $Q \to 0$ ml min^{-1}.

Our experimental results revealed two different timescales of the transient ∇P response after a step change in flow rate: a short-time (≤ 5 mins.) transient, associated with the change in flow rate, and a long-time transient which persisted over the duration of each flow rate step. This transient ∇P behavior was observed in all experiments, irrespective of flow rate, obstruction placement, solid concentration, or particle size distribution.

4.5 Discussion

The experimental velocity and pressure gradient results showed unexpected behavior of the concentrated suspension. Our measurements showed the regions near the no-flow boundaries

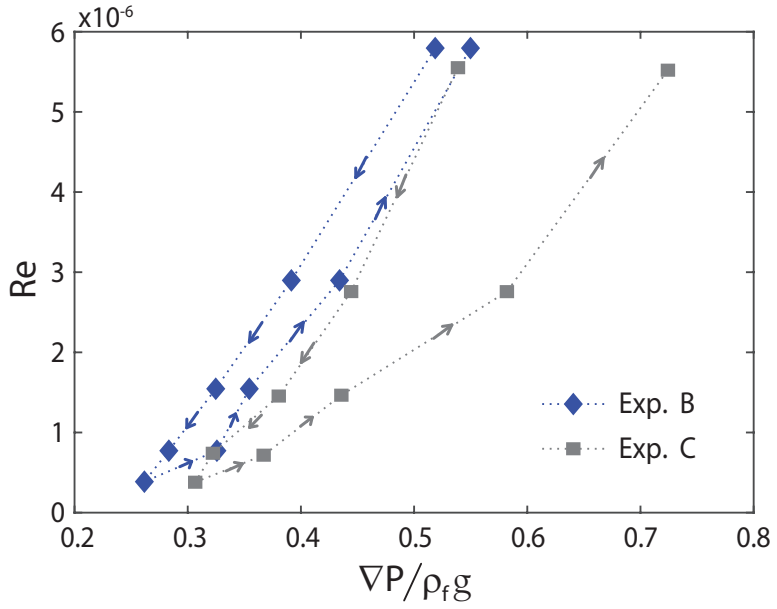

Figure 4.12: Experimental pressure gradient (∇P) normalized by the specific weight of the fluid ($\rho_f g$) versus Reynolds number ($Re = \frac{\rho h \bar{u}}{\eta}$). The data shows a hysteretic behavior, which was most pronounced for Experiment C, the case with two obstructions. Both suspension exhibit a yield stress, i.e., ${}^{\nabla P}/_{\rho_f g} > 0$ as $Re \to 0$.

had velocities that were more than twice the average velocity. The absorbance analysis revealed these high-velocity regions were correlated to reduced ϕ in these regions. Furthermore, the angle of the manifold walls was the same as the angle of the obstructions in Exp. C, however, regions of low-ϕ (high-velocity) did not develop in the extensional region between the obstructions. Therefore, we hypothesize these low-ϕ regions were caused by the formation of non-uniform ϕ-distribution upstream of the inlet manifold. Pressure measurements across the fracture showed two characteristic timescales for ∇P in response to a step-change in flow rate. The long-time transient ∇P was observed in all experiments and was insensitive to flow rate. We hypothesize that the long-time transient ∇P behavior was caused by internal changes in the suspension, i.e., particle rearrangement as the suspension flowed through the fracture. Because we cannot quantify these changes with our experimental system, we use the two-dimensional suspension balance model (SBM) (Dbouk, 2013) in two different idealized flow geometries, to investigate the source of the high-velocity (low-ϕ) regions near the no-flow boundary and the transient ∇P observed in our experiments.

As previously discussed, shear-induced normal stress differences in suspensions cause particles to migrate from regions of high shear to regions of low shear. Guar-gum fluids also have normal stress differences, however, these differences are negligible for shear rates $\dot{\gamma} \leq 10$ sec^{-1} (Torres et al., 2014). The maximum shear rate expected in our experiments was ~ 1.0 sec^{-1}; therefore, we assume normal stress differences arising from the fluid are negligible and are ignored. We modified the SBM model to include the shear-dependent fluid viscosity for 0.75% guar-gum solution, which is approximated by the Cross-power law model (Fig. 4.3). This SBM model assumes uniform-sized particles; we used the weighted geometric mean of the particle radii ($a = 56$ μm) as an approximation of the multimodal PSD used in the experiments.

We used the suspension balance model to simulate a 2-D version of the geometry described in Section 4.3.1. The geometries of Experiments A, B, and C correspond to Models A, B, and C, respectively. For all three models, flow was along the x-axis and the fracture width was aligned with the y-axis, such that shear acted in the x-y plane (e.g., fracture plane). We plot the concentration profiles for all three simulations, normalized by the inlet concentration $\phi_0 = 0.5$ (Fig. 4.13). The profiles show a slight concentration decrease at the obstruction boundaries in Model B and Model C, which are consistent with that observed for Exp. B-2 (Fig. 4.9). Though there are slight differences, ϕ^* profiles for all three simulations show the regions adjacent to the no-flow boundaries have a significantly lower ϕ^* than the middle regions. The normalized concentration profiles show ϕ^* decreased by approximately 4% near the no-flow boundary for all simulations (Fig. 4.13). These low-ϕ regions spanned approximately $0.1W$-$0.12W$ on either side, similar to that observed in the experiments (Fig. 4.8).

As with the experiments, the obstructions did not develop low-ϕ regions similar to those next to the no-flow boundaries. This difference is best illustrated by Model C: the obstructions have the same expansion ratio (i.e., same angle) as the inlet manifold and both are no-slip

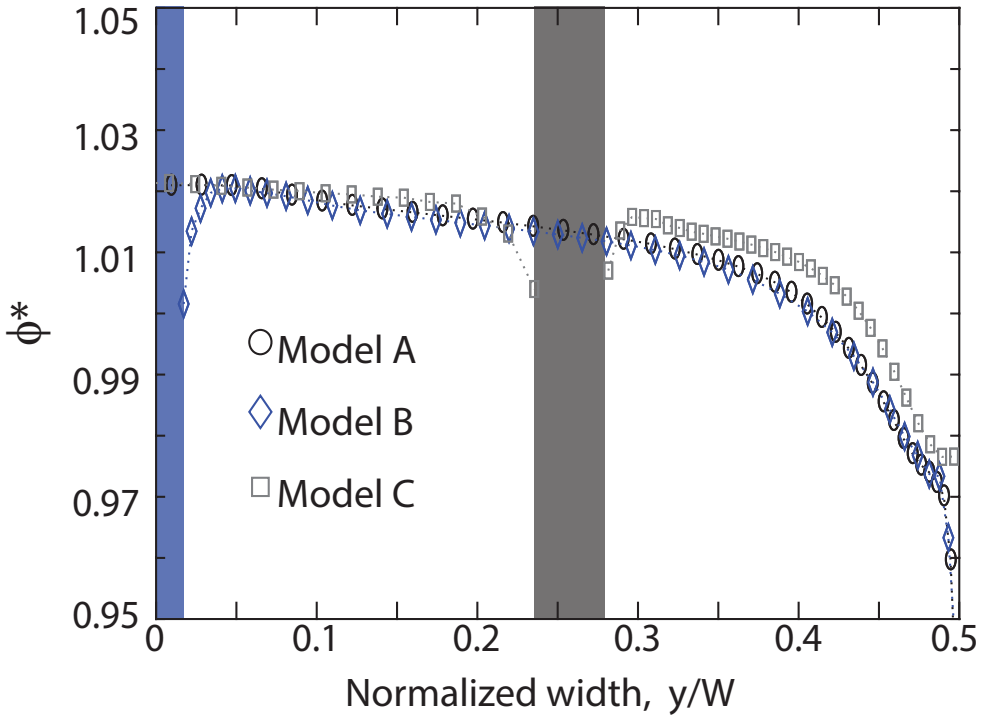

Figure 4.13: Normalized concentration, $\phi^* = \frac{\phi}{\phi_0}$, profiles sampled across the fracture width at $0.5L$ for all three models. The profiles show ϕ^* decreased $\sim 4\%$ at $0.35W$ (Model A), at $0.35W$ (Model B), and $0.40W$ (Model C), respectively.

boundaries. Flow through the manifold and in the region between the obstructions has similar extensional flow components. The reason low-ϕ regions developed adjacent to the no flow boundaries and *not* between the obstructions is due to upstream solid distribution. The simulation included a long tube, upstream of the manifold. As the suspension flowed inside the tube it developed a non-uniform ϕ-distribution which was then extended inside the manifold. Therefore, when the suspension reached the fracture entrance at $L = 0$, the concentration was already non-uniform across the width. In contrast, upstream of the obstructions the suspension was uniform, this was confirmed by both the simulation and experimental results (Sec. 4.4.2). Thus, the low-ϕ regions observed in both the simulations and experiments were not caused by the manifold, they developed inside the tube and were extended laterally as they flowed through the manifold.

We investigate the cause of the long-time transient pressure gradients observed in our experiments by simulating a long, rectangular, 2-D channel oriented in the x-z plane (e.g., aperture plane) with the same height as the fracture aperture, $h = 0.34$ cm. We imposed a parabolic velocity profile, $u_x(z)$, and a uniform solid volume fraction $\phi_0 = 0.5$ at the inlet. We simulated injecting the suspension at a flow rate of $Q = 6.0$ ml min^{-1} until it reached steady-state. The step-decrease in flow rate was simulated as an instantaneous decrease in velocity, corresponding to a flow rate of $Q = 3.0$ ml min^{-1}. We investigate the effect of gravity by simulating the suspension with particles that are denser than the fluid and the suspension with neutrally buoyant particles. For more details on the simulations see Appendix A.

Figure 4.14 shows the evolution of the suspension concentration and the effect this evolution has on the pressure after a step change in flow rate from 6 to 3 ml min^{-1}. Figure 4.14a shows the evolution of the $\phi-$profile across the fracture aperture. We sampled the concentration one meter into the fracture, which results in a travel time from the inlet to the observation point that is similar to the timescale required for suspension in the experiment to travel from the pump to the observation point in the fracture. For the neutrally buoyant suspension there was almost no change from the previously established steady-state ϕ-distribution (Fig. 4.14a2), whereas, for the dense suspension, the ϕ-distribution evolved over time (Fig. 4.14a1). Because the decreased velocity leads to reduced shear rate, shear-induced particle stresses decrease and gravity causes particles to migrate towards the lower fracture surface. This particle migration leads to the formation of a region with higher solid concentration on the bottom surface (Fig. 4.14b1).

Changes in the ϕ-distribution led to corresponding changes in the velocity distribution (Fig. 4.14b3), therefore, it is instructive to consider the evolution of the shear stress, $\tau = \dot{\gamma}\eta(\phi, \dot{\gamma})$, across the aperture. Figure 4.14c shows the shear stress normalized by a characteristic shear stress, $\tau_0 = \dot{\gamma_0}\eta(\phi_0, \dot{\gamma_0})$, where shear rate is approximated by $\dot{\gamma_0} = \frac{3\bar{u}}{h}$ and $\phi_0 = 0.5$ is the

inlet concentration. The shear stress distribution for the suspension with neutrally buoyant particles remained constant throughout the duration of the flow step (Fig. 4.14c2). Whereas, the shear stress distribution for the dense suspension shows the development of a high shear stress region at the bottom of the fracture (Fig. 4.14c1). This high shear stress region at the bottom fracture surface suggests gravity-driven particle migration leads to an extended region with an increased solid content (blue circles in Fig. 4.14b1).

Figure 4.14d shows the pressure gradient sampled at $x = 1.0$ m. The plot shows a large step-decrease in ∇P, caused by the instantaneous decrease in velocity (flow rate decreased from $Q = 6.0 \rightarrow 3.0$ ml min^{-1} at time $t = 0$). For the neutrally-buoyant suspension ∇P remained almost constant after the initial decrease, but for the suspension with dense particles ∇P gradually rebounds to an intermediate value. The magnitude of the rebound is consistent with that observed in the experiments. Furthermore, the time evolution of the ϕ-distribution and its effect on the shear stress support the conclusion that the transient ∇P observed during the experiments was due to a gradual redistribution of ϕ, which caused a corresponding increase in shear stress on the bottom surface of the fracture.

The pressure gradient plot for the stepped flow experiment shows that ∇P reached a steady state over a timescale that is independent of flow rate (Fig. 4.11b). This suggests that the timescale of particle rearrangement across the fracture after each flow rate change is also time independent. The two mechanisms controlling cross-flow transport of suspended particles are: shear-induced normal stress differences, which drive particle motion from regions of high shear-rate to regions of low shear-rate and gravity driven particle settling. Shear-induced particle migration can be approximated as a diffusive process, in which particles must travel a distance of half the aperture, $h/2$, before the suspension reaches its fully developed distribution (Nott and Brady, 1994). For a concentrated suspension this timescale is given by $t_{diff} \sim \frac{h^3}{a^2}\frac{1}{4\bar{u}}$ (Leighton and Acrivos, 1986). The corresponding timescale for gravity driven migration is given by $t_{set} = \frac{h}{u_s f(\phi)}$, where $u_s = 2g\Delta\rho a^2/9\eta_f$ is the Stokes settling velocity of a

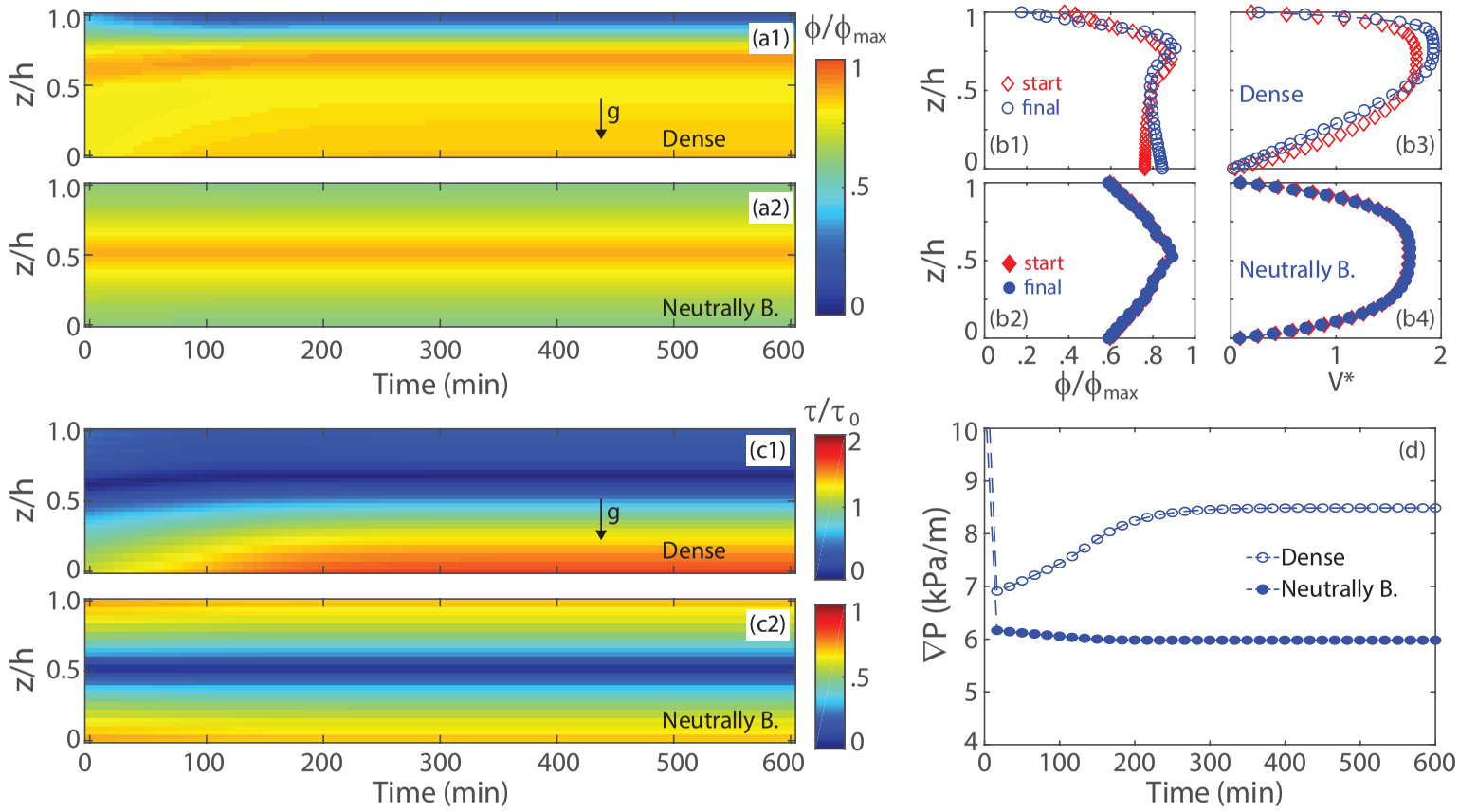

Figure 4.14: Simulation results for a concentrated ($\phi_0 = 0.5$) suspension flowing inside a long rectangular channel, after a step change in flow rate $Q = 6.0 \rightarrow 3.0$ ml min^{-1}. (a1-2) Normalized concentration distribution, ϕ/ϕ_{max}, across the fracture aperture; sampled at $x = 1.0$ m; (b1-2) normalized concentration profiles, ϕ/ϕ_{max} and (b3-4) normalized velocity profiles, $V^* = u/\bar{u}$; (c1-2) normalized shear stress, τ/τ_0; and (d) pressure gradient, ∇P.

single particle, $f(\phi)$ is the hindrance function (see Eq. A.5 in supplementary material), and their product is the hindered settling velocity. Note, η_f depends on $\dot{\gamma}$, but for the settling of particles flowing with the suspension, $\dot{\gamma}$ scales with the settling velocity, not the flow rate such that η_f can be approximated by η_{f_o}.

We can quantify the relative effect of shear-induced particle migration to gravity-driven settling by taking the ratio of the diffusive and settling timescales:

$$t^* = \frac{t_{diff}}{t_{set}} = \frac{2h^2 g \Delta\rho}{9\eta_f \bar{u}} \frac{f(\phi)}{4} \tag{4.5}$$

Since both timescales depend on the square of the particle size, taking the ratio of the diffusive and settling timescales removes the particle size dependence. Furthermore, when $t^* = \mathcal{O}(1)$ both the settling and diffusive timescales are of the same order of magnitude. In the experiments, the diffusive timescale is smaller than the settling timescale ($t^* = 0.04$) at the highest flow rate, while at the lowest flow rate, both timescales were of the same order of magnitude ($t^* = 1.21$). This suggests the settling timescale controls the transient behavior observed in our experiments. This is supported by Fig. 4.11b, which shows the transient timescale is independent of the average velocity. In the experiments, the time it takes the transient ∇P to reach steady-state is on the order of 60 minutes. This is the time it takes the larger particles in the concentrated suspension to settle a distance equal to the fracture aperture, h. This suggests that even in a multimodal dense suspension, settling of the larger particles controls the timescale required to reach steady state.

Changing the alignment of the shear plane in a two-dimensional suspension balance model provided additional insights to the complexities of three-dimensional suspension flows. Aligning the shear plane with the fracture plane, the simulations demonstrated the development of the non-uniform ϕ-distribution across the fracture width, similar to that observed in our experiments. The simulations show that the low-ϕ regions on either side of the fracture,

spanning 15% of the width, developed in the upstream tubing and expanded laterally as the suspension flowed through the diverging manifold. Aligning the shear plane with the aperture plane, demonstrated that particle rearrangement due to setting controls the evolution of ϕ across the fracture aperture. This evolving ϕ-distribution changed the shear-stress distribution and directly impacted the long-time transient ∇P response observed in our experiments.

4.6 Conclusion

We studied the flow behavior of a concentrated suspension flowing inside a laboratory-scale analog fracture. The use of a transparent fracture allowed the direct quantification of ϕ field, velocity field, and the evolving pressure gradient as the suspension flowed through different flow geometries. Obstructions placed in the fracture flow field added shear-rate gradients in both cross-flow directions and extensional components to the flow. The experiments demonstrated that both the orientation of the obstructions and the development of non-uniform ϕ-distributions within the fracture had significant effects on the velocity and ∇P of the flowing suspensions.

Applying transmitted-light techniques allowed direct quantification of the solid concentration. Absorbance measurements captured particle-size-dependent shear-induced migration in the regions adjacent to no-flow boundaries, in which larger particles preferentially migrated from regions of high shear to regions of lower shear (e.g., away from the walls). This size-dependent migration is similar to that observed in concentric cylinders (Abbott et al., 1991) and parallel plates (Krishnan et al., 1996). Furthermore, our analysis suggests that in dispersed suspensions, larger particles migrating away from the walls displace smaller particles towards the walls, opposite to the expected shear-induced motion. This led to a small

region adjacent to the walls with a higher concentration of small particles and depleted of larger particles.

Velocity measurements revealed that the regions near the no-flow boundaries (spanning approximately 15% of the fracture width on either side) had the highest velocity, whereas the middle two-thirds of the fracture had a uniform velocity. Absorbance measurements revealed these high velocity regions were correlated with lower ϕ in these regions. Though a lower ϕ was expected near the no-flow boundaries, the extent of these low-ϕ regions was unexpected. Using the two dimensional SBM in the fracture plane, demonstrated that the non-uniform ϕ distribution formed in the inlet tubing, and was subsequently extended laterally as the suspension transition into the gradually expanding manifold. This led to relatively wide regions of lower ϕ near the walls and uniform ϕ in the middle of the fracture. This suggest that non-uniform ϕ-distributions may have a large impact on the velocity and lateral solid concentration distribution that may persist over long timescales and lengthscales. This is especially important in hydraulic fracturing where the solid distribution can have a significant effect on the permeability of the propped fracture.

The pressure gradient, ∇P, across the fracture exhibited a transient response after a step-change in flow rate. This transient behavior persisted throughout the experiment and was insensitive to flow rate or obstruction configuration. Simulating a long 2-D channel showed that the spatial-temporal evolution of ϕ-distribution across the fracture aperture was directly related to the transient ∇P response after a step-change in flow rate. As the flow rate decreased, the shear-induced particle forces decreased, compared to the gravitational forces, which led to a downward flux of particles and the formation of a region with higher concentration near the bottom fracture surface. A scaling analysis showed that for the range of experimental flow rates, the settling timescale was comparable to or larger than the 'diffusive' timescale. Therefore, the time required for ∇P to reach steady-state was controlled by the settling timescale of the larger particles in the suspension.

Though existing formulations of the suspension balance model do not allow for fully 3-D flows, our results demonstrate that important features of our experiments can be represented using 2-D idealizations of the flow geometry. We note that this approach does not represent effects arising from concurrent shear-rate gradients in the fracture plane and across the fracture aperture. These may be important, particularly in regions where large changes in ϕ in the fracture plane lead to significant in-plane velocity variations or in the vicinity of no-flow boundaries (e.g., areas of contact between fracture surfaces). Nonetheless, 2-D simulations can provide significant insights into the mechanisms controlling the distribution of suspended solids within fractures and the potential impact on velocity fields and pressure gradients. Understanding this connection between ϕ distribution and the relationship between pressure gradients and suspension velocities is important in both engineering applications (e.g., hydraulic fracturing) and natural events (e.g., mud volcanoes) where at least one of these measurements is unknown.

Chapter 5

Settling and flowback of sand-fiber proppants in a deformable fracture

5.1 Abstract

We investigated the response of a sand-fiber proppant suspension flowing and settling inside a deformable fracture subjected to an applied normal stress, σ_n. We used a transparent, laboratory-scale, fracture supported by an aluminum frame that applies a normal stress to the fracture surfaces. The suspension was composed of 17.7% sand (40/70 mesh) and 0.38% polymeric fibers for a total solid volume fraction, $\phi_{\text{total}} = \phi_s + \phi_f = 0.1808$. We quantified the solid distribution within the fracture and the evolution of the solid volume fraction, ϕ, as σ_n increased. The results showed the sand-fiber suspension formed a highly heterogeneous proppant pack, which was significantly different from the uniform solid distribution observed in settling experiments without fibers. This heterogeneity was a result of the formation of sand-fiber clumps with randomly scattered solids-free regions surrounding the clumps. As σ_n increased from 0 to 88.5 kPa, the fracture aperture decreased by up to 85% and caused

the sand-fiber clumps to act like pillars that supported the applied stress and prevented full fracture closure. At the end of the settling experiments, we simulated flowback by injecting solids-free carrier fluid, while maintaining $\sigma_n = 88.5$ kPa. Fluid flowback caused the mobilization of some solids but left the supporting pillars intact. We used a numerical model to simulate flow through the porous proppant pack and open regions of the fracture and found a correlation between ϕ and the shear-rate, $\dot{\gamma}$, of mobilized solids. Using the experimental and simulation results, we defined a mobilization threshold ($\phi < \phi_{\text{mob}}$ and $\dot{\gamma} > \dot{\gamma}_{\text{mob}}$) to understand the effect of solid mobilization in a heterogeneous proppant distribution. Simulations showed that solid mobilization may lead to the formation of highly conductive channels that significantly increase fracture permeability. Our results suggest that adding fibers to conventional sand proppants may lead to heterogeneous proppant distributions and increased fracture permeability.

5.2 Introduction

Hydraulic fracturing is an approach for inducing fractures in both rock and unconsolidated sedimentary formations. Fractures are created by injecting large volumes of fluid into the formation at pressures sufficiently greater than the minimum compressive stress to induce tensile fractures. This technique has been widely applied for hydraulic fracturing in the oil and gas industry over the past several decades (e.g., Economides and Nolte, 2000). More recently, the use of proppants has been proposed for enhanced geothermal systems (Shiozawa and McClure, 2016), contaminant remediation (Murdoch et al., 2006), and as a means to increase ground elevations to combat coastal flooding (Germanovich and Murdoch, 2010). The common technique is to inject solid particles (proppants) suspended in a viscous carrying fluid into the fracture. As fluid pressure in the fracture decreases, the stress acting normal to the fracture surfaces is supported by the proppants. A fundamental challenge to effective

hydraulic fracturing is maximizing fracture permeability during the proppant placement phase and maintaining it during the production phase as pore pressure decreases.

The permeability of propped hydraulic fractures depends on the fracture aperture, proppant properties, formation strength, and closure pressure (Economides and Nolte, 2000). Efforts to increase fracture permeability have largely focused on carrier fluid and proppant properties (Montgomery, 2013; Barbati et al., 2016; Osiptsov, 2017). In particular, adding polymers to the water-based carrier fluid (e.g., guar gum or xanthan gum) yields a shear-thinning fluid with increased viscosity at low shear rates, thereby reducing particle settling rates (Chudzikowski, 1971; Metzner, 1985; Lei and Clark, 2007; Liu and Sharma, 2005; Amundarain et al., 2009). By increasing the solids carrying capacity of the carrier fluid, it is possible to deliver more proppant to individual fractures, resulting in larger fracture apertures that are completely filled with sand (Medina et al., 2016).

Recent studies have proposed adding polymeric fibers to proppant suspensions in an effort to improve the efficiency of delivering proppant to fractures (Vasudevan et al., 2001; Bulova et al., 2006; Gillard et al., 2010). Fibers have been shown to increase the apparent fluid viscosity (Guo et al., 2005; Rajabian et al., 2008; George et al., 2011, 2012) and reduce particle settling velocities (Guo et al., 2005; Férec et al., 2008; George et al., 2011). Furthermore, experiments of fiber suspensions have demonstrated the formation of fiber 'flocs', or agglomerations of fibers, when the suspension is subjected to shear deformation (Herzhaft et al., 1996; Schmid et al., 2000). These flocs form even if attractive forces between fibers are ignored, suggesting the main mechanisms affecting the formation of fiber flocs are the mechanical contacts and hydrodynamic interactions between fibers (Herzhaft et al., 1996). Thus, floc formation depends on the aspect ratio and flexibility of the fibers, and the solid content of the fluid-fiber suspension (Herzhaft et al., 1996). Furthermore, experimental observations have shown that floc formation is enhanced for fibers suspended in polymeric solutions, such as guar-water mixtures (Guo et al., 2015) resulting in reduced settling veloc-

ities for single particles is suspensions of dispersed fibers (Guo et al., 2005; Rajabian et al., 2008; Elgaddafi et al., 2012). The formation of these fiber flocs appears to be a promising mechanism to reinforce proppant packs (Willberg et al., 2011; Potapenko et al., 2014), however, further studies on the interactions of sand-fiber mixtures is needed.

The tendency of fibers to flocculate in a suspension can promote formation of a heterogeneous distribution of solids within fractures (Medvedev et al., 2013). This has the potential to result in localized regions of highly concentrated sand and fibers separated by regions with little to no solids. When the effective stress acting on the fracture surfaces increases, these localized regions of high solids content may act as pillars to support the fracture surfaces and the regions between the pillars that are devoid of solids act as high conductivity flow channels (Howard et al., 1999; Morris et al., 2014). This has two distinct advantages over conventional proppant injection techniques. Hydraulic fracturing uses significant quantities of sand; for example, in the Marcellus formation in the United States, on average, 2,100 metric tonnes of sand is injected per well (Edwards and Celia, 2018). If sand can be effectively deposited in localized regions this quantity can be significantly reduced. In a fracture filled completely with sand, the fracture permeability is controlled by the permeability of the proppant pack. However, in a fracture with localized regions of proppant, the permeability will be controlled by the fracture aperture and connectivity of the surrounding sand-free regions, and may be significantly larger than a uniformly sand-filled fracture. These potential benefits of fiber-sand proppant injection require that the localized regions of proppant persist after stress is applied to the propping pillars and that interconnected channels develop during proppant injection or during flowback.

We investigated the behavior of a mixed sand-fiber suspension as it flowed and settled inside a laboratory-scale transparent fracture confined in a rigid frame capable of applying a normal stress, σ_n, to the fracture surfaces. Transmitted light techniques allowed visualization of proppant settling and the subsequent response to applied stresses. We developed a method

to estimate solid volume fraction, ϕ (volume of solids/total volume), using transmitted light techniques. The experiments show that adding fibers led to the formation of fiber clumps with sand particles entangled within these clumps as suggested by Willberg et al. (2011) and Potapenko et al. (2014). These sand-fiber clumps led to a heterogeneous distribution of settled solids throughout the fracture, which was significantly different than the uniform solid distribution observed in previous settling experiments without fibers. Increasing σ_n led to a decrease in fracture aperture and caused the sand-fiber clumps to act as pillars capable of supporting the applied stress and preventing fracture closure. During the flowback experiment, while applying the normal stress, we observed the mobilization of some solids, many of which were flushed out of the fracture. Using a numerical solver, we simulated flow through the heterogeneous solid distribution and explored the mechanisms controlling solid mobilization and the potential for solid mobilization to further enhance fracture permeability.

5.3 Methods

Experiments were carried out in a transparent fracture, which allowed visualization of the sand-fiber proppant as it flowed into the fracture, settled between the fracture walls, and deformed due to applied normal stresses. Here, we describe the experimental setup, the procedure used to carry out the experiments, and the image processing techniques.

5.3.1 Experimental Setup

The settling experiments were carried out inside a transparent analog fracture oriented vertically. The experimental setup included a rotating stand housing a high-resolution CCD camera (Quantix KAF-6303e), red LED backlight panel (with an emitted light wavelength of $\lambda \approx 625$ nm), electronic controllers, and the fracture cell (Fig. 5.1). We used a pneumatic

tank to inject the suspension into the fracture. The pneumatic tank consisted of a PVC pipe with a fitted funnel bottom-cap, an air inlet on the top, and a threaded cap. The tank was sealed after pouring the suspension into the tank; supplying compressed air at the top displaced the suspension out of the tank and into the fracture (Fig. 5.1). A laboratory balance measured effluent mass flow rate.

The transparent fracture was composed of two 15.2×15.2×1.2 cm flat pieces of glass sealed by two no-flow manifolds (top and bottom), inlet (left), and outlet (right) manifolds (Fig. 5.2). Initial fracture aperture was created by separating the fracture surfaces using removable plastic shims; a normal force was applied to the no-flow manifolds by the screws attached to the outer steel frame. Once the normal force on the side manifolds was enough to support the fracture surfaces, the plastic shims were removed, and we sealed the fracture using the inlet/outlet manifolds. Additionally, the glass surfaces were well mated to the fused-quartz windows by a clear PVC-gasket. Eight reverse-action pneumatic-actuators (Bimba SR-092-R) were rigidly mounted on the top aluminum frame with the steel rod threaded to the bottom aluminum frame. The actuators were externally connected using high-pressure copper tubing; supplying air to the copper tubing ensured all actuators received the same air pressure. The air supplied to the actuator cylinder forced the steel rod to move into the cylinder, forcing fracture closure by lowering the top aluminum frame towards the bottom frame which was secured to the imaging stand. Four linear variable displacement transducers (LVDT, Schaevitz HCD 250) rigidly mounted on opposite sides (two on each side) of the fracture cell accurately (±1 μm) measured displacement of the upper aluminum frame throughout the experiment (Fig. 5.2).

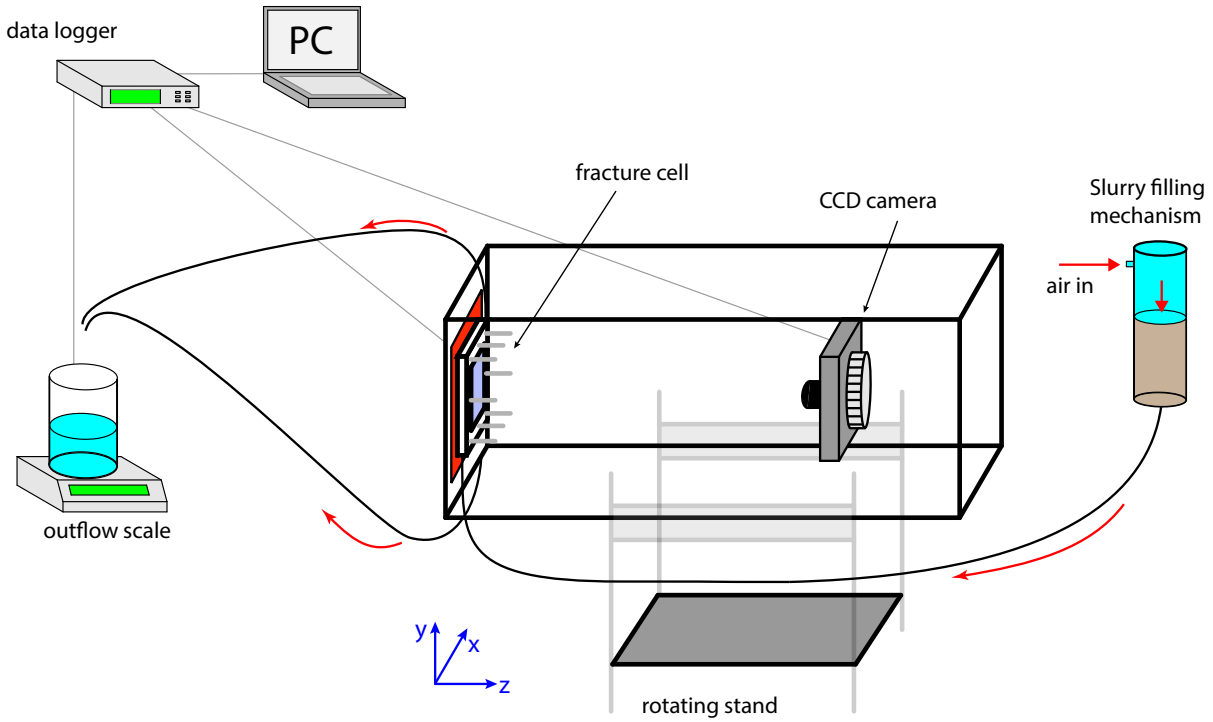

Figure 5.1: Schematic of experimental system. The slurry-filling mechanism consisted of a pneumatic tank, a PVC pipe with a fitted funneled end-cap. After the slurry was poured into the pneumatic tank, the tank was sealed and pressurized air was supplied, which displaced the slurry out of the the tank and into the fracture. Once a steady-state flow rate was achieved, the flow was stopped and slurry allowed to settle inside the fracture cell (See Fig. 5.2 for details). After the slurry settled for some predetermined time, a normal stress was applied to the fracture cell by activating the pneumatic actuators.

5.3.2 Experimental Procedure

The carrier fluid was prepared by mixing deionized de-aired water, guar gum (0.48% W/W), and glutaraldehyde (0.01% V/V) in a laboratory-grade blender for ∼15 minutes. The carrier fluid was then placed under vacuum for 12 hours to remove air bubbles trapped during the mixing process. A detailed description of the preparation method for the carrier fluid was provided by Medina et al. (2015). We used a flat-plate viscometer to measure the viscosity of the guar-water mixture. The fluid exhibits a pseudo-plastic shear thinning behavior with an apparent viscosity of $\eta_0 = 2.8$ Pa·s in the low shear-rate regime, i.e., in the Newtonian

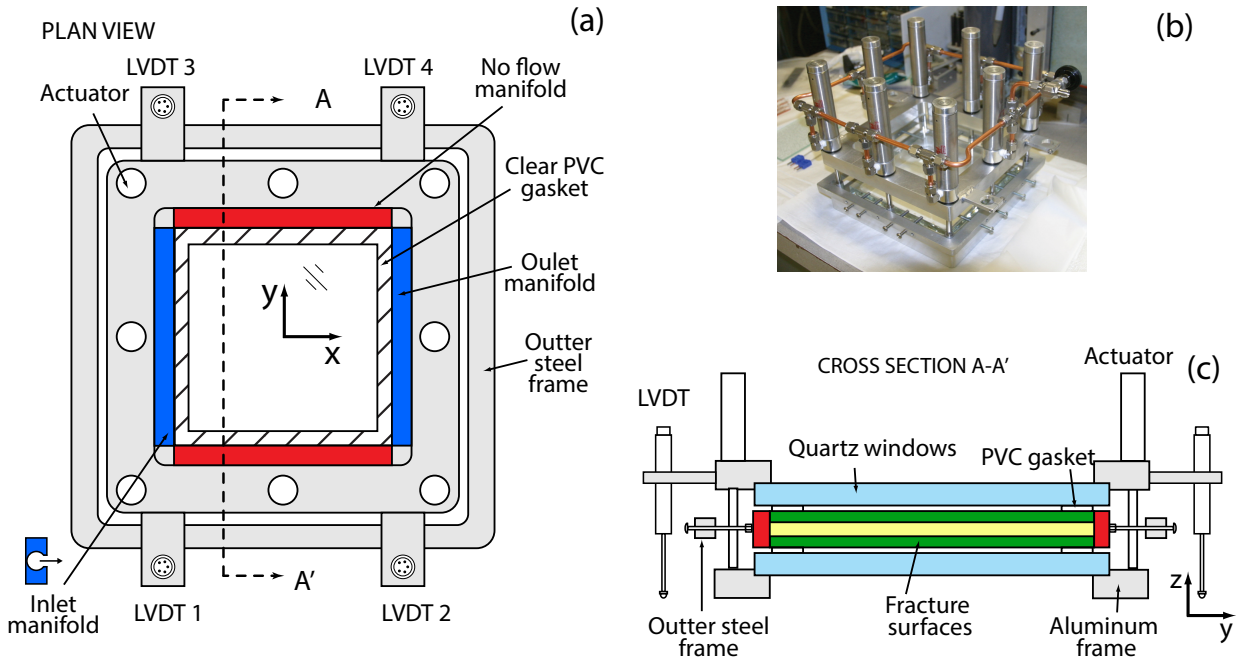

Figure 5.2: Schematic and photograph of the fracture cell used in our experimental system. (a) Plan view of the fracture cell showing the location of all eight pneumatic actuators, LVDTs, and inlet and outlet manifolds; (b) photograph of the fracture cell; and (c) cross-section view (A-A') of the fracture cell showing the fracture walls and inlet/outlet manifold configuration. For all experiments, flow was along the x-axis and gravity points in the negative y-direction.

regime. The shear thinning viscosity can be modeled using the non-Newtonian, Ellis model given by

$$\eta(\tau) = \frac{\eta_0}{1 + \left(\tau/\tau_{1/2}\right)^{\beta-1}} \tag{5.1}$$

where $\tau_{1/2}$ is the shear stress where $\eta = \eta_0/2$. Using a least-squares fit of Eq. 5.1 to the measured data resulted in estimates of $\tau_{1/2} = 5.76$ Pa and $\beta = 3.30$.

The sand-fiber suspension was prepared by slowly adding 40/70-mesh silica sand (particle radius ranging from $a = 0.13$ to 0.24 mm) and polymeric fibers (fiber length $l_f \approx 10 \pm 2$ mm and diameter $d_f \approx 12 \pm 2\mu$m) into the carrier fluid using a rotary mixing paddle. The suspension was prepared by initially adding $\sim 30\%$ of the total sand and slowly adding fibers

while the rotary paddle mixed the suspension. After adding approximately two-thirds of the fibers to the suspension, we added additional $\sim$ 30% of sand, mixed for several minutes, and, finally, added the remaining fibers and sand. Adding solids in small amounts, before and during the fiber mixing process, helped disperse the fibers within the suspension. The final suspension had a total solid volume fraction of $\phi_{\text{total}} = \phi_s + \phi_f = 0.1808$, with most of the solid volume fraction made up of sand particles ($\phi_s = 0.177$) and fibers making up the remainder of the solid volume fraction ($\phi_f = 0.0038$).

We carried out three different experiments (referred to in the text as tests A, B, and C) to investigate the settling behavior of sand-fiber suspensions. To explore reproducibility, all experiments were initialized using the same procedure, which we briefly summarize here. Initially, the fracture and all the tubes were filled with carrier fluid. We acquired a set of reference images with the cell completely filled with carrier fluid. Image acquisition began before injecting the suspension to capture the entire process, i.e., initial filling and settling. Immediately after mixing, the suspension was transferred to a pneumatic tank and injected into the fracture at a flowrate of $\sim$ 400 ml/min until $\sim$10 fracture volumes had passed through the system (about 5 minutes). We allowed the suspension to settle uninterrupted for approximately 25 minutes before applying a normal stress. We incrementally increased the normal stress, σ_n, at regular time intervals of $\sim$50 minutes, from 12.6 kPa up to a maximum of 88.5 kPa. Each actuator applied the same force to the aluminum frame, which was about 0.82 of the supplied air pressure. We assumed the total force was uniformly distributed on the fracture surface. Reported σ_n values are the uniform stress on the fracture, which was calculated by adding the forces from the eight actuators and dividing by the area of the fracture surface. At the end of the settling experiment, while maintaining $\sigma_n = 88.5$ kPa, we performed a flowback experiment by injecting carrier fluid at flow rates ranging from 100 to 300 ml/min.

5.3.3 Image Analysis

Light transmission techniques allowed us to accurately measure the fracture aperture field, b_{ij}. We acquired two reference images, one with the fracture filled with deionized water and one with the fracture filled with dyed water at a known concentration. The raw intensities were used to calculate the absorbance field using the Beer-Lambert law, $A_{\text{dye}} = \ln(I_c/I_d)$, where I is the light intensity, and subscripts c and d denote the clear and dyed solution, respectively. Using the Beer-Lambert law, absorbance was related to the aperture field by using an independently measured mean aperture, for more details see Detwiler et al. (1999):

$$b_{ij} = \frac{A_{\text{dye}_{ij}}}{\langle A_{\text{dye}} \rangle} \langle b \rangle \tag{5.2}$$

where b_{ij} is the aperture at fracture location (i, j), A is the absorbance, and $\langle \cdot \rangle$ is a spatial average. The mean and standard deviation (in parenthesis) of the initial aperture was 3114 μm (116), 2865 μm (174), and 2692 μm (110) in tests A, B, and C, respectively.

5.3.4 Solid Volume Fraction Estimation

Using light absorbance and scattering theory for a *slab* of particles (Bohren and Huffman, 2008), we derived a relationship for light absorbance as a function of ϕ_s within the fracture as

$$A = \phi_s \alpha_s b \tag{5.3}$$

where b is the fracture aperture, $A = \ln(I_{cf}/I_s)$ is the absorbance, I_{cf} is the light intensity transmitted through the carrier fluid, I_s is the light intensity transmitted through the sand/carrier fluid mixture, and $\alpha_s = C_{\text{ext}-s}/V_{\text{s}}$ is the light absorbance coefficient, e.g., ab-

sorbance per unit length. The absorbance coefficient is the ratio of the extinction cross section $C_{\text{ext}-s}$ (a measure of total light attenuated) to the actual volume of the sand particles, V_s; thus, α has units of $length^{-1}$.

Using Equation 5.3, we measured the absorbance coefficient of sand by carrying out a settling experiment. We prepared a concentrated ($\phi_s = 0.5$) suspension of silica sand (40/70-mesh) using a procedure similar to that described in Section 5.3.2. The suspension was injected into a uniform-aperture fracture and allowed to settle undisturbed for 6 days, which ensured settling reached steady state. Because the sand particles settled undisturbed (without shaking or vibration), we assumed the settled solid concentration inside the fracture reached a value close to the random loose packing limit, $\phi_s \rightarrow \phi_{\text{rlp}} \approx 0.55$ (Shapiro and Probstein, 1992), and $\alpha_s \approx A_{ij}/(\phi_{\text{rlp}} b_{ij})$. The mean absorbance coefficient of 40/70-mesh silica sand was $\langle \alpha_s \rangle = 1.3 \times 10^{-3}$ μm^{-1} with a standard deviation of $\sigma_{\alpha_s} = 6.9 \times 10^{-5}$.

Light absorption scales linearly with all components attenuating light (Bohren and Huffman, 2008), therefore, light absorbance through the sand and fiber suspension scales as

$$A = \phi_s \alpha_s b + \phi_f \alpha_f b \tag{5.4}$$

where the subscripts s and f denote the sand and fiber, respectively, and the absorbance coefficient of fibers was defined as $\alpha_f = C_{\text{ext}-f}/V_f$, where $C_{\text{ext}-f}$ is the extinction cross section of fibers and V_f is the volume of a fiber particle. Both sand and fiber particles are much larger than the wavelength of the light-source; therefore, we can use scaling arguments from Mie-scattering theory to assume that $C_{\text{ext}-s}/A_{\text{proj}-s} \approx C_{\text{ext}-f}/A_{\text{proj}-f}$, where A_{proj} is the projected area of the particle, normal to the incident light. We assumed the projected area of fiber and sand particles to be that of a rectangle ($A_{\text{proj}-f} = l_f d_f$) and circle ($A_{\text{proj}-s} = \pi a^2$), respectively. The light absorbance of fibers can, therefore, be estimated using the independently measured α_s as

$$\alpha_f = \langle \alpha_s \rangle \frac{A_{\text{proj}-f}}{A_{\text{proj}-s}} \frac{V_s}{V_f} = \langle \alpha_s \rangle \frac{16a}{3\pi d} \tag{5.5}$$

where sand particles are approximated as spheres and fiber particles as cylinders. Due to the heterogeneity of fiber suspensions (e.g., flocculation), it was difficult to estimate the local fiber concentration using our experimental system. We used a first-order approximation of the local fiber concentration by calculating the total area covered by solids and normalizing the bulk fiber concentration by this area. Such normalization was applied in the regions identified as having solids: in solids-free regions $\phi_f^* = 0$ and in regions where solids were found, we set $\phi_f^* = \phi_f / A_{\text{solids}}$; here, A_{solids} is defined as the fraction of the total area identified as having solids. Using the above analysis and assumptions yields

$$\phi_s = \frac{A - \alpha_f \phi_f^* b}{\alpha_s b} \tag{5.6}$$

where α_s was measured in the constant-aperture experiment, α_f was estimated using Eq. 5.5, A was measured using light transmission techniques, and b was calculated by adjusting the aperture field based on recorded displacements by the LVDTs. A, b, ϕ_s, and ϕ_f^* in Eq. 5.6 vary over the fracture (i, j), while α_s and α_f are constants. This analysis yields a robust quantitative measure of the solid volume fraction and gives a measure of the evolution of ϕ_s throughout the duration of the experiment. Fig. 5.3 shows a snapshot (subset) of these ϕ_s-fields at different times throughout the experiments. Note for the remainder of the text we dropped the the subscript s from ϕ_s, unless otherwise noted.

5.4 Results

In this section, we present the experimental results of the initial suspension injection and settling, fracture displacement, and solid volume fraction changes due to the applied normal

stress. We then present the experimental results of fluid flowback. We used the resulting solid distribution from the experiments to model fluid flowback using the numerical formulation presented in Appendix C.1.

5.4.1 Initial Flow and Settling

The sand-fiber suspension was injected into the fracture at a flow rate of approximately 400 ml/min for about five minutes. Following the initial injection, flow stopped, and the solids settled uninterrupted (without an applied stress) for $\sim$ 25 minutes. The ϕ-fields in all experiments showed a similar solid distribution immediately after the suspension was injected into the fracture (first column in Figure 5.3). These ϕ-fields show the suspension was dispersed throughout the entire fracture and the solids were heterogeneously distributed. This heterogeneity was due to the formation of sand-fiber clumps or aggregates resulting from the relatively high ϕ_s (compared to ϕ_f), which reduced the space between fiber particles and increased the probability of contact between fibers. The ϕ-fields show these clumps had a higher solid concentration ($\phi \approx 0.25$) than the initial solid concentration ($\phi \approx 0.18$).

The uninterrupted settling period led to significant differences in ϕ-distribution compared to the initial distribution (second column in Figure 5.3). The ϕ fields suggest there was differential settling between sand-fiber clumps and sand particles not interlocked in the clumps. That is, the sand-fiber clumps were immobilized, e.g., they were trapped or jammed between the fracture walls. Immobilization suggests these clumps were supported by shear stresses between the solids and the fracture walls. Sand particles not interlocked inside sand-fiber clumps settled at a significantly faster rate; however, some particles settled on top of the immobilized sand-fiber clumps. This settling process resulted in a heterogeneous ϕ-field with the sand-fiber clump regions having significantly higher solid content and some solids-free regions randomly scattered around the sand-fiber clumps. During this uninterrupted

settling phase, most solids from the top region of the fracture settled toward lower regions, which led to the formation of a large gap or channel near the top of the fracture. At the end of the initial settling phase, the clumps reached a sand concentration of $\phi \sim 0.25$ to 0.35; there were also visible solids-free pockets ($\phi = 0$) surrounding these clumps.

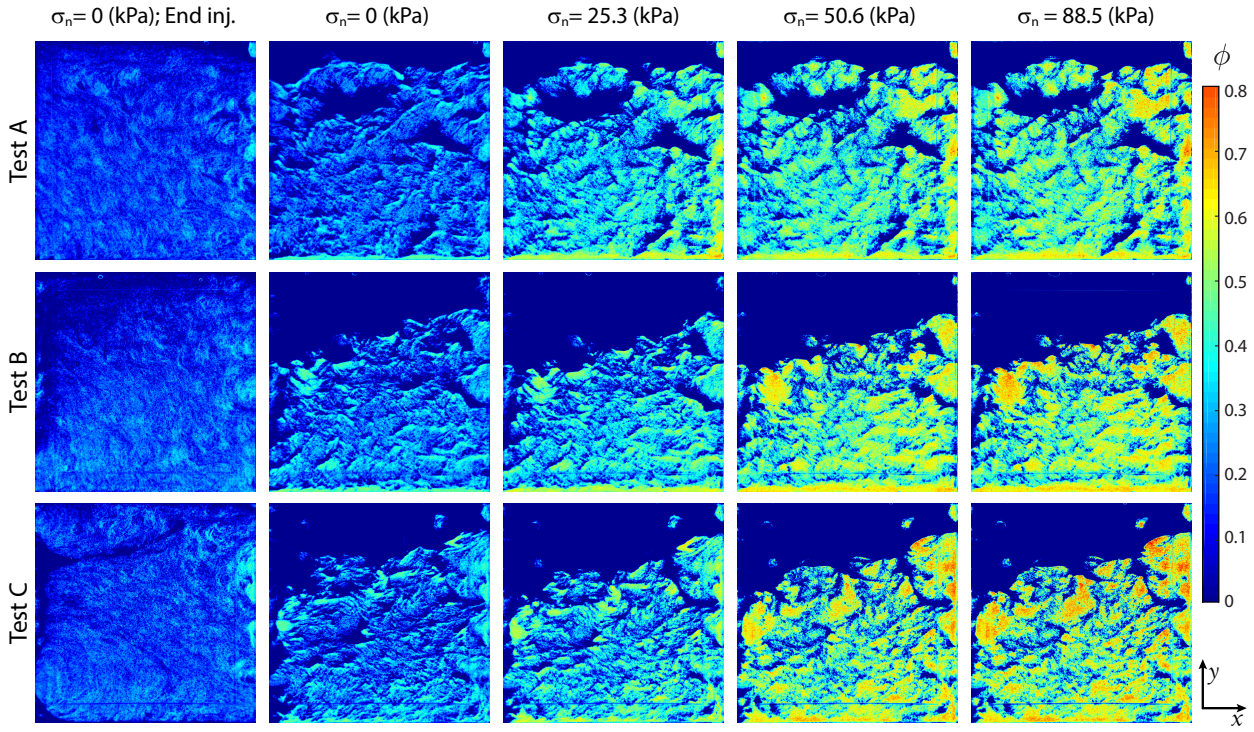

Figure 5.3: Solid volume fraction (ϕ) distribution for tests A-C. As the applied stress increased, the solids are compacted and the stress is transferred from the boundaries to the solids. The compacted solids at the higher σ_n act as pillars, which prevent full fracture closure. The suspension was injected in the positive x-direction and gravity acted in the negative y-direction.

5.4.2 Solid Volume Fraction and Fracture Closure Due to Applied Stress

After the uninterrupted settling phase, we investigated the response of the sand-fiber proppant to an applied stress, simulating the shut-in phase of hydraulic fracturing. The normal stress was increased by 12.6 kPa every ~50 minutes up to a maximum of $\sigma_n = 88.5$ kPa

with the fluid pressure maintained at $\sim$ 4.5 kPa. The LVDTs securely mounted on the top aluminum frame measured the displacement of the top fracture surface. Figure 5.4 shows the LVDT displacements relative to the initial mean fracture aperture, $\langle b \rangle$. During the initial injection of the suspension, fracture aperture increased by $\sim$ 50-100 μm in all three experiments. After suspension injection stopped, the fracture aperture returned to its initial position ($\pm$3 μm); the uninterrupted settling phase had no effect on the fracture aperture.

LVDT displacements show that applying a normal stress to the fracture reduced the fracture aperture. Figure 5.4 shows the fracture aperture decreased $\lesssim$ 100 μm after the normal stress was increased to σ_n =12.6 kPa. Increasing σ_n from 25.3 to 37.9 kPa, caused the fracture aperture in all three experiments to decrease significantly ($\sim$ 1500 μm). The fracture aperture decreased by $\sim$ 100 μm, after every σ_n step increase higher than 37.9 kPa. Furthermore, as σ_n increased, the aperture decreased non-uniformly, i.e., the aperture on the upper region of the fracture (LVDT 3 and 4) decreased more than aperture near the bottom of the fracture (LVDT 1 and 2). This non-uniform aperture reduction was likely due to the relatively low solid content in the upper regions of the fracture and resulted in an aperture decrease of $\sim$ 85% in the upper region and $\sim$ 40% in the lower region of the fracture. Figure 5.5a shows that as σ_n increased the mean aperture decreased significantly, reaching a 55% reduction at the highest applied normal stress. Though the aperture decreased significantly due to the applied stress, the fracture remained open, which suggests that some (if not all) solids were supporting the applied stress.

The results show that as σ_n increased, the fracture aperture decreased, which caused a significant increase in ϕ. The procedure to estimate ϕ using optical measurements was based on the assumption that total absorbance is linearly proportional to the absorbance of all components, e.g., sand, fibers, and fluid (Sec. 5.3.3). Furthermore, based on scaling arguments, we assumed the unknown optical properties of fibers (α_f) could be derived from the measured optical properties of sand (α_s). Though both of these assumptions were reasonable

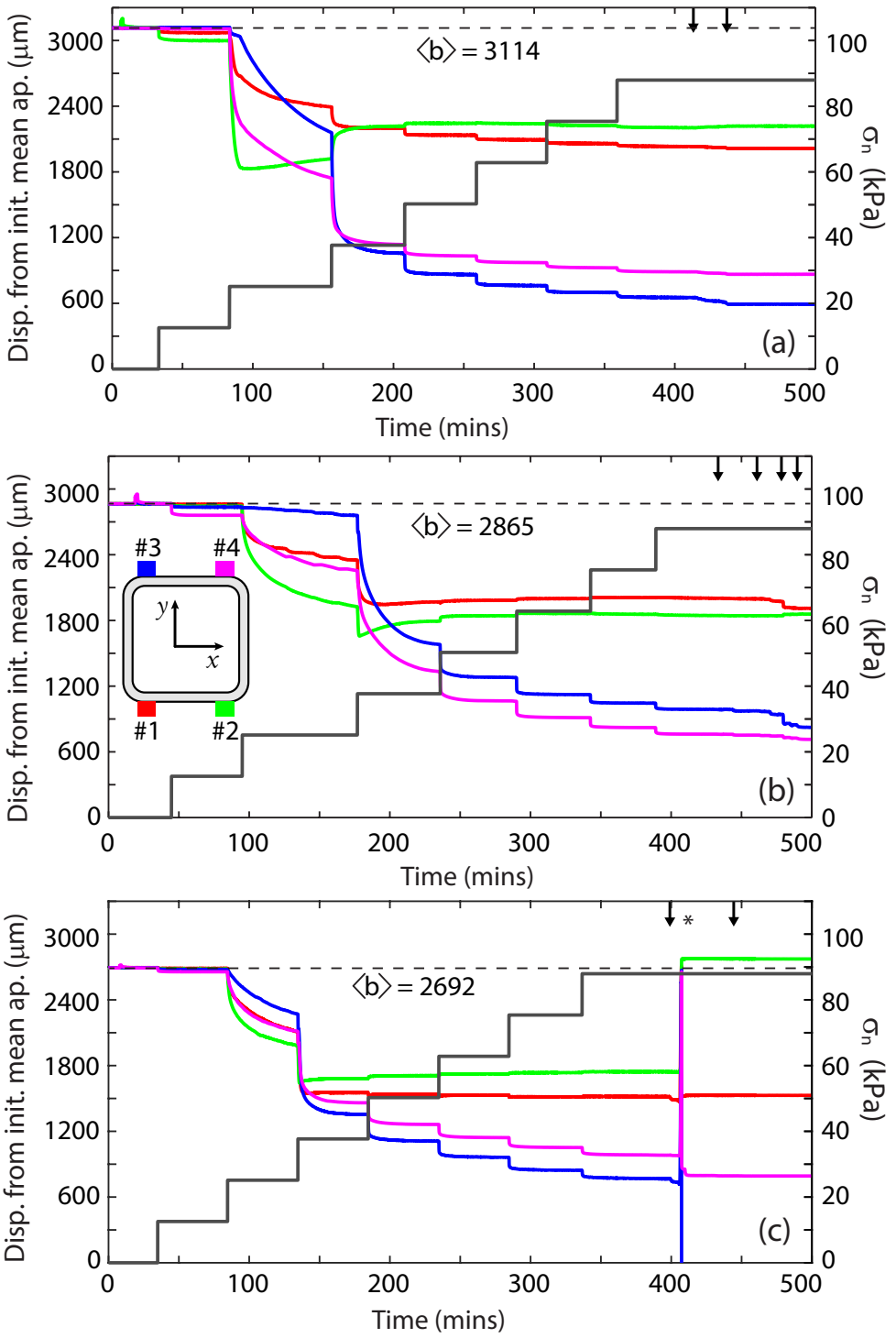

Figure 5.4: Fracture aperture reduction as σ_n increased. Panels a-c show displacement data for tests A-C, respectively. The black line shows the applied normal stress, and the colored lines correspond to the LVDT locations as indicated in Fig. 5.2 and shown in the inset in panel b.

(Bohren and Huffman, 2008), it was important to quantify the relative error associated with our ϕ estimates. Performing an uncertainty analysis, we found the relative error of our ϕ estimates to be 6% (see supporting material for more details). Furthermore, we verified that the procedure was accurate by performing a mass balance of the solids inside the fracture. Using the ϕ-fields and known aperture fields, we estimated the volume of solids inside the fracture as σ_n increased. Figure 5.5b shows that the total volume of sand was conserved in all experiments. These results show that although the ϕ-fields exhibited large changes in response to the aperture decrease induced by the increased σ_n, the volume of solids inside the fracture remained constant. The low relative uncertainty and the constant volume of solids inside the fracture suggest the assumptions made when deriving the ϕ estimates were adequate for this analysis.

At the end of the experiments, ϕ-fields showed a highly heterogeneous solid distribution throughout the fracture (last column in Fig. 5.3). In addition to the heterogeneous solids placement within the fracture, there was heterogeneity in solid concentration, e.g., not all solids had the same ϕ. This ϕ-heterogeneity resulted from the aperture decrease, which caused rearrangement of sand particles, and a corresponding decrease in void space between the solids, or local increase in ϕ. Figure 5.3 shows most solids had a concentration higher than the initial solid content of the suspension. As σ_n increased, some clumps reached $\phi \sim$ 0.6 to 0.65, whereas some sand-fiber clumps in the top regions of the fracture had slightly higher solid concentration, $\phi \sim 0.75$ which was a result of the non-uniform displacement of the top fracture surface. The high ϕ values confirm the fiber clumps were interlocked with sand particles, which compacted as the aperture decreased.

The solid volume fraction can be used as an indicator of the solids' ability to support an externally applied load. As ϕ increases, the probability of a particle being in contact with more than one particle increases. As the void space between particles decrease, the solids may reach a stable configuration capable of supporting an externally applied load. The

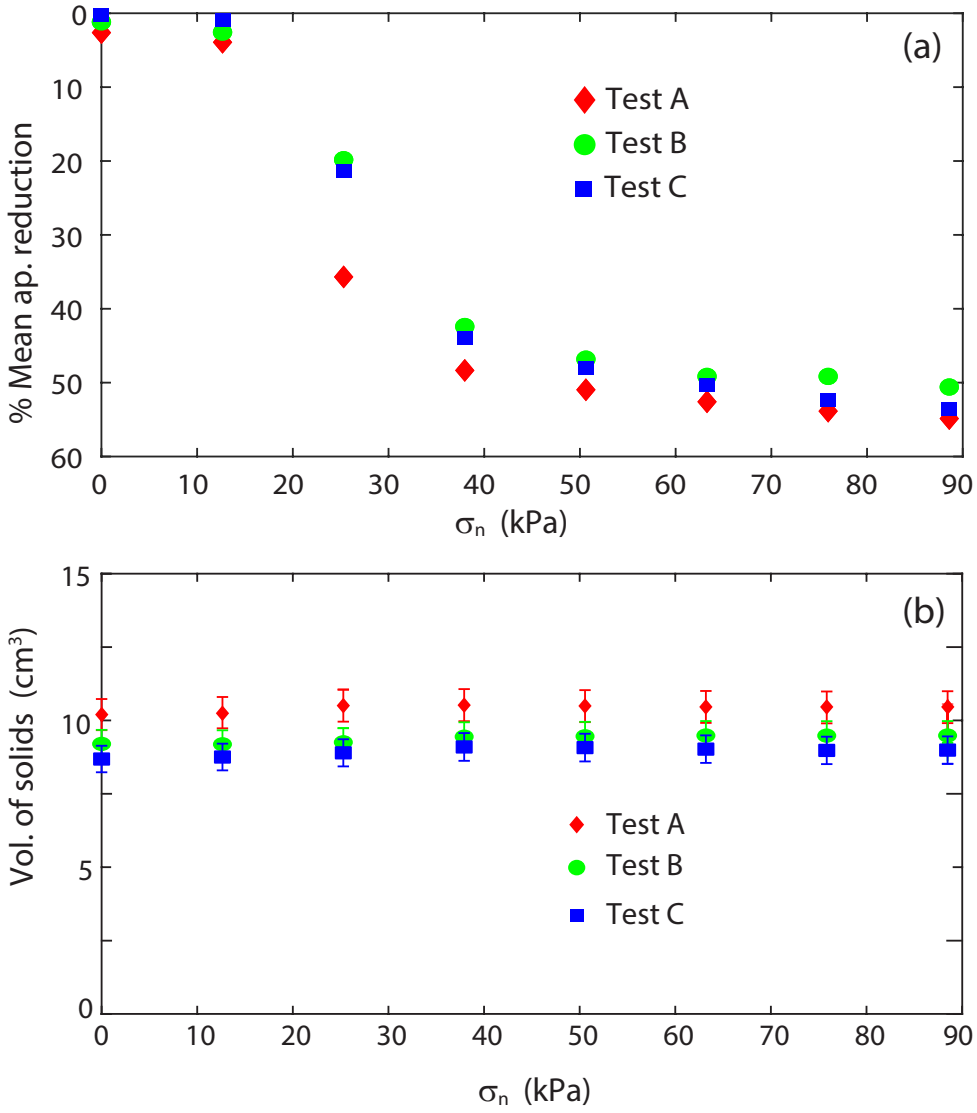

Figure 5.5: (a) Percent mean aperture reduction, relative to the initial mean aperture. As σ_n increased, the mean aperture decreased significantly. At the highest applied normal stress, the mean aperture decreased up to 55% in all three experiments. (b) Average volume of solids at the end of each applied normal stress step. Conservation of volume suggests our analysis for the approximation of ϕ was valid.

concentration at which this stable configuration occurs is the jamming transition or the point at which the behavior of suspended solids transitions from fluid-like to solid-like. This transition occurs at a concentration between the random loose packing limit (ϕ_{rlp}) and the random close packing limit (ϕ_{rcp}) (Shapiro and Probstein, 1992; Santiso and Müller, 2002). For uniform-sized spheres $\phi_{\text{rlp}} \approx 0.55$ and $\phi_{\text{rcp}} \approx 0.65$, while for non-spherical polydisperse

particles $\phi_{\max} \approx 0.84$ (Onoda and Liniger, 1990; Santiso and Müller, 2002). The ϕ-fields suggests that some solids reached a solid concentration and thus a stable configuration, allowing these solids to support the applied normal stress and prevent the full closure of the fracture aperture.

We calculated the area of solids supporting the applied normal stress, i.e., *load-bearing* solids, by applying a threshold to the ϕ-fields: all solids with ϕ greater than some critical solid content, ϕ_c, were considered load-bearing. Figure 5.6 shows the area of load-bearing solids relative to the fracture area (232 cm^2) for two values of ϕ_c, e.g., $\phi_c = \phi_{rlp}$ (filled symbols) and $\phi_c = \phi_{rcp}$ (open symbols). Initially, there were no load-bearing solids, only after σ_n was increased to 25.3 kPa did a small fractions of solids become load-bearing (Fig. 5.6); note this was also the stress at which the large decrease in aperture was recorded (see Fig. 5.4). As σ_n increased, the area of load-bearing solids increased linearly (Fig. 5.6). At the end of the experiment, load-bearing solids covered 3 to 15 % (test A), 7 to 23 % (test B), and 11 to 27 % (test C) of the fracture. Note these ranges are for ϕ_{rcp} and ϕ_{rlp}. The observed increase in area covered by load-bearing regions suggests the sand-fiber pillars may be undergoing particle rearrangement, compaction, and spreading as the normal stress was increased.

5.4.3 Experimental Flowback

After solids had settled at the maximum stress ($\sigma_n = 88.5$ kPa), we conducted a flowback experiment by injecting solids-free carrier fluid at flow rates ranging from 100 to 300 ml/min. Fracture displacements recorded by the transducers show that the fluid injection had little effect on the fracture aperture in all experiments. In test A, we performed two separate injections at a flow rate of 100 ml/min and 200 ml/min; in test B four injections at a flow rate of 100, 100, 200, 300 ml/min; and in test C two injections at a flow rate of 100 and 300 ml/min. Note, the black arrows on the top of each panel in Fig. 5.4a-c indicate the

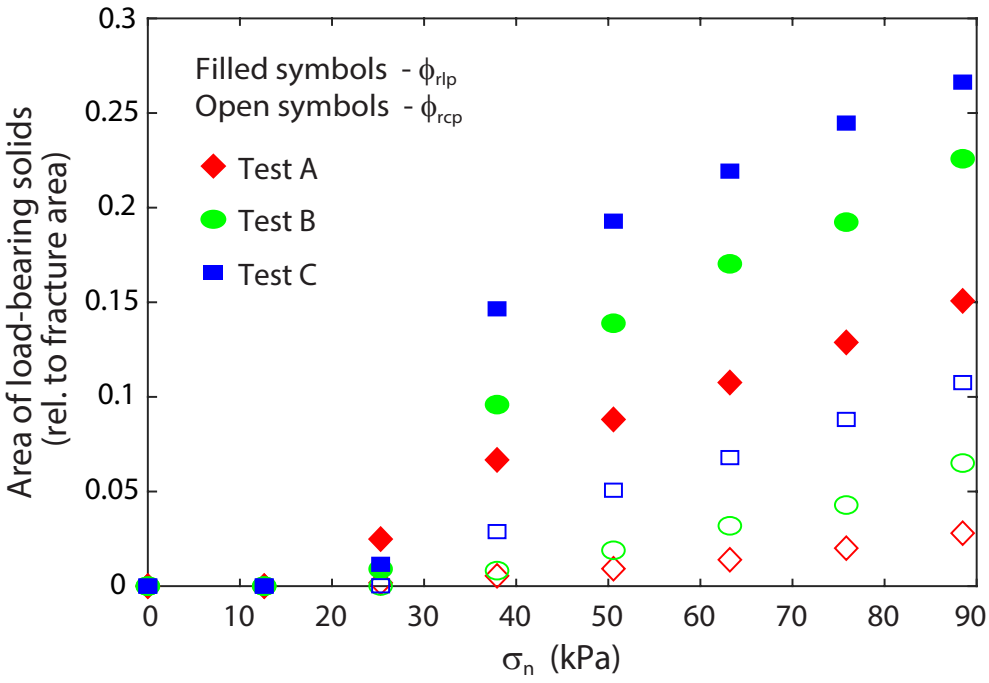

Figure 5.6: Area of load-bearing regions (relative to the fracture area). As the applied normal stress increased, the area of load-bearing regions increased which was due to compaction and spreading. Filled symbols: load-bearing ϕ set equal to $\phi_{rlp} = 0.55$. Open symbols: load-bearing ϕ set equal to $\phi_{rcp} = 0.64$. At the end of the experiments, the area covered by all solids was 174 cm^2 (Exp. A), 144 cm^2 (Exp. B), and 151 cm^2 (Exp. C). The fracture area was 232 cm^2.

injection of carrier-fluid during flowback. In all three experiments, the LVDTs displaced approximately 10 to 20 μm after each flowback injection. After 5 minutes of injection in test C, the outlet tube was inadvertently blocked, which led to a temporary increase in pore pressure resulting in a significant increase in aperture (large vertical displacements observed in Figure 5.4c). This change in pore pressure and aperture caused significant changes in ϕ-distribution with a significant amount of solids flushed out of the fracture (bottom right panel in Fig. 5.7). Subsequent fluid injection at $Q = 300$ ml/min had no effect on the rearragned solid distribution.

In addition to the relatively small changes in aperture, flowback through the heterogeneous solid distribution caused some solids to be mobilized and flushed out of the fracture. Solid mobilization was mostly observed in the area near the top of the fracture, in regions adjacent

to the large solids-free region of the fracture. Images recorded during the flowback suggest that mobilization was mainly caused by the gradual erosion from the edges of pillars. In addition to the erosion, a few small isolated pillars ($\sim$ 5mm$\times$ 5mm) were also mobilized during flowback.

Figure 5.7 shows the ϕ-distribution before and after flowback for all experiments. Solid mobilization caused the widening of the large open channels; this widening, can be seen in more detail by looking at the difference in solid content before and after flowback. The last column in Fig. 5.7 shows the difference field before and after the last flowback flow rate, e.g., at the end of Q=200 ml min^{-1}, Q=300 ml min^{-1}, and Q=100 ml min^{-1} for tests A, B, and C, respectively. Red represents locations were solids were eroded and blue shows locations were solids were deposited. Approximately 0.4 cm^3 (A), 0.9 cm^3 (B), and 2.9 cm^3 (C), were flushed out of the fracture during flowback in test A, B, and C, respectively. Additionally, the area of load-bearing solids relative to the area occupied by all solids increased after flowback in all experiments, which suggests that most mobilized solids were not load bearing. In test C, one-third of the total solids were flushed out of the fracture, the remaining solids were rearranged into a compact sand pack at the bottom of the fracture (third panel in Fig. 5.7).

The results from flowback experiments suggest the wide channels near the top acted as high-permeability conduits, which caused flow to be focused through these channels with relatively little flow passing through the sand pack. This apparent flow focusing led to the mobilization of solids in the regions adjacent to the channel creating wider channels. There were no significant changes in solid distribution, and minimal solid mobilization was observed in the bottom half of the fracture (within the sand pack). We hypothesized that there were two competing mechanisms controlling solid mobilization: the shear stress exerted by the fluid on the side of the pillars causing solid erosion and mobilization, acting against the applied normal stress (e.g., contact stress between particles) preventing solids mobilization.

We cannot measure shear stresses from our experiments, however, we can use flow simulations through this system to understand solid mobilization.

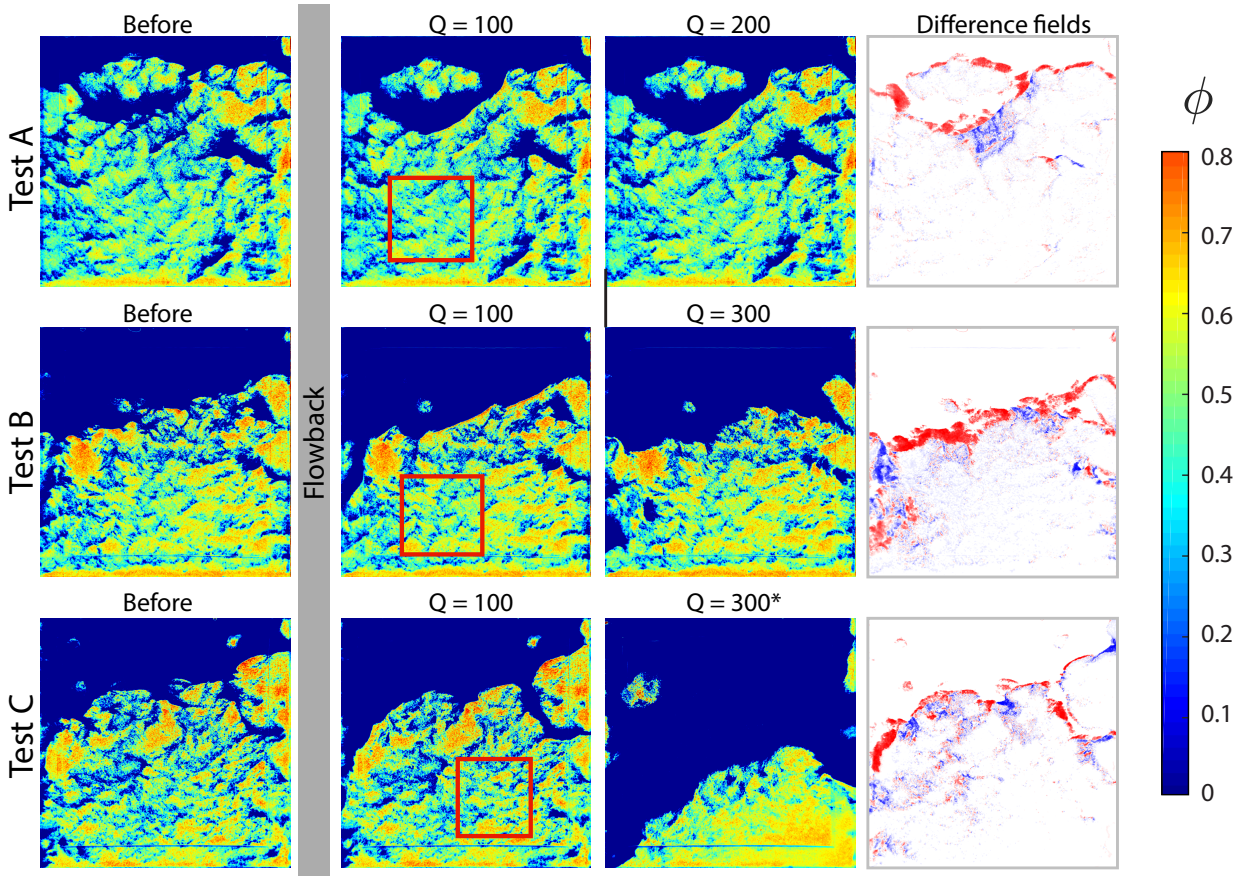

Figure 5.7: ϕ-distribution for test A-C, before and after flowback. In all cases σ_n=88.5 kPa. Most fluid flowed through the large open channel near the top of the fracture. Flowback caused some solids to be mobilized and created wider channels. The difference fields show that solids were mostly mobilized from the edges surrounding the large channel near the top of the fracture. In test C a large change in pore pressure caused solids to rearrange, see text for details. Red boxes show the location used to simulate flowback through the sand pack, see text for details.

5.4.3.1 Numerical Simulation of Flowback

We investigated solid mobilization due to flowback by simulating fluid injection through the solid distribution at the end of the experiments. The model was developed by considering flow of an Ellis fluid through a parallel-plate fracture filled with sand concentrations ranging

from 0 to $\phi_{\max}$. The numerical model is similar to a parallel-plate fracture with localized contacts (e.g., Jasinski and Dabrowski, 2018), but here the contacts are permeable. Flow through the permeable sand pack was simulated as a porous medium (Tosco et al., 2013; de Castro and Radilla, 2017). The permeability at each cell was calculated as the geometric average of permeability of a porous matrix and parallel fracture. The resulting nonlinear flow equation was solved using Picard iteration (see Supplementary Information for details of the derivation and implementation of the model). We simulated flow through the heterogeneous ϕ-distribution in our experiments by applying a constant pressure at the inlet (left) and outlet (right) and no-flux boundary on the top and bottom of the fracture and solving for the velocity field. The simulations for test A-C all show the top of the fracture had the highest velocity, which confirmed that flow was focused through the large open channel as discussed. The sand pack in the bottom regions of the fracture experienced significantly lower flow; velocity in the sand pack was several orders of magnitude smaller than velocity in the channel. Additionally, the simulations revealed that fluid moves significantly faster, by two orders of magnitude, through the solids-free regions than fluid through the sand-fiber pillar regions.

We investigated the hypothesis that solid mobilization was controlled by competing mechanisms (e.g., shear stresses exerted by the fluid and contact stresses between particles) by constructing a time-history of the flow field during flowback. This time-history was constructed by solving the steady-state velocity field for each ϕ-field (acquired image) during flowback; using this velocity field, we calculated the shear rate of the fluid, $\dot{\gamma} = \left(\left({}^{du}/_{dy}\right)^2 + \left({}^{dv}/_{dx}\right)^2\right)^{1/2}$ throughout the fracture. For every timestep, we identified the location of mobilized solids and recorded the $\dot{\gamma}$ values at those locations. We assumed the $\dot{\gamma}$ was the shear-rate required to mobilized those solids. Figure 5.8 shows the joint probability distribution of ϕ and $\dot{\gamma}$ of mobilized regions constructed over the time-history of flowback. Figure 5.8 suggests a strong correlation between $\dot{\gamma}$ generated by fluid flowback and solid mobilization: most solids were mobilized by $\dot{\gamma}$ between 0.1 and 100 s^{-1}. Furthermore, it appears that there is a critical $\dot{\gamma}_{\text{mob}}$

required to mobilize solids. Histograms of ϕ for mobilized solids show that a large fraction of mobilized solids had a low concentration (Fig. 5.8d-f). These results suggest that indeed, the two mechanisms controlling solid mobilization are the shear rates generated by the fluid and the normal forces between load-bearing solids. Figure 5.8 suggests the main mechanism of mobilization was erosion caused by the high $\dot{\gamma}$ at the fluid-solid boundary of the sand-fiber pillars. Erosion was observed in the acquired images and is supported by the high amount of mobilized solids with low ϕ values. Furthermore, the normalized histograms suggest that solid mobilization is unlikely to occur when solids reach a concentration above some ϕ_{mob}; this concentration seems to be between ϕ_{rlp} and ϕ_{rcp} (Fig. 5.8 d-f).

5.5 Discussion

The experimental procedure and relatively small scale of the fracture led to the formation of a large channel near the top of the fracture. During flowback, flow was focused through this channel with relatively little flow through the sand pack in the bottom $\sim$2/3 of the fracture. In a field application of proppant injection, proppant is typically injected radially from a well bore into a vertical fracture propagating from the wellbore. Thus, it is likely that large-scale channels such as those observed in our experiments will form far from the well bore and may have a negligible impact on fluid flow to the well. To investigate the potential impact of solid mobilization in the absence of such large-scale preferential channels, we simulated flow through a small (5.2 cm^2) region inside the sand pack (red box in Figure 5.7). Though the ϕ-distribution is heterogeneous, the initial ϕ distribution lacks a single dominant preferential flow path. The simulations were carried out by applying constant pressure on the left and right sides of the field and no-flux boundaries on the top and bottom of the field.

The flow simulations provided local measurements of $\dot{\gamma}$ throughout the flow field. We then identified locations meeting the mobilization condition, $\phi < \phi_{\text{mob}}$ and $\dot{\gamma} > \dot{\gamma}_{\text{mob}}$, and ar-

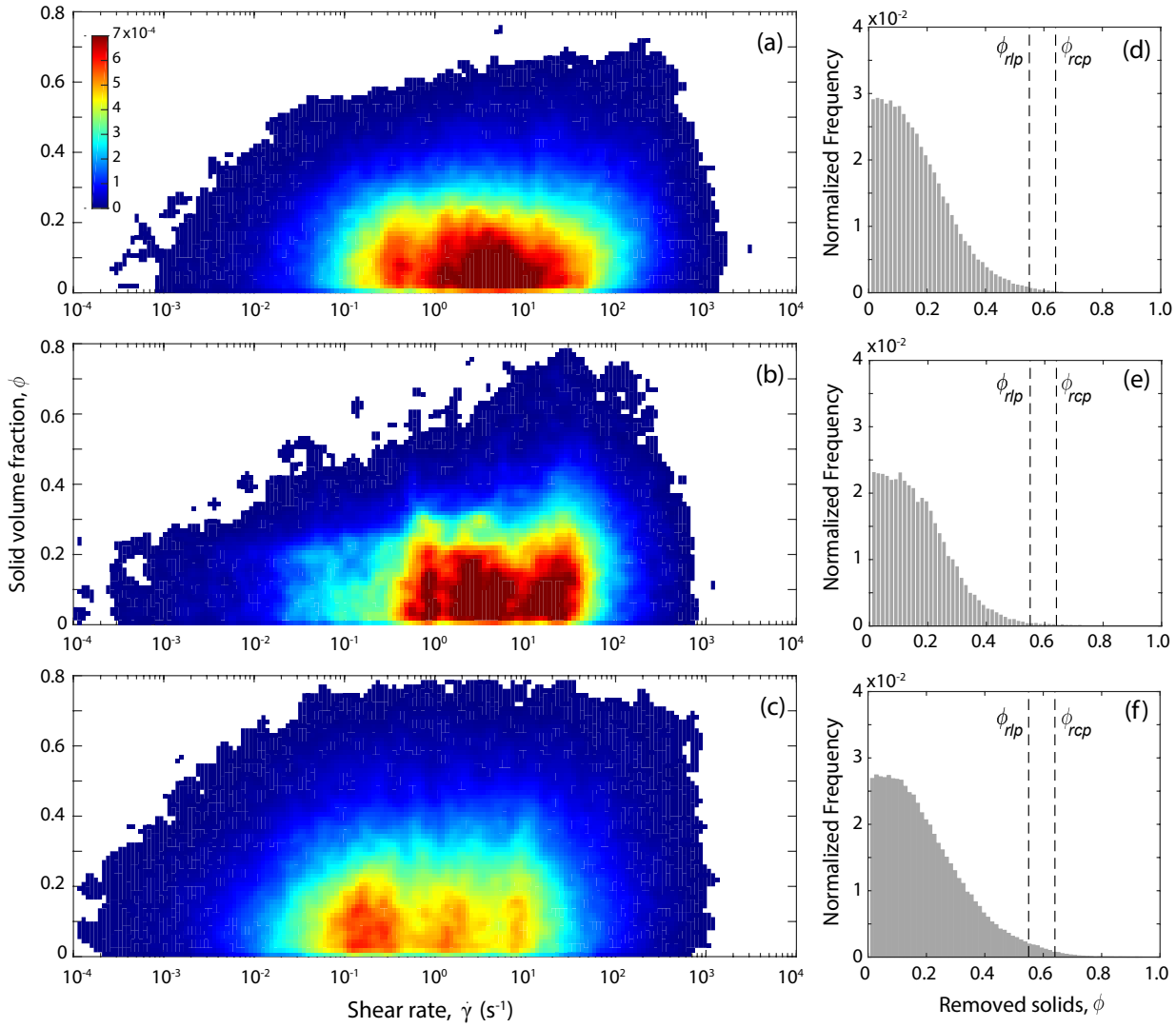

Figure 5.8: Joint probability distribution of $\dot{\gamma}$ and ϕ of solids mobilized during flowback in tests A-C, shown in panels (a)-(c), respectively. The color scale is the normalized frequency of mobilized solids locations. There appears to be a strong correlation between the mobilized solids' concentration and the shear rates generated by fluid flowback. Most solids were mobilized by the larger shear rates, whereas the lower shear rates only tend to mobilize the low-ϕ solids. Panels (d)-(f) show normalized histograms of the concentration (ϕ) of mobilized solids in test A-C, respectively.

tificially mobilized the solids at those locations by setting $\phi = 0$. The velocity field was solved again using the new ϕ field, repeating the process until the flow and ϕ fields reached a steady state. Note, we only simulated mobilization and did not consider the possibility of particle deposition. Figure 5.9 shows the steady-state ϕ-fields and velocity fields before and

after artificial solid mobilization for $\phi_{\text{mob}} = 0.55$, $\dot{\gamma}_{\text{mob}} = 0.5$ s^{-1}, and $\nabla P = 224$ kPa/m. The simulation results show artificial mobilization led to the formation of high-conductivity channels that grew from the high-$\dot{\gamma}$ regions in the thin preferential flow paths within the sand pack. As solids were mobilized channels developed and widened until the shear rate at the edge of the channel was lower than $\dot{\gamma}_{\text{mob}}$ or until the edge of the channel edge reached a region with $\phi \geq \phi_{\text{mob}}$. These simulations show that solid erosion and mobilization may lead to the formation of channels within the heterogeneous sand pack which may significantly increase fracture conductivity.

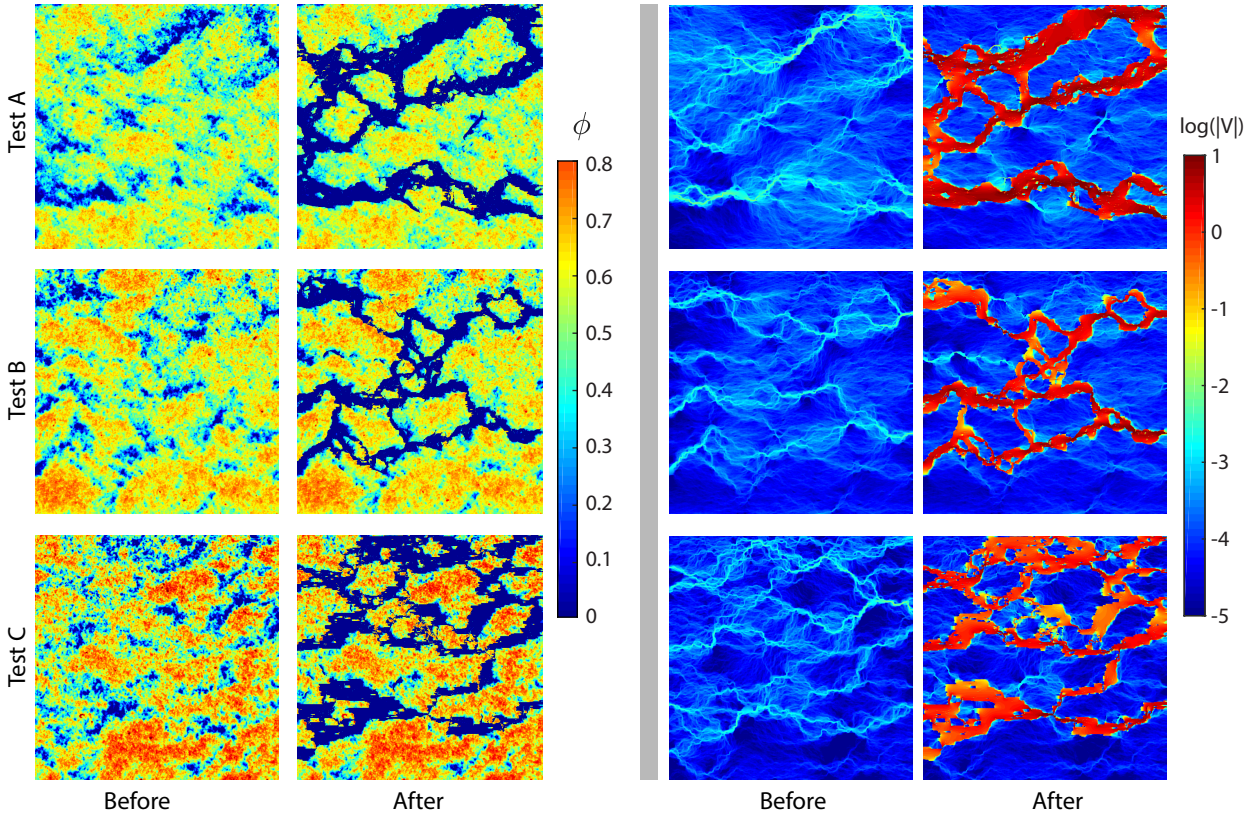

Figure 5.9: Simulation results showing the development of high-conductivity channels due to solid mobilization. The left panels show the ϕ distribution before and after mobilization. The right panels show the velocity magnitude, $|V|$, before and after erosion. The sand-pack region for these simulations is highlighted in Fig. 5.7.

We explored the effect of varying the mobilization threshold on the artificial mobilization. We simulated artificial mobilization for a range of mobilization thresholds: $\dot{\gamma}_{\text{mob}} = 5.0$ to 50.0 s^{-1} with $\phi_{\text{mob}} = \phi_{rlp} = 0.55$ or $\phi_{\text{mob}} = \phi_{rcp} = 0.65$, over a wide range of pressure

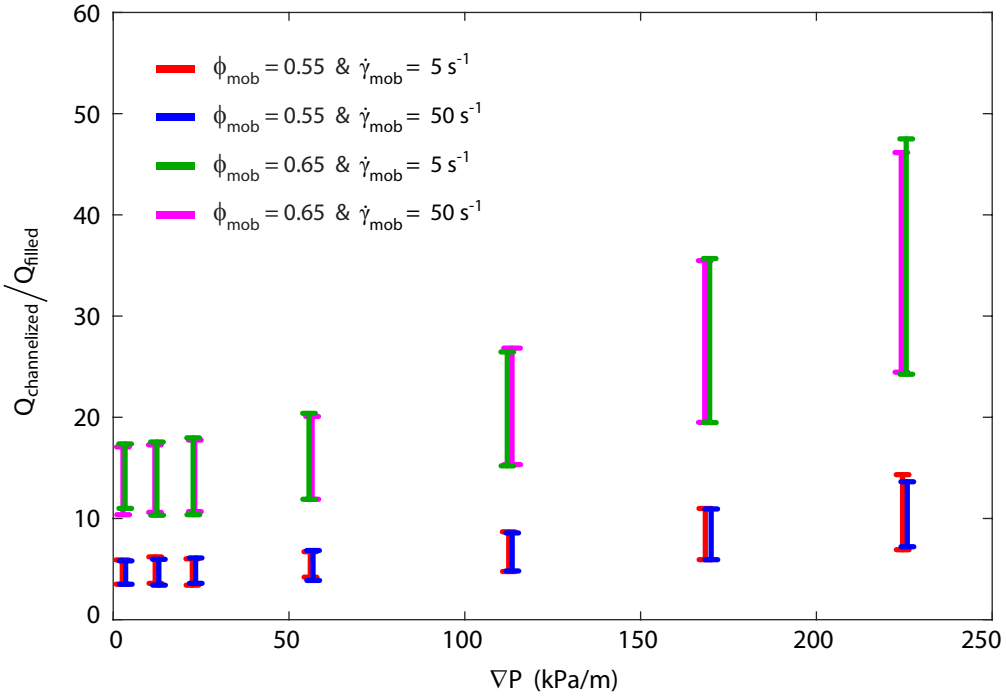

Figure 5.10: Flow rate through channelized solid distribution, normalized by the flow rate through the same fracture filled with a uniform solid content. The bars show the variability between results for the different ϕ distributions (e.g., tests A-C).

gradients, $\nabla P = 22.4 - 224$ kPa/m. We calculated the flow rate through the channelized or artificially eroded fracture ($Q_{\text{channelized}}$) and normalized by the flow rate of a fracture filled with a uniform $\phi = \phi_{\text{mob}}$ sand pack (Q_{filled}). Note that, even before solid mobilization, flow through a heterogeneous ϕ distribution was higher than flow through uniform-ϕ sand-pack. Figure 5.10 shows the normalized flow rates for different mobilization thresholds, the bar shows the variability between experiments. The results suggest solid mobilization was more sensitive to ϕ_{mob}. For the conditions tested here, flow through the heterogeneous and eroded ϕ distribution was 5 to 48 times higher than flow through a fracture filled with uniformly distributed solids. Solid mobilization in these simulations resulted in the the formation of channels ranging from 0.2 to 3.2 mm wide. These simulations suggest that solid mobilization may lead to a significant increase fracture conductivity.

5.6 Conclusions

We presented experiments in which sand-fiber proppant mixtures were injected into a vertical deformable analog fracture. Using a transparent fracture and transmitted light techniques, we developed an accurate method to quantify the ϕ-distribution of solids inside the fracture. The experimental results showed that adding polymer fibers to conventional proppants led to complex settling behavior, resulting in heterogeneous proppant placement inside the hydraulic fracture. Heterogeneous proppant placement was the result of sand-laden fiber agglomerates (e.g., sand-fiber clumps) that formed during the settling process. As we increased the applied normal stress on the fracture, the aperture decreased significantly (up to 55% mean aperture reduction from the initial mean aperture). As the aperture decreased, the solids compacted and rearranged, which resulted in some sand-fiber clumps reaching a concentration close to or higher than the jamming limit, ϕ_c. The regions with solid concentrations $\phi > \phi_c$ were load bearing, i.e., those solids supported the applied stress and prevented fracture closure. The area and concentration of load-bearing solids increased as σ_n increased, which suggests solids were spreading and compacting. At the highest applied stress, the load-bearing solids covered about 15 to 25% of the total fracture area.

Injecting carrier fluid through the heterogeneous solid distribution showed the flow was focused through the large channel near the top of the fracture. This flow focusing led to the significantly higher shear stresses in the areas near the edges of the large channel, which caused mobilization of solids. A large fraction of mobilized solids were eroded from the regions surrounding the channels, which led to the formation of wider channels. We hypothesized that solid mobilization was the result of two competing forces, e.g., the shear stresses generated by the flowing fluid acting on the edges of the solids causing mobilization and contact forces between the solid particles. Though we cannot measure the force between particles, we can use ϕ, which provides a measure of the degree of contact between particles, as an indicator of the contact forces. Using the experimental ϕ-fields and numerically

simulated flow velocities, we found a correlation between ϕ and $\dot{\gamma}$ for solid mobilization. We used the ϕ-$\dot{\gamma}$ correlation to understand solid mobilization and the relative effect of the shear rate and concentration on mobilization in a heterogeneous solid distribution without a single initial preferential flow path. The simulation results showed that solid mobilization was dependent on $\dot{\gamma}$. The resulting mobilization formed conductive channels between stable sand-fiber proppant pillars. The width of these newly formed channels were several particle diameters or larger and led to an order-of-magnitude increase in fracture conductivity.

Chapter 6

Concluding Remarks

6.1 Conclusion

In this dissertation I have investigated the behavior of concentrated suspensions flowing through confined geometries. The experimental results demonstrate that small variations ($\sim$3%) in the spatial distribution of ϕ can induce large velocity variations within the fracture, which persisted through the length of the fracture and at different flow rates. These velocity and ϕ-heterogeneities should be accounted for when predicting the solid distribution within a fracture to accurately predict the expected fracture permeability. Furthermore, the relationship between pressure and flow rate observed in the experiments was accurately predicted by the cubic law using an apparent viscosity as a function of solid concentration $\eta(\phi)$ and assuming a homogeneous suspension. The results presented here suggest that while the assumption of uniform flow may match observations of pressure drop and total flow rates, it may underestimate the time of breakthrough and degree of dispersion of the slurry transported within the fracture, which may have a significant impact on the solid distribution and thus affect fracture permeability.

The results presented in this dissertation also demonstrate that concentrated suspensions exhibit a complex flow behavior in the presence of obstructions which create shear-rate gradients in both the cross-flow direction and extensional components to the flow. The orientation of the obstructions and development of non-uniform ϕ-distributions within the fracture had significant effects on the velocity and ∇P of the flowing suspensions. I observed particle-size-dependent shear-induced migration in regions adjacent to no-flow boundaries. These size-dependent migrations caused larger particles to preferentially migrate from regions of high shear to regions of lower shear (e.g., away from the walls) and smaller particles migrating towards regions of higher shear, opposite to the expected shear-induced motion. Non-uniform ϕ-distributions are especially important in hydraulic fracturing where the solid distribution can have a significant effect on the permeability of the propped fracture.

In addition to lateral heterogeneity in ϕ-distribution, the suspensions exhibited a transient pressure gradient, ∇P, response after a step-change in flow rate, which persisted throughout the experiment and was insensitive to flow rate or obstruction configuration. Using a 2-D suspension balance model I showed that the spatial-temporal evolution of ϕ-distribution across the fracture aperture was directly related to the transient ∇P response after a step-change in flow rate. More specifically, the development of a 'settling' layer was directly correlated to the observed transient ∇P response. The results presented here suggest that concentrated suspensions exhibit complex behavior with non-uniform ϕ-distribution in both the fracture plane and aperture plane. This heterogeneous solid distribution and its effects on pressure readings are important when interpreting permeability and pressure measurements in hydraulic fracturing field operations.

Using transmitted light techniques, I developed an accurate method to estimate ϕ of solids inside transparent fractures. The experimental results showed that the addition of fibers led to a heterogeneous solid distribution with sand-fiber clumps surrounded by solids-free regions. Applying a normal stress to the heterogeneous solid distribution inside the fracture

caused some sand-fiber regions to act as pillars supporting the applied stress and preventing fracture closure. Fluid flowback through such heterogeneous ϕ-distribution revealed that flowback caused the mobilization of some solids. Solid mobilization depends on shear stresses generated by the flowing fluid and ϕ of solids. Using a numerical flow model it was demonstrated that solid mobilization has the potential to create high-permeability channels which may lead to significantly higher fracture permeability than a fracture filled with a uniform proppant distribution.

6.2 Future Work

The work presented in this dissertation investigated the behavior of concentrated suspensions flowing through parallel plate fractures. The complex behaviors and mechanisms observed give a better understanding of the flow behaviors of concentrated suspensions. However, some questions remain regarding the potential impact of normal stress differences of the carrier fluid on the suspension. It has been well documented that normal stress differences arising from the presence of particles in suspension are responsible for particle migrations. However, the effects of normal stress differences from the base fluid itself have not been investigated. Additionally, the experiments demonstrated particle-size-dependent migration in which large particles migrated from regions of higher shear to regions of lower shear (as expected) and smaller particles migrated from regions of lower shear to regions of higher shear (counter to the theoretically expected migration). This particle-dependent shear migration should be further explored. Understanding the role of normal stress differences from both particles and suspending fluid and size-dependent shear-driven migrations is important to understand the role the particle microstructure, i.e., spatial arrangement of suspended particles, has in the rheology and flow behavior of dense suspensions.

The multi-component (sand-fiber) proppant experiments demonstrated that adding fibers to sand proppants promotes the formation of a highly heterogeneous solid distribution which may lead to increased fracture permeability. Future sand-fiber experiments should be carried out in deforming fracture surfaces at higher applied normal stress. Applying a higher stress on a linear-elastic deforming fracture can help evaluate permeability changes due to proppant embedding into the fracture surface. Using a linear-elastic deforming fracture surface allows us to quantify the effect aperture reduction has on fracture permeability. That is, can evaluate the aperture reduction in the created *channels* and the effect this aperture reduction has on the fracture permeability. It should also be investigated how the separation distance between sand-fiber pillars and heterogeneous ϕ-distribution affects aperture reduction in the *channels*. The experiments presented here only considered smooth-walled parallel-plate fractures. Future experiments should consider the effects that long-wavelength and short-wavelength roughness variations on the fracture surface has on the on the solid distribution and the resulting fracture permeability.

Finally, mechanisms contributing to solid mobilization during flowback can be explored by numerical simulations of mobilization at the particle level. In the experiments presented in this work we observed that most solids were mobilized in the first flush, e.g. doubling or tripling the flow rate only had a small differential effect on solid mobilization. Though ϕ and $\dot{\gamma}$ appear to be adequate measures for solid mobilization, however, the effect of fibers was not explicitly accounted for. I hypothesize that fibers may increase the sand-fiber clumps resistance to erosion cause by shear. This should be investigated and can be modeled as a *reinforcement* or *cohesion* factor when modeling solid mobilization.

Bibliography

J. R. Abbott, N. Tetlow, A. L. Graham, S. A. Altobelli, Eiichi Fukushima, L. A. Mondy, and T. S. Stephens. Experimental observations of particle migration in concentrated suspensions: Couette flow. *Journal of Rheology*, 35(5):773–795, 1991. doi: 10.1122/1.550157.

MA Alves, PJ Oliveira, and FT Pinho. A convergent and universally bounded interpolation scheme for the treatment of advection. *International Journal for Numerical Methods in Fluids*, 41(1):47–75, JAN 10 2003. ISSN 0271-2091. doi: {10.1002/fld.428}.

J.L. Amundarain, L.J. Castro, M.R. Rojas, S. Siquier, N. Ramírez, A.J. Müller, and A.E. Sáez. Solutions of xanthan gum/guar gum mixtures: shear rheology, porous media flow, and solids transport in annular flow. *Rheologica Acta*, 48(5):491–498, 2009. ISSN 0035-4511. doi: 10.1007/s00397-008-0337-5.

T.E. Baldock, M.R. Tomkins, P. Nielsen, and M.G. Hughes. Settling velocity of sediments at high concentrations. *Coastal Engineering*, 51(1):91–100, 2004. ISSN 0378-3839. doi: 10.1016/j.coastaleng.2003.12.004.

Alexander C. Barbati, Jean Desroches, Agathe Robisson, and Gareth H. McKinley. Complex fluids and hydraulic fracturing. *Annual Review of Chemical and Biomolecular Engineering*, 7(1):415–453, 2016. doi: 10.1146/annurev-chembioeng-080615-033630.

G. K. Batchelor. The stress system in a suspension of force-free particles. *Journal of Fluid Mechanics*, 41:545–570, April 1970. ISSN 1469-7645. doi: 10.1017/S0022112070000745.

G. K. Batchelor and J. T. Green. The determination of the bulk stress in a suspension of spherical particles to order c2. *Journal of Fluid Mechanics*, 56:401–427, December 1972. ISSN 1469-7645. doi: 10.1017/S0022112072002435.

G.K. Batchelor. Sedimentation in a dilute dispersion of spheres. *Journal of Fluid Mechanics*, 52:245–268, 1972. doi: 10.1017/S0022112072001399.

LE Bayliss. The flow of suspensions of red blood cells in capillary tubes. changes in the'cell-free'marginal sheath with changes in the shearing stress. *The Journal of physiology*, 179 (1):1, 1965.

SH Bittleston, J Ferguson, and IA Frigaard. Mud removal and cement placement during primary cementing of an oil well - laminar non-newtonian displacements in an eccentric

annular hele-shaw cell. *Journal of Engineering Mathematics*, 43(2-4):229–253, August 2002. ISSN 0022-0833. doi: 10.1023/A:1020370417367.

Craig F Bohren and Donald R Huffman. *Absorption and scattering of light by small particles*. John Wiley & Sons, 2008.

C. Boschi, A. Dini, L. Dallai, G. Ruggieri, and G. Gianelli. Enhanced co2-mineral sequestration by cyclic hydraulic fracturing and si-rich fluid infiltration into serpentinites at malentrata (tuscany, italy). *Chemical Geology*, 265(1):209–226, 2009. ISSN 0009-2541. doi: 10.1016/j.chemgeo.2009.03.016.

Francois Boyer, Élisabeth Guazzelli, and Olivier Pouliquen. Unifying suspension and granular rheology. *Phys. Rev. Lett.*, 107:188301, October 2011a. doi: 10.1103/PhysRevLett.107.188301.

François Boyer, Olivier Pouliquen, and Élisabeth Guazzelli. Dense suspensions in rotating-rod flows: normal stresses and particle migration. *Journal of Fluid Mechanics*, 686:5–25, 2011b. doi: 10.1017/jfm.2011.272.

John F. Brady. The rheological behavior of concentrated colloidal dispersions. *The Journal of Chemical Physics*, 99(1):567–581, 1993. doi: 10.1063/1.465782.

John F. Brady and Jeffrey F. Morris. Microstructure of strongly sheared suspensions and its impact on rheology and diffusion. *Journal of Fluid Mechanics*, 348:103–139, October 1997. ISSN 1469-7645. doi: 10.1017/S0022112097006320.

Marina Nikolaevna Bulova, Ksenia Evgenievna Nosova, Dean Michael Willberg, and John T. Lassek. Benefits of the novel fiber-laden low-viscosity fluid system in fracturing low-permeability tight gas formations, January 2006. ISSN 978-1-55563-149-9.

RJ Card, PR Howard, JP Feraud, et al. A novel technology to control proppant backproduction. *SPE Production & Facilities*, 10(04):271–276, 1995.

Pierre J. Carreau. Rheological equations from molecular network theories. *Transactions of The Society of Rheology*, 16(1):99–127, 1972. doi: 10.1122/1.549276.

C Cassar, M Nicolas, and O Pouliquen. Submarine granular flows down inclined planes. *Physics of Fluids*, 17(10), OCT 2005. ISSN 1070-6631. doi: {10.1063/1.2069864}.

Chingyi Chang and Robert L. Powell. Dynamic simulation of bimodal suspensions of hydrodynamically interacting spherical particles. *Journal of Fluid Mechanics*, 253:1–25, 8 1993. ISSN 1469-7645. doi: 10.1017/S0022112093001697.

B.K. Chapman and D.T. Leighton Jr. Dynamic viscous resuspension. *International Journal of Multiphase Flow*, 17(4):469 – 483, 1991. ISSN 0301-9322. doi: 10.1016/0301-9322(91)90043-3.

R.P. Chhabra. *Bubbles, Drops, and Particles in Non-Newtonian Fluids, Second Edition*. Chemical Industries. CRC Press, 2nd edition, 2006. ISBN 9781420015386.

J. S. Chong, E. B. Christiansen, and A. D. Baer. Rheology of concentrated suspensions. *Journal of Applied Polymer Science*, 15(8):2007–2021, 1971. ISSN 1097-4628. doi: 10.1002/app.1971.070150818.

AW Chow, JH Iwayima, SW Sinton, and DT Leighton. Particle migration of non-brownian, concentrated suspensions in a truncated cone-and-plate. In *Society of Rheology Meeting, Sacramento, CA*, volume 103, 1995.

Gary D. Christian, Purnendu Dasgupta, and Kevin Schug. *Analytical chemistry*. John Wiley and Sons, Inc, Hoboken, NJ, 2014.

R. J. Chudzikowski. Guar gum and its applications. *Journal of the Society of Cosmetic Chemists*, 22(1):43–60, 1971.

JB Clark. A hydraulic process for increasing the productivity of wells. *Journal of Petroleum Technology*, 1(1):1–8, 1949.

Nilo Cesar Consoli, Michéle Dal Casagrande, and Matthew Richard Coop. Effect of fiber reinforcement on the isotropic compression behavior of a sand. *Journal of geotechnical and geoenvironmental engineering*, 131(11):1434–1436, 2005.

Benjamin Patrick Cook. *Lubrication models for particle-laden thin films*. ProQuest, 2007.

R G Cox and S G Mason. Suspended particles in fluid flow through tubes. *Annual Review of Fluid Mechanics*, 3(1):291–316, 1971. doi: 10.1146/annurev.fl.03.010171.001451.

Simon Dagois-Bohy, Sarah Hormozi, Élisabeth Guazzelli, and Olivier Pouliquen. Rheology of dense suspensions of non-colloidal spheres in yield-stress fluids. *Journal of Fluid Mechanics*, 776, 2015. doi: 10.1017/jfm.2015.329.

R H Davis and A Acrivos. Sedimentation of noncolloidal particles at low reynolds numbers. *Annual Review of Fluid Mechanics*, 17(1):91–118, 1985. doi: 10.1146/annurev.fl.17.010185.000515.

T. Dbouk, E. Lemaire, L. Lobry, and F. Moukalled. Shear-induced particle migration: Predictions from experimental evaluation of the particle stress tensor. *Journal of Non-Newtonian Fluid Mechanics*, 198(0):78 – 95, 2013. ISSN 0377-0257. doi: 10.1016/j.jnnfm.2013.03.006.

Talib Dbouk. *Rheology of concentrated suspensions and shear-induced migration*. PhD thesis, Citeseer, 2013.

Antonio Rodríguez de Castro and Giovanni Radilla. Non-darcian flow of shear-thinning fluids through packed beads: Experiments and predictions using forchheimer's law and ergun's equation. *Advances in Water Resources*, 100:35 – 47, 2017. ISSN 0309-1708. doi: 10.1016/j.advwatres.2016.12.009.

Wallace de Laguna. Disposal of radioactive wastes by hydraulic fracturing: Part i. general concept and first field experiments. *Nuclear Engineering and Design*, 3(2):338 – 352, 1966. ISSN 0029-5493. doi: 10.1016/0029-5493(66)90120-8.

Angélique Deboeuf, Georges Gauthier, Jérôme Martin, Yevgeny Yurkovetsky, and Jeffrey F. Morris. Particle pressure in a sheared suspension: A bridge from osmosis to granular dilatancy. *Phys. Rev. Lett.*, 102:108301, Mar 2009. doi: 10.1103/PhysRevLett.102.108301.

Russell L. Detwiler, Scott E. Pringle, and Robert J. Glass. Measurement of fracture aperture fields using transmitted light: An evaluation of measurement errors and their influence on simulations of flow and transport through a single fracture. *Water Resources Research*, 35 (9):2605–2617, 1999. ISSN 1944-7973. doi: 10.1029/1999WR900164.

V Di Federico. Estimates of equivalent aperture for non-Newtonian flow in a rough-walled fracture. *International Journal of Rock Mechanics and Mining Sciences*, 34(7):1133–1137, OCT 1997. ISSN 1365-1609. doi: {10.1016/S1365-1609(97)90205-7}.

A Diambra and E Ibraim. Fibre-reinforced sand: interaction at the fibre and grain scale. *Géotechnique*, 65(4):296–308, 2015.

A. Diambra, E. Ibraim, D. Muir Wood, and A.R. Russell. Fibre reinforced sands: Experiments and modelling. *Geotextiles and Geomembranes*, 28(3):238 – 250, 2010. ISSN 0266-1144. doi: 10.1016/j.geotexmem.2009.09.010.

A. Diambra, E. Ibraim, A. R. Russell, and D. Muir Wood. Fibre reinforced sands: from experiments to modelling and beyond. *International Journal for Numerical and Analytical Methods in Geomechanics*, 37(15):2427–2455, 2013. ISSN 1096-9853. doi: 10.1002/nag.2142.

DA Drew and RT Lahey. Analytical modeling of multiphase flow. *Particulate two-phase flow*, pages 509–566, 1993.

SC du Pont, P Gondret, B Perrin, and M Rabaud. Granular avalanches in fluids. *Physical Review Letters*, 90(4), JAN 31 2003. ISSN 0031-9007. doi: {10.1103/PhysRevLett.90.044301}.

Michael J Economides and Tony Martin. *Modern fracturing: Enhancing natural gas production*. ET Publishing Houston, Texas, 2007.

M.J. Economides and K.G. Nolte. *Reservoir Stimulation*. Prentice Hall, Englewood Cliffs, New Jersey, 2 edition, 2000. ISBN 9780471491927.

Ryan W. J. Edwards and Michael A. Celia. Shale gas well, hydraulic fracturing, and formation data to support modeling of gas and water flow in shale formations. *Water Resources Research*, Apr 2018. ISSN 0043-1397. doi: 10.1002/2017wr022130.

Albert Einstein. Eine neue bestimmung der moleküldimensionen. *Annalen der Physik*, 324 (2):289–306, 1906.

EA Ejofodomi, G Cavazzoli, J Morris, R Prioul, et al. Application of channel fracturing in the vaca muerta shale formation. In *SPE Latin America and Caribbean Petroleum Engineering Conference*. Society of Petroleum Engineers, 2014.

Hesham M. Eldesouky, Mohamed M. Morsy, and Mohamed F. Mansour. Fiber-reinforced sand strength and dilation characteristics. *Ain Shams Engineering Journal*, 7(2):517 – 526, 2016. ISSN 2090-4479. doi: 10.1016/j.asej.2015.06.003.

Rida Elgaddafi, Ramadan Ahmed, Matthew George, and Fred Growcock. Settling behavior of spherical particles in fiber-containing drilling fluids. *Journal of Petroleum Science and Engineering*, 84-85:20–28, 2012.

Rida Elgaddafi, Ramadan Ahmed, and Fred Growcock. Settling behavior of particles in fiber-containing herschel bulkley fluid. *Powder Technology*, 301:782 – 793, 2016. ISSN 0032-5910. doi: http://dx.doi.org/10.1016/j.powtec.2016.07.006.

JE Elkhoury, EE Brodsky, and DC Agnew. Seismic waves increase permeability. *Nature*, 441(7097):1135–1138, JUN 28 2006. ISSN 0028-0836. doi: {10.1038/nature04798}.

Jean E. Elkhoury, Andre Niemeijer, Emily E. Brodsky, and Chris Marone. Laboratory observations of permeability enhancement by fluid pressure oscillation of in situ fractured rock. *Journal of Geophysical Research: Solid Earth*, 116, FEB 24 2011. ISSN 2169-9313. doi: {10.1029/2010JB007759}.

J. Férec, M.C. Heuzey, G. Ausias, and P.J. Carreau. Rheological behavior of fiber-filled polymers under large amplitude oscillatory shear flow. *Journal of Non-Newtonian Fluid Mechanics*, 151(1–3):89 – 100, 2008. ISSN 0377-0257. doi: 10.1016/j.jnnfm.2008.01.002.

N. A. Frankel and Andreas Acrivos. The constitutive equation for a dilute emulsion. *Journal of Fluid Mechanics*, 44:65–78, 10 1970. ISSN 1469-7645. doi: 10.1017/S0022112070001696.

F. Gadala-Maria and A. Acrivos. Shear-induced structure in a concentrated suspension of solid spheres. *Journal of Rheology*, 24(6):799–814, 1980. doi: 10.1122/1.549584.

Chaiwut Gamonpilas, Jeffrey F. Morris, and Morton M. Denn. Shear and normal stress measurements in non-brownian monodisperse and bidisperse suspensions. *Journal of Rheology*, 60(2):289–296, 2016. doi: 10.1122/1.4942230.

S Garland, G Gauthier, J Martin, and JF Morris. Normal stress measurements in sheared non-brownian suspensions. *Journal of Rheology (1978-present)*, 57(1):71–88, 2013.

Matthew George, Ramadan Ahmed, and Fred Growcock. Rheological properties of fiber-containing drilling sweeps at ambient and elevated temperatures. In *Proceedings of the 2011 National Technical Conference and Exhibition - American Association of Drilling Engineers*, 2011.

Matthew George, Ramadan Ahmed, and Fred Growcock. Stability and flow behavior of fiber-containing drilling sweeps. In Juan De Vicente, editor, *Rheology*, chapter 9. INTECH Open Access Publisher, 2012.

Leonid N. Germanovich and Lawrence C. Murdoch. Injection of solids to lift coastal areas. *Proceedings of the Royal Society of London A: Mathematical, Physical and Engineering Sciences*, 466(2123):3225–3252, 2010. ISSN 1364-5021. doi: 10.1098/rspa.2010.0033.

Matthew Robert Gillard, Oleg O Medvedev, Paul R Hosein, Anatoly Medvedev, Fabio Peñacorada, Emmanuel d'Huteau, et al. A new approach to generating fracture conductivity. In *SPE Annual Technical Conference and Exhibition*. Society of Petroleum Engineers, 2010.

D.I. Graham and T.E.R. Jones. Settling and transport of spherical particles in power-law fluids at finite reynolds number. *Journal of Non-Newtonian Fluid Mechanics*, 54(0):465 – 488, 1994. ISSN 0377-0257. doi: 10.1016/0377-0257(94)80037-5.

Al Granberg. What is hydraulic fracturing?, 2008. URL `https://www.propublica.org/article/hydraulic-fracturing-national`.

Élisabeth Guazzelli and John Hinch. Fluctuations and instability in sedimentation. *Annual Review of Fluid Mechanics*, 43(1):97–116, 2011. doi: 10.1146/annurev-fluid-122109-160736.

Jianchun Guo, Jian Ma, Zhihong Zhao, and Yang Gao. Effect of fiber on the rheological property of fracturing fluid. *Journal of Natural Gas Science and Engineering*, 23(0):356 – 362, 2015. ISSN 1875-5100. doi: 10.1016/j.jngse.2015.02.017.

Rong Guo, Jalel Azaiez, and Celine Bellehumeur. Rheology of fiber filled polymer melts: Role of fiber-fiber interactions and polymer-fiber coupling. *Polymer Engineering & Science*, 45 (3):385–399, 2005. ISSN 1548-2634. doi: 10.1002/pen.20285.

Tiankui Guo, Shicheng Zhang, Zhanqing Qu, Tong Zhou, Yongshun Xiao, and Jun Gao. Experimental study of hydraulic fracturing for shale by stimulated reservoir volume. *Fuel*, 128(0):373 – 380, 2014. ISSN 0016-2361. doi: 10.1016/j.fuel.2014.03.029.

T.K. Guo, S.C. Zhang, B. Xiao, G.Q. Liu, F. Wang, J.C. Zhang, and X.B. Bian. Evaluation and optimization of new nanocomposite fiber for fracturing technology based on a new equipment. *Transport in Porous Media*, 94(1):243–257, 2012. ISSN 0169-3913. doi: 10.1007/s11242-012-0002-4.

R. E. Hampton, A. A. Mammoli, A. L. Graham, N. Tetlow, and S. A. Altobelli. Migration of particles undergoing pressure-driven flow in a circular conduit. *Journal of Rheology*, 41 (3):621–640, 1997. doi: 10.1122/1.550863.

J. Happel and E. Bart. The settling of a sphere along the axis of a long square duct at low reynolds' number. *Applied Scientific Research*, 29(1):241–258, 1974. ISSN 0003-6994. doi: 10.1007/BF00384149.

Oliver G. Harlen, R. R. Sundararajakumar, and Donald L. Koch. Numerical simulations of a sphere settling through a suspension of neutrally buoyant fibres. *Journal of Fluid Mechanics*, 388:355–388, 6 1999. ISSN 1469-7645. doi: 10.1017/S0022112099004929.

Francis H Harlow. The particle-in-cell computing method for fluid dynamics. *Methods Comput. Phys.*, 3:319–343, 1964.

M. D. Haw. Jamming, two-fluid behavior, and "self-filtration" in concentrated particulate suspensions. *Phys. Rev. Lett.*, 92:185506, May 2004. doi: 10.1103/PhysRevLett.92.185506.

R Herczynski and I Pienkowska. Toward a statistical theory of suspension. *Annual Review of Fluid Mechanics*, 12(1):237–269, 1980. doi: 10.1146/annurev.fl.12.010180.001321.

Benjamin Herzhaft and Élisabeth Guazzelli. Experimental study of the sedimentation of dilute and semi-dilute suspensions of fibres. *Journal of Fluid Mechanics*, 384:133–158, 1999.

Benjamin Herzhaft, Élisabeth Guazzelli, Michael B. Mackaplow, and Eric S. G. Shaqfeh. Experimental investigation of the sedimentation of a dilute fiber suspension. *Phys. Rev. Lett.*, 77:290–293, Jul 1996. doi: 10.1103/PhysRevLett.77.290.

Bing Hou, Xiaojin Zheng, Mian Chen, Zhihui Ye, and Dong Chen. Parameter simulation and optimization in channel fracturing. *Journal of Natural Gas Science and Engineering*, 35, Part A:122 – 130, 2016. ISSN 1875-5100. doi: 10.1016/j.jngse.2016.08.046.

Tengfei Hou, Shicheng Zhang, Xinfang Ma, Junjie Shao, Yunan He, Xinrun Lv, and Jingyu Han. Experimental and theoretical study of fracture conductivity with heterogeneous proppant placement. *Journal of Natural Gas Science and Engineering*, 37:449 – 461, 2017. ISSN 1875-5100. doi: 10.1016/j.jngse.2016.11.059.

PR Howard, SG James, David Milton-Tayler, et al. High permeability channels in proppant packs containing random fibers. In *SPE Formation Damage Control Conference*. Society of Petroleum Engineers, 1999.

Mads Huuse, Christopher A. L. Jackson, Pieter Van Rensbergen, Richard J. Davies, Peter B. Flemings, and Richard J. Dixon. Subsurface sediment remobilization and fluid flow in sedimentary basins: an overview. *Basin Research*, 22(4):342–360, AUG 2010. ISSN 0950-091X. doi: {10.1111/j.1365-2117.2010.00488.x}.

Lukasz Jasinski and Marcin Dabrowski. The effective transmissivity of a plane-walled fracture with circular cylindrical obstacles. *Journal of Geophysical Research: Solid Earth*, 123 (1):242–263, Jan 2018. ISSN 2169-9313. doi: 10.1002/2017jb014509.

A. Karnis, H.L. Goldsmith, and S.G. Mason. The kinetics of flowing dispersions: I. concentrated suspensions of rigid particles. *Journal of Colloid and Interface Science*, 22(6):531 – 553, 1966. ISSN 0021-9797. doi: 10.1016/0021-9797(66)90048-8.

T. Katsaga, A. Riahi, D. O. DeGagne, B. Valley, and B. Damjanac. Hydraulic fracturing operations in mining: conceptual approach and dfn modeling example. *Mining Technology*, 124(4):255–266, 2015. doi: 10.1179/1743286315Y.0000000022.

D.R. Kaushal, Kimihiko Sato, Takeshi Toyota, Katsuya Funatsu, and Yuji Tomita. Effect of particle size distribution on pressure drop and concentration profile in pipeline flow of highly concentrated slurry. *International Journal of Multiphase Flow*, 31(7):809 – 823, 2005. ISSN 0301-9322. doi: 10.1016/j.ijmultiphaseflow.2005.03.003.

LR Kern, TK Perkins, and RE Wyant. The mechanics of sand movement in fracturing. *Transactions of the American Institute of Mining and Metallurgical Engineers*, 216:403–405, 1959.

Subramanian Kesavan and Robert K Prud'Homme. Rheology of guar and (hydroxypropyl) guar crosslinked by borate. *Macromolecules*, 25(7):2026–2032, 1992.

Kartic C Khilar and H Scott Fogler. *Migrations of fines in porous media*, volume 12. Springer Science & Business Media, 1998.

Jihoon Kim and George J. Moridis. Numerical analysis of fracture propagation during hydraulic fracturing operations in shale gas systems. *International Journal of Rock Mechanics and Mining Sciences*, 76(0):127 – 137, 2015. ISSN 1365-1609. doi: 10.1016/j.ijrmms.2015.02.013.

Christopher J Koh, Philip Hookham, and LG Leal. An experimental investigation of concentrated suspension flows in a rectangular channel. *Journal of Fluid Mechanics*, 266(1): 1–32, 1994.

Douglas B Kothe and William J Rider. A comparison of interface tracking methods. Technical report, Los Alamos National Lab., NM (United States), 1995.

Irvin M. Krieger and Thomas J. Dougherty. A mechanism for non-newtonian flow in suspensions of rigid spheres. *Transactions of The Society of Rheology (1957-1977)*, 3(1):137–152, 1959. doi: 10.1122/1.548848.

Gokul P. Krishnan, Shannon Beimfohr, and David T. Leighton. Shear-induced radial segregation in bidisperse suspensions. *Journal of Fluid Mechanics*, 321:371–393, 8 1996. ISSN 1469-7645. doi: 10.1017/S0022112096007768.

Brice Lecampion and Dmitry I. Garagash. Confined flow of suspensions modelled by a frictional rheology. *Journal of Fluid Mechanics*, 759:197–235, 11 2014. ISSN 1469-7645. doi: 10.1017/jfm.2014.557.

B. Legarth, E. Huenges, and G. Zimmermann. Hydraulic fracturing in a sedimentary geothermal reservoir: Results and implications. *International Journal of Rock Mechanics and Mining Sciences*, 42(7):1028 – 1041, 2005. ISSN 1365-1609. doi: 10.1016/j.ijrmms.2005.05.014.

Cuiyue Lei and Peter. E. Clark. Crosslinking of guar and guar derivatives. In *SPE Annual Technical Conference and Exhibition*. Society of Petroleum Engineers, 2004.

Cuiyue Lei and Peter. E. Clark. Crosslinking of guar and guar derivatives. 12(3):316–321, 2007. doi: 10.2118/90840-PA.

David Leighton and Andreas Acrivos. Viscous resuspension. *Chemical Engineering Science*, 41(6):1377 – 1384, 1986. ISSN 0009-2509. doi: 10.1016/0009-2509(86)85225-3.

David Leighton and Andreas Acrivos. Measurement of shear-induced self-diffusion in concentrated suspensions of spheres. *Journal of Fluid Mechanics*, 177:109–131, 4 1987a. ISSN 1469-7645. doi: 10.1017/S0022112087000880.

David Leighton and Andreas Acrivos. The shear-induced migration of particles in concentrated suspensions. *Journal of Fluid Mechanics*, 181:415–439, 9 1987b. ISSN 1469-7645. doi: 10.1017/S0022112087002155.

Tianbo Liang, Fujian Zhou, Yang Shi, Xiongfei Liu, Rui Wang, Ben Li, and Xiuhui Li. Evaluation and optimization of degradable-fiber-assisted slurry for fracturing thick and tight formation with high stress. *Journal of Petroleum Science and Engineering*, 165:81 – 89, 2018. ISSN 0920-4105. doi: 10.1016/j.petrol.2018.02.010.

Yuan Lin, Nhan Phan-Thien, and Boo Cheong Khoo. Polymeric suspensions in shear flow: Relaxation and normal stress differences. *Journal of Non-Newtonian Fluid Mechanics*, 239:28 – 34, 2017. ISSN 0377-0257. doi: 10.1016/j.jnnfm.2016.12.005.

Yajun Liu and Mukul M. Sharma. Effect of fracture width and fluid rheology on proppant settling and retardation: An experimental study. Society of Petroleum Engineers, 2005.

M. K. Lyon and L. G. Leal. An experimental study of the motion of concentrated suspensions in two-dimensional channel flow. Part 2. bidisperse systems. *Journal of Fluid Mechanics*, 363:57–77, 5 1998a. ISSN 1469-7645. doi: 10.1017/S0022112098008817.

M. K. Lyon and L. G. Leal. An experimental study of the motion of concentrated suspensions in two-dimensional channel flow. Part 1. Monodisperse systems. *Journal of Fluid Mechanics*, 363:25–56, 5 1998b. ISSN 1469-7645. doi: 10.1017/S0022112098008817.

H.M. Mader, E.W. Llewellin, and S.P. Mueller. The rheology of two-phase magmas: A review and analysis. *Journal of Volcanology and Geothermal Research*, 257(0):135 – 158, 2013. ISSN 0377-0273. doi: 10.1016/j.jvolgeores.2013.02.014.

Michael Manga and Emily Brodsky. Seismic triggering of eruptions in the far field: Volcanoes and geysers. *Annual Review of Earth and Planetary Sciences*, 34:263–291, 2006. ISSN 0084-6597. doi: 10.1146/annurev.earth.34.031405.125125.

Samuel H. Maron and Percy E. Pierce. Application of ree-eyring generalized flow theory to suspensions of spherical particles. *Journal of Colloid Science*, 11(1):80 – 95, 1956. ISSN 0095-8522. doi: 10.1016/0095-8522(56)90023-X.

R. Medina, J. E. Elkhoury, J. P. Morris, R. Prioul, J. Desroches, and R. L. Detwiler. Flow of concentrated suspensions through fractures: small variations in solid concentration cause significant in-plane velocity variations. *Geofluids*, 15(1-2):24–36, 2015. ISSN 1468-8123. doi: 10.1111/gfl.12109.

R. Medina, J. E. Elkhoury, J. P. Morris, R. Prioul, J. Desroches, and R. L. Detwiler. *Flow of concentrated suspensions through fractures: small variations in solid concentration cause significant in-plane velocity variations*, chapter 5. Wiley-Blackwell, 2016. ISBN 978-1-119-16656-6.

Anatoly Vladimirovich Medvedev, Chad Christopher Kraemer, Alejandro Andres Pena, and Mohan Kanaka Raju Panga. On the mechanisms of channel fracturing, February 2013. ISSN 978-1-61399-252-4.

Bloen Metzger, Elisabeth Guazzelli, and Jason E Butler. Large-scale streamers in the sedimentation of a dilute fiber suspension. *Physical review letters*, 95(16):164506, 2005.

Bloen Metzger, Jason E. Butler, and Élisabeth Guazzelli. Experimental investigation of the instability of a sedimenting suspension of fibres. *Journal of Fluid Mechanics*, 575:307–332, 003 2007. doi: 10.1017/S0022112006004460.

A. B. Metzner. Rheology of suspensions in polymeric liquids. *Journal of Rheology*, 29(6): 739–775, 1985. doi: 10.1122/1.549808.

Ryan M. Miller and Jeffrey F. Morris. Normal stress-driven migration and axial development in pressure-driven flow of concentrated suspensions. *Journal of Non-Newtonian Fluid Mechanics*, 135(2–3):149 – 165, 2006. ISSN 0377-0257. doi: 10.1016/j.jnnfm.2005.11.009.

William J. Milliken, Moshe Gottlieb, Alan L. Graham, Lisa A. Mondy, and Robert L. Powell. The viscosity-volume fraction relation for suspensions of rod-like particles by falling-ball rheometry. *Journal of Fluid Mechanics*, 202:217–232, 5 1989. ISSN 1469-7645. doi: 10.1017/S0022112089001163.

Hadi Mohammadigoushki and James J. Feng. Size segregation in sheared two-dimensional polydisperse foam. *Langmuir*, 29(5):1370–1378, 2013. doi: 10.1021/la304445f.

J.J. Monaghan. Smoothed particle hydrodynamics and its diverse applications. *Annual Review of Fluid Mechanics*, 44(1):323–346, 2012. doi: 10.1146/annurev-fluid-120710-101220.

Carl Montgomery. Fracturing fluids. In Andrew P. Bunger, John McLennan, and Rob Jeffrey, editors, *Effective and Sustainable Hydraulic Fracturing*, chapter 01. InTech, Rijeka, 2013. doi: 10.5772/56192.

J. P. Morris, N. Chugunov, and G. Meouchy. Understanding heterogeneously propped hydraulic fractures through combined fluid mechanics, geomechanics, and statistical analysis, August 2014. ISSN 978-0-9894844-1-1.

Jeffrey F. Morris and Fabienne Boulay. Curvilinear flows of noncolloidal suspensions: The role of normal stresses. *Journal of Rheology*, 43(5):1213–1237, 1999. doi: 10.1122/1.551021.

JP Morris and JJ Monaghan. A switch to reduce SPH viscosity. *Journal of Computational Physics*, 136(1):41–50, SEP 1 1997. ISSN 0021-9991. doi: {10.1006/jcph.1997.5690}.

Deepak Mudgil, Sheweta Barak, and Bhupendar Singh Khatkar. Guar gum: processing, properties and food applications-a review. *Journal of food science and technology*, 51(3): 409–418, 2014.

S. Mueller, E. W. Llewellin, and H. M. Mader. The rheology of suspensions of solid particles. *Proceedings of the Royal Society A: Mathematical, Physical and Engineering Science*, 2009. doi: 10.1098/rspa.2009.0445.

Larry Murdoch. *Alternative methods for fluid delivery and recovery*. DIANE Publishing, 1995.

Lawrence C. Murdoch, James R. Richardson, Qingfeng Tan, Shaun C. Malin, and Cedric Fairbanks. Forms and sand transport in shallow hydraulic fractures in residual soil. *Canadian Geotechnical Journal*, 43(10):1061–1073, Oct 2006. ISSN 0008-3674. doi: {10.1139/T06-063}.

H. Nicolai, B. Herzhaft, E. J. Hinch, L. Oger, and E. Guazzelli. Particle velocity fluctuations and hydrodynamic self-diffusion of sedimenting non-brownian spheres. *Physics of Fluids*, 7(1):12–23, 1995. doi: 10.1063/1.868733.

Prabhu R. Nott and John F. Brady. Pressure-driven flow of suspensions: simulation and theory. *Journal of Fluid Mechanics*, 275:157–199, 9 1994. ISSN 1469-7645. doi: 10.1017/S0022112094002326.

Sangwon Oh, Yi-qiao Song, Dmitry I. Garagash, Brice Lecampion, and Jean Desroches. Pressure-driven suspension flow near jamming. *Phys. Rev. Lett.*, 114:088301, Feb 2015. doi: 10.1103/PhysRevLett.114.088301.

George Y. Onoda and Eric G. Liniger. Random loose packings of uniform spheres and the dilatancy onset. *Phys. Rev. Lett.*, 64:2727–2730, May 1990. doi: 10.1103/PhysRevLett.64.2727.

Andrei A. Osiptsov. Fluid mechanics of hydraulic fracturing: a review. *Journal of Petroleum Science and Engineering*, 156:513 – 535, 2017. ISSN 0920-4105. doi: 10.1016/j.petrol.2017.05.019.

Rajinder Pal. Rheology of suspensions of solid particles in power-law fluids. *The Canadian Journal of Chemical Engineering*, 93(1):166–173, 2015. ISSN 1939-019X. doi: 10.1002/cjce.22114.

J.R.A. Pearson. On suspension transport in a fracture: framework for a global model. *Journal of Non-Newtonian Fluid Mechanics*, 54(0):503 – 513, 1994. ISSN 0377-0257. doi: 10.1016/0377-0257(94)80039-1.

"R.M. Perez, S. Siquier, N. Ramirez, A.J. Muller, and A.E. Saez". Non-newtonian annular vertical flow of sand suspensions in aqueous solutions of guar gum. *Journal of Petroleum Science and Engineering*, 44(3–4):317 – 331, 2004. ISSN 0920-4105. doi: 10.1016/j.petrol.2004.03.006.

Ronald J. Phillips, Robert C. Armstrong, Robert A. Brown, Alan L. Graham, and James R. Abbott. A constitutive equation for concentrated suspensions that accounts for shear-induced particle migration. *Physics of Fluids A*, 4(1):30–40, 1992. doi: 10.1063/1.858498.

Luis Felipe Miranda Pino and Béatrice Anne Baudet. The effect of the particle size distribution on the mechanics of fibre-reinforced sands under one-dimensional compression. *Geotextiles and Geomembranes*, 43(3):250 – 258, 2015. ISSN 0266-1144. doi: 10.1016/j.geotexmem.2015.02.004.

Dmitriy Ivanovich Potapenko, Leland Ramsey, Timothy M Lesko, Dean M Willberg, Theodore Lafferty, and John W Still. Compositions and methods for increasing fracture conductivity, 2014.

Dmitriy Ivanovich Potapenko, J Ernest Brown, Partha Ganguly, Andrey Bogdan, and Leland Ramsey. In situ channelization method and system for increasing fracture conductivity, 2016.

Arun Kumar Pradhan, Dipayan Das, R. Chattopadhyay, and S.N. Singh. Effect of 3d fiber orientation distribution on particle capture efficiency of anisotropic fiber networks. *Powder Technology*, 249(0):205 – 207, 2013. ISSN 0032-5910. doi: 10.1016/j.powtec.2013.08.011.

D. Quemada. Rheology of concentrated disperse systems and minimum energy dissipation principle. *Rheologica Acta*, 16(1):82–94, 1977. ISSN 1435-1528. doi: 10.1007/BF01516932.

Mahmoud Rajabian, Charles Dubois, Miroslav Grmela, and PierreJ. Carreau. Effects of polymer–fiber interactions on rheology and flow behavior of suspensions of semi-flexible fibers in polymeric liquids. *Rheologica Acta*, 47(7):701–717, 2008.

Mallela Mallikarjuna Reddy and Anugrah Singh. Flow of concentrated suspension through oblique bifurcating channels. *AIChE Journal*, 60(7):2692–2704, 2014. ISSN 1547-5905. doi: 10.1002/aic.14446.

J.F. Richardson and W.N. Zaki. Sedimentation and fluidisation: Part i. *Transactions of the Institution of Chemical Engineers*, 32:35–53, 1954. ISSN 0263-8762. doi: 10.1016/S0263-8762(97)80006-8.

David Saintillan, Eric Darve, and Eric S. G. Shaqfeh. A smooth particle-mesh ewald algorithm for stokes suspension simulations: The sedimentation of fibers. *Physics of Fluids*, 17(3):033301, 2005. doi: 10.1063/1.1862262.

Erik Santiso and Erich A. Müller. Dense packing of binary and polydisperse hard spheres. *Molecular Physics*, 100(15):2461–2469, 2002. doi: 10.1080/00268970210125313.

Christian F. Schmid and Daniel J. Klingenberg. Properties of fiber flocs with frictional and attractive interfiber forces. *Journal of Colloid and Interface Science*, 226(1):136 – 144, 2000a. ISSN 0021-9797. doi: 10.1006/jcis.2000.6803.

Christian F Schmid and Daniel J Klingenberg. Mechanical flocculation in flowing fiber suspensions. *Physical review letters*, 84(2):290, 2000b.

Christian F. Schmid, Leonard H. Switzer, and Daniel J. Klingenberg. Simulations of fiber flocculation: Effects of fiber properties and interfiber friction. *Journal of Rheology*, 44(4):781–809, 2000. doi: 10.1122/1.551116.

Andrew P. Shapiro and Ronald F. Probstein. Random packings of spheres and fluidity limits of monodisperse and bidisperse suspensions. *Phys. Rev. Lett.*, 68:1422–1425, Mar 1992. doi: 10.1103/PhysRevLett.68.1422.

Sogo Shiozawa and Mark McClure. Simulation of proppant transport with gravitational settling and fracture closure in a three-dimensional hydraulic fracturing simulator. *Journal of Petroleum Science and Engineering*, 138:298 – 314, 2016. ISSN 0920-4105. doi: 10.1016/j.petrol.2016.01.002.

Dennis A Siginer. *Developments in the Flow of Complex Fluids in Tubes*. Springer, 2015.

Michelle E. Staben, Alexander Z. Zinchenko, and Robert H. Davis. Motion of a particle between two parallel plane walls in low-reynolds-number poiseuille flow. *Physics of Fluids (1994-present)*, 15(6):1711–1733, 2003. doi: 10.1063/1.1568341.

Jonathan J Stickel and Robert L Powell. Fluid mechanics and rheology of dense suspensions. *Annu. Rev. Fluid Mech.*, 37:129–149, 2005.

M Sussman, P Smereka, and S Osher. A Level Set Aapproach for Comptuting Solutions to Incompressible 2-Phase Flow. *Journal of Computational Physics*, 114(1):146–159, SEP 1994. ISSN 0021-9991. doi: {10.1006/jcph.1994.1155}.

Leonard H. Switzer and Daniel J. Klingenberg. Flocculation in simulations of sheared fiber suspensions. *International Journal of Multiphase Flow*, 30(1):67 – 87, 2004. ISSN 0301-9322. doi: 10.1016/j.ijmultiphaseflow.2003.10.005.

Leonard H Switzer III and Daniel J Klingenberg. Rheology of sheared flexible fiber suspensions via fiber-level simulations. *Journal of Rheology (1978-present)*, 47(3):759–778, 2003.

Chaosheng Tang, Bin Shi, Wei Gao, Fengjun Chen, and Yi Cai. Strength and mechanical behavior of short polypropylene fiber reinforced and cement stabilized clayey soil. *Geotextiles and Geomembranes*, 25(3):194 – 202, 2007. ISSN 0266-1144. doi: 10.1016/j.geotexmem.2006.11.002.

W. Thielicke and E. Stamhuis. Pivlab - time-resolved digital particle image velocimetry tool for matlab, 2012.

M.D. Torres, B. Hallmark, and D.I. Wilson. Effect of concentration on shear and extensional rheology of guar gum solutions. *Food Hydrocolloids*, 40:85 – 95, 2014. ISSN 0268-005X. doi: 10.1016/j.foodhyd.2014.02.011.

Tiziana Tosco, Daniele L. Marchisio, Federica Lince, and Rajandrea Sethi. Extension of the darcy–forchheimer law for shear-thinning fluids and validation via pore-scale flow simulations. *Transport in Porous Media*, 96(1):1–20, 2013. ISSN 1573-1634. doi: 10.1007/s11242-012-0070-5.

U.S.EPA. Hydraulic fracturing for oil and gas: Impacts from the hydraulic fracturing water cycle on drinking water resources in the united states. Technical report, United States Environmental Protection Agency. Office of Research and Development, Washington, DC, December 2016.

S. Vasudevan, D. M. Willberg, J. A. Wise, T. L. Gorham, R. C. Dacar, P. F. Sullivan, C. L. Boney, and F. Mueller. Field test of a novel low viscosity fracturing fluid in the lost hills field, california, January 2001. ISSN 978-1-55563-931-0.

Henk Kaarle Versteeg and Weeratunge Malalasekera. *An introduction to computational fluid dynamics: the finite volume method*. Pearson Education, 2007.

D. M. Willberg, M. J. Miller, M. J. Thiercelin, and I. V. Kosarev. Method for hydraulic fracturing of subterranean formation, 2011.

P. A. Witherspoon, J. S. Y. Wang, K. Iwai, and J. E. Gale. Validity of cubic law for fluid flow in a deformable rock fracture. *Water Resources Research*, 16(6):1016–1024, 1980. ISSN 1944-7973. doi: 10.1029/WR016i006p01016.

Ron CK Wong and Marolo C Alfaro. Fracturing in low-permeability soils for remediation of contaminated ground. *Canadian Geotechnical Journal*, 38(2):316–327, 2001.

J.-Z. Xue, E. Herbolzheimer, M. A. Rutgers, W. B. Russel, and P. M. Chaikin. Diffusion, dispersion, and settling of hard spheres. *Phys. Rev. Lett.*, 69:1715–1718, Sep 1992. doi: 10.1103/PhysRevLett.69.1715.

S. Yadav, M. Mallikarjuna Reddy, and Anugrah Singh. Shear-induced particle migration in three-dimensional bifurcation channel. *International Journal of Multiphase Flow*, 76:1 – 12, 2015. ISSN 0301-9322. doi: 10.1016/j.ijmultiphaseflow.2015.06.007.

Yingtao Yang and Qingzhi Wen. Numerical simulation of gas-liquid two-phase flow in channel fracture pack. *Journal of Natural Gas Science and Engineering*, 43:33 – 47, 2017. ISSN 1875-5100. doi: 10.1016/j.jngse.2017.03.024.

Ching H. Yew and Xiaowei Weng. *Mechanics of Hydraulic Fracturing*. Gulf Professional Publishing, Boston, second edition edition, 2015. ISBN 978-0-12-420003-6. doi: 10.1016/B978-0-12-420003-6.09994-8.

David L Youngs. An interface tracking method for a 3d eulerian hydrodynamics code. *Atomic Weapons Research Establishment (AWRE) Technical Report*, (44/92):35, 1984.

Isidro E. Zarraga, Davide A. Hill, and David T. Leighton Jr. The characterization of the total stress of concentrated suspensions of noncolloidal spheres in newtonian fluids. *Journal of Rheology*, 44(2):185–220, 2000. doi: 10.1122/1.551083.

Xiaojin Zheng, Mian Chen, Bing Hou, Zhihui Ye, Wei Wang, Congbin Yin, and Xingyu Chen. Effect of proppant distribution pattern on fracture conductivity and permeability in channel fracturing. *Journal of Petroleum Science and Engineering*, 149:98 – 106, 2017. ISSN 0920-4105. doi: 10.1016/j.petrol.2016.10.023.

Appendix A

Numerical simulations of concentrated suspensions

Numerical simulations of concentrated suspensions were carried out using a modified version of the suspension balance model (SBM) developed by Dbouk et al. (2013). We modified the source code to include the gravity terms and a shear-dependent fluid viscosity. The model was developed for the open-source CFD software OpenFOAM®.

The balance equations in the SBM were developed by averaging the mass and momentum conservation equations over the suspension (fluid and particle phases) and particle phase, which is treated as a continuum, following an averaging procedure similar to that proposed by Drew and Lahey (1993). This leads to the suspension mass and momentum balances given by

$$\nabla \cdot \mathbf{U} = 0 \tag{A.1}$$

$$\nabla \cdot \mathbf{\Sigma} + \langle \rho \rangle \mathbf{b} = 0 \tag{A.2}$$

where $\mathbf{U}$ is the bulk suspension velocity, $\mathbf{\Sigma}$ is the bulk suspension stress, and $\langle\rho\rangle\mathbf{b}$ is the mean gravity force. The particle phase mass balance is given by

$$\frac{\partial\phi}{\partial t} + \mathbf{U}\cdot\nabla\phi = -\nabla\cdot\mathbf{j} \tag{A.3}$$

where $\mathbf{j} = \phi(\mathbf{U_p} - \mathbf{U})$ is the particle migration flux relative to the bulk motion, here $\mathbf{U_p}$ is the particle phase velocity. The migration flux is determined from particle momentum balance, which includes hydrodynamic drag forces acting on the particle phase. Therefore, the particle migration flux is given by

$$\mathbf{j} = \frac{2a^2}{9\eta_f} f(\phi)[\nabla\cdot\Sigma^p + \phi\Delta\rho g] \tag{A.4}$$

which depends on the divergence of the particle stress Σ^p and the bouyancy-corrected body forces acting on the particles (Cook, 2007). Where the hindrance function, $f(\phi)$, represents the mobility of the particle phase. We used the hindrance function of the form (Miller and Morris, 2006):

$$f(\phi) = (1 - \phi/\phi_m)(1-\phi)^{\alpha-1} \tag{A.5}$$

with $\alpha = 5.1$. The first term of the hindrance function is necessary to ensure particle migration stops when the concentration reaches ϕ_m (Miller and Morris, 2006). The second term of the hindrance function has the same form as the classical Richardson-Zaki equation $f(\phi) = (1-\phi)^\beta$ (Richardson and Zaki, 1954). The full particle transport equation is then given by:

$$\frac{\partial \phi}{\partial t} + \mathbf{U} \cdot \nabla \phi = -\nabla \cdot \left[\frac{2a^2}{9\eta_f} f(\phi) \left(\nabla \cdot \Sigma^p + \phi \Delta \rho g \right) \right] \tag{A.6}$$

The suspension stress is the sum of the fluid stress and the particle stress, $\mathbf{\Sigma} = \mathbf{\Sigma}^f + \mathbf{\Sigma}^p$. The fluid stress is defined as

$$\mathbf{\Sigma}^f = -P_f \mathbf{I} + 2\eta_f \mathbf{E} \tag{A.7}$$

where P_f is the fluid phase pressure, $\mathbf{I}$ is the identity tensor, η_f is the carrier fluid viscosity, and $\mathbf{E} = \frac{1}{2}[\nabla \cdot \mathbf{U} + (\nabla \cdot \mathbf{U})^T]$ is the local rate of strain. The particle phase stress tensor is given by

$$\mathbf{\Sigma}^p = -\eta_f \eta_N(\phi) \dot{\gamma} \mathbf{Q} + 2\eta_f \eta_P(\phi) \mathbf{E} \tag{A.8}$$

where $\mathbf{Q}$ is a tensor to represent normal stress differences in the suspension. The first term in Equation A.8 represents the normal viscosity component and the second term is the contribution of the shear viscosity. The suspension $\eta_s(\phi)$, normal $\eta_N(\phi)$, and shear $\eta_P(\phi)$ viscosities, respectively, are given by (Miller and Morris, 2006; Morris and Boulay, 1999; Dbouk et al., 2013):

$$\eta_s(\phi) = \eta_f \left(1 - \frac{\phi}{\phi_m} \right)^{-2} \tag{A.9}$$

$$\eta_N(\phi) = \eta_f K_n \left(\frac{\phi}{\phi_m} \right)^2 \left(1 - \frac{\phi}{\phi_m} \right)^{-2} \tag{A.10}$$

$$\eta_P(\phi) = \eta_s(\phi) - \eta_f \tag{A.11}$$

where η_f is the suspending fluid viscosity, K_n is a fitting parameter of $\mathcal{O}(1)$, and ϕ_m is the maximum solid volume fraction. We assume $K_n = 0.75$, a value found to agree with rheology measurements in wide-gap Couette (Morris and Boulay, 1999).

Equations A.9-A.11 assume the carrier fluid is Newtonian with constant η_f. We modified the source code to include a shear-depended fluid viscosity modeled by the Cross-power law model given by:

$$\eta_f(\dot{\gamma}) = \frac{\eta_0 - \eta_\infty}{1 + (m\dot{\gamma})^n} + \eta_\infty \tag{A.12}$$

where m is the fluid relaxation time, n is the power-law index, and η_0 and η_∞ are the fluid viscosity at zero and infinite shear-rate, respectively (Chhabra, 2006). We measured the viscosity of a 0.75% guar-water mixture for shear rates in the range $\dot{\gamma} = 0.01 - 1000$ sec^{-1}. Using a least squares fit, we estimated the fitting parameters for Eq. A.12 as: $m = 0.534$ s, $n = 0.833$, $\eta_0 = 6.844$ Pa·s, and $\eta_\infty = 0.01$ Pa·s. The shear rate, calculated at every step as $\dot{\gamma} = \sqrt{2\mathbf{E} : \mathbf{E}}$, is used to calculate the shear-dependent fluid viscosity, $\eta_f(\dot{\gamma})$, at every element in the domain. This shear-dependent fluid viscosity is used in all necessary equations. As previously noted, normal stress differences due to the suspended particles are the driving mechanism for cross-flow particle transport. Though, guar solutions have been observed to exhibit normal stress differences, these normal stress differences are negligible at low shear rates, $\dot{\gamma} \lesssim 10$ s^{-1} (Lin et al., 2017). Our experimental and simulated velocities were in the rage $\bar{u} = 2.6 \times 10^{-4} - 8.6 \times 10^{-6}$ m/s, resulting in approximate range of shear rates in the range $\dot{\gamma} = 7.6 \times 10^{-3} - 0.23$ s^{-1}. Therefore, we assume normal stress differences from the fluid are negligible and do not contribute to the particle shear-induced normal stress differences. The momentum and continuity equations are solved using the SIMPLE algorithm (Versteeg and Malalasekera, 2007) Particle transport is then calculated by Equation A.6.

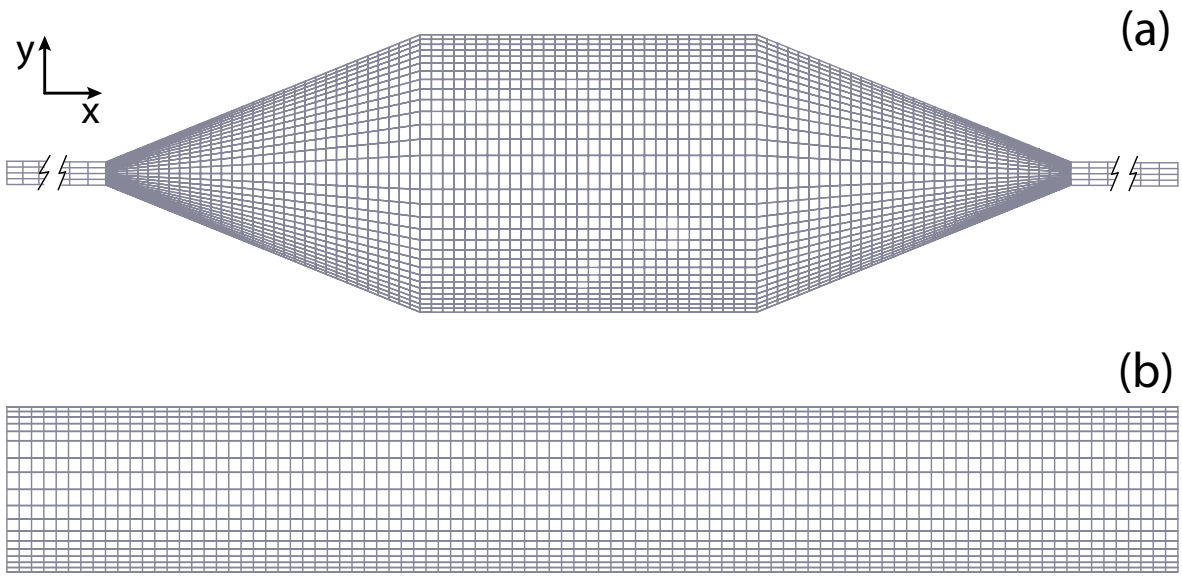

Figure A.1: Mesh representation for the (a)2-D experimental geometry and (b)2-D long fracture, geometry.

We simulated concentrated suspension flow using the modified SBM which included the gravity terms and shear-dependent fluid viscosity. We used the built-in mesh generator, (*blockMesh*), to construct the 2-D representation of the experimental geometry with 19,260 cells (Figure A.1a). The long fracture was modeled using a 2-D fracture with a total of 14,000 cells (Figure A.1b). In all cases, we applied mesh refinement in the y-direction, such that elements in the middle of the mesh were four times larger than the boundary elements. The inlet and outlet tubes were modeled as straight, 1.0 m long square ducts, which allowed the flow to develop before reaching the inlet manifold. The initial conditions consisted of setting velocity and ϕ equal to zero everywhere inside the domain. The boundary conditions included a constant velocity and uniform solid concentration at the inlet with pressure set to zero at the outlet for reference. All walls (e.g., tube, manifold, fracture, and obstructions) were defined as no-slip boundaries.

Appendix B

Uncertainty analysis of solid volume fraction, ϕ

Absorbance is linearly proportional to the medium through which the light passes through. The total amount of light absorbed depends on the material properties, total amount and the distribution of material. Assuming the solids inside our fracture system can be treated as a 'slab' of particles, the light absorbance equation is given by:

$$\begin{aligned} A &= n_s A_{p,s} Q_s b + n_f A_{p,f} Q_f b \\ &= (\frac{3\phi_s}{4\pi a^3}) A_{p,s} Q_s b + (\frac{4\phi_f}{\pi l d^2}) A_{p,f} Q_f b \\ &= \phi_s \alpha_s b + \phi_f \alpha_f b \end{aligned} \tag{B.1}$$

where n is the number of particles per unit volume, ϕ is the volume fraction, A_p is the projected area, Q is the light extinction efficiency, which is a property of the material, b is the aperture, A is the absorbance, and α is the light absorbance per unit length. The subscripts s and f indicate sand and fiber particles, respectively.

The light absorbance per unit length of sand, α_s, was measured independently, in a settling experiment (see text for details). Individual sand particles are assumed to be spherical and therefore their projected area is $A_{p,s} = \pi a^2$. The projected area of fibers depends on the orientation of the fibers, if the normal along the long-axis is oriented parallel to the camera it will have a circular projected area ($A_{p,f} = \pi(d/2)^2$). However, if the fiber's long axis is perpendicular to the camera the projected area will be $A_{p,f} = dl$, where d = fiber diameter and l = fiber length. Fibers tend to align their long-axis parallel to the flow; additionally, fibers are significantly longer than the maximum fracture aperture. Therefore, the projected are will be closer to dl than to $\pi(d/2)^2$ and can be approximated by $A_{p,f} = \mathrm{n}dl$, where n accounts for the angle of the fiber.

We estimate the solid volume fraction of sand, ϕ_s, over all space and time by rearranging Equation B.1, to isolate ϕ_s:

$$\phi_s = \frac{A/b - \phi_f \alpha_f}{\alpha_s} \tag{B.2}$$

therefore, the fractional uncertainty associated with the solid volume fraction is given by:

$$\begin{aligned} \frac{\delta\phi_s}{\phi_s} = \Bigg[& \left(\frac{A/b}{A/b - \phi_f\alpha_f}\right)^2 \left(\left(\frac{\delta A}{A}\right)^2 + \left(\frac{\delta b}{b}\right)^2\right) \\ & + \left(\frac{\phi_f\alpha_f}{A/b - \phi_f\alpha_f}\right)^2 \left(\left(\frac{\delta\phi_f}{\phi_f}\right)^2 + \left(\frac{\delta\alpha_f}{\alpha_f}\right)^2\right) \\ & + \left(\frac{\delta\alpha_s}{\alpha_s}\right)\Bigg]^{1/2} \end{aligned} \tag{B.3}$$

where δ denotes the uncertainty associated with each of the variables. Measured uncertainties of aperture $\delta b/b \approx 0.95\%$ and absorbance $\delta A/A \approx 3.4\%$. We cannot directly measure the uncertainty associated with ϕ_f; due to this, we overestimate the relative uncertainty associated with ϕ_f by setting it to 5%, i.e., $\delta\phi_f/\phi_f \approx 5.0\%$. Using this analysis, we obtain a relative uncertainty for the sand content of approximately 6.2%.

Appendix C

Development of non-Newtonian flow solver: Flow through mixed fracture and porous proppant pack

C.1 Development of numerical flow simulation

Fluid flow through a fracture is typically represented as flow between two parallel plates. For the case of a Newtonian fluid, the fluid velocity through a fracture is given by the cubic law. For non-Newtonian fluids, the average velocity is derived from conservation of mass and momentum, accounting for the non-Newtonian viscosity; in this case the constant viscosity is replaced by an effective viscosity, η_{eff}. We considered flow between parallel plates in a system represented in Fig. C.1. Following mass and momentum conservation equations, and using the Ellis viscosity model (Eq. 5.1) we get the flow between parallel plates for an Ellis fluid:

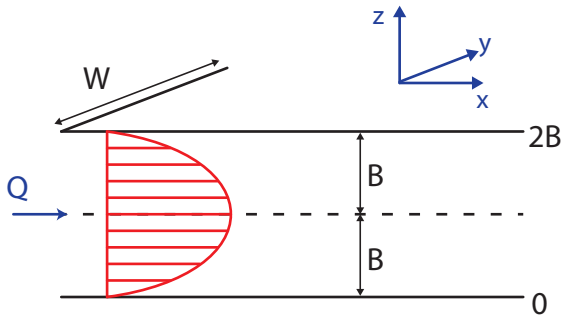

Figure C.1: Schematic for flow between two parallel plates.

$$q_f = \frac{Q}{W(2B)} = \frac{-B^2\gamma_f}{3\eta_0}\frac{\partial h}{\partial x}\left(1 + \frac{3}{(\alpha+2)}\left(\frac{B\gamma_f}{\tau_{1/2}}\right)^{\alpha-1}\left|\frac{\partial h}{\partial x}\right|^{\alpha-1}\right) \tag{C.1}$$

where q_f is the flux per unit area in the fracture, B is the half-aperture, γ_f is the specific weight of the fluid, $\frac{\partial h}{\partial x}$ is the driving head gradient, and η_0, α, and $\tau_{1/2}$ are the Ellis model parameters.

Flow through a porous medium is governed by Darcy's Law. Similarly to the fracture case, when the fluid is non-Newtonian, the constant viscosity is replaced by an effective viscosity. For an Ellis-type fluid the viscosity is a function of the shear-stress, thus we can simply use Eq. 5.1 in Darcy's equation:

$$q_m = \frac{Q}{W(2B)} = \frac{k\gamma_f}{\eta(\tau)}\frac{\partial h}{\partial x} \tag{C.2}$$

where q_m is the flux per unit area through the porous matrix, $\eta(\tau)$ is the fluid viscosity as a function of shear stress, τ, $\frac{\partial h}{\partial x}$ is the head gradient driving flow, and k is the permeability of the porous medium. The permeability depends on the type of material and structure of the porous media, which can be related to the void fraction, $\epsilon = 1-\phi$, using the Kozeny-Carman equation:

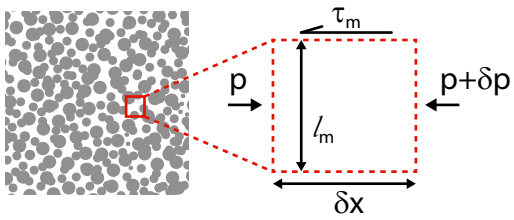

Figure C.2: Schematic used to obtain effective shear stress in fluid element flowing through the porous matrix.

$$k = \frac{d_p^2}{180} \frac{\epsilon^3}{(1-\epsilon)^2} \tag{C.3}$$

where d_p is the average diameter of particles in the porous medium. Substituting the constitutive equation for the Ellis viscosity as a function of shear stress into Eq. C.2 yields:

$$q_m = \frac{Q}{W(2B)} = \frac{k\gamma_f}{\eta_0} \frac{\partial h}{\partial x} \left[1 + \left| \frac{\tau_m}{\tau_{1/2}} \right|^{\alpha-1} \right] \tag{C.4}$$

where τ_m is now defined as the effective shear stress through the porous medium. The effective shear stress can be estimated locally, by considering a fluid element passing through the porous medium (Fig. C.2). Following a procedure similar to that of Tosco et al. (2013), the effective stress through the porous medium is given by:

$$\tau_m = \ell_m \nabla p = \sqrt{\epsilon \cdot k} \nabla p \tag{C.5}$$

where $\ell_m = \sqrt{\epsilon \cdot k}$ is the effective length in the porous medium (Tosco et al., 2013). Substituting this into Eq. C.4 gives the flux per unit area in the porous matrix:

$$q_m = \frac{Q}{W(2B)} = \frac{k\gamma_f}{\eta_0} \frac{\partial h}{\partial x} \left[1 + \left| \frac{\gamma_f \sqrt{\epsilon \cdot k}}{\tau_{1/2}} \right|^{\alpha-1} \left| \frac{\partial h}{\partial x} \right|^{\alpha-1} \right] \tag{C.6}$$

C.1.1 Fracture and porous matrix flow

The flow equations derived above describe flow through fractures (Eq. C.1) and porous medium (Eq. C.6), respectively. When modeling flow through systems which include both fracture and matrix flow, as is the case for many natural systems, must couple these equations to accurately predict flow. Both flux equations (fracture and matrix) have similar functional form, therefore, these equations can be rewritten as:

$$q_f = N_{Lf}\frac{\partial h}{\partial x}\left(1 + N_{NLf}\left|\frac{\partial h}{\partial x}\right|^{\alpha-1}\right) \tag{C.7}$$

$$q_m = N_{Lm}\frac{\partial h}{\partial x}\left(1 + N_{NLm}\left|\frac{\partial h}{\partial x}\right|^{\alpha-1}\right) \tag{C.8}$$

where the first term is the coefficient of the linear contribution to the flow in the fracture (N_{Lf}) and porous media (N_{Lf}), respectively. The terms inside parenthesis (N_{NLf} and N_{NLf}) represent the additional non-linear contribution to the flow, which is a result of the non-Newtonian fluid viscosity, in the fracture and porous matrix, respectively. Thus, Eq. C.7 represents the case where the fluid moves between two adjacent fracture regions. Similarly, Eq. C.8 represents the case where the fluid moves between two adjacent porous matrix regions. Eq. C.7 and C.8 have the same form, the only difference being the linear and non-linear coefficients. The flux between fracture and porous matrix regions can then be approximated by introducing the geometric average of the linear and non-linear coefficients, such that:

$$N_L = \frac{N_{Lf}}{1 + {}^{N_{Lf}}/_{N_{Lm}}} \tag{C.9}$$

$$N_{NL} = \frac{N_{NLf}}{1 + {}^{N_{NLf}}/_{N_{NLm}}} \tag{C.10}$$

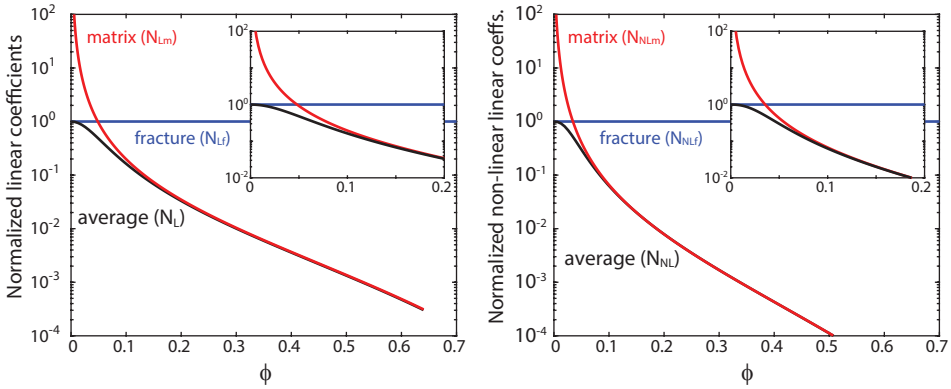

Figure C.3: Fracture (blue), porous matrix (red), and averaged (black) coefficients defined by Eqs. C.9 and C.10. All coefficients are normalized by the value of the fracture coefficient (N_{Lf} and N_{NLf}, respectively). This averaging technique ensures a smooth transition for flow between fracture and porous matrix regions.

This averaging procedure provides a smooth transition between fracture and matrix elements. Figure C.3 shows the linear, non-linear, and averaged coefficients, normalized by the fracture coefficient. At low-ϕ the flow is fracture dominated with both N_L and N_{NL} converging to the value of of N_{fL} and N_{fNL}, respectively. As ϕ increases, the averaged coefficients converged to the porous matrix coefficients, N_{mL} and N_{mNL}, in the Darcy dominated regime. Introducing these averaged coefficients, simplifies Eqs. C.7 and C.8 to a single equation. This eliminated the need to identify whether the flow between two fracture elements, two porous elements, or a combination, since that information is incorporated into the coefficients. Thus the flow equation is through the system is simplified to the single equation:

$$q = N_L \frac{\partial h}{\partial x}\left(1 + N_{NL}\left|\frac{\partial h}{\partial x}\right|^{\alpha-1}\right) \tag{C.11}$$

From the experimental results, we obtain the spatial distribution of aperture and ϕ during and after applying the normal stress. Therefore, we can calculate the spatial distribution of values for both N_L and N_{NL} and can then solve the head field using a Matlab solver.